Doctoral Dissertation

博士論文

Spatial heterogeneity of eddy-mean flow interactions in the Antarctic Circumpolar Current

（南極周極流における渦・平均流相互作用の空間非一様性）

A Dissertation Submitted for the Degree of Doctor of Philosophy

December 2021

令和３年１２月博士（理学）申請

Department of Earth and Planetary Science, Graduate School of Science,
The University of Tokyo

東京大学大学院理学系研究科地球惑星科学専攻

Takuro Matsuta

松田　拓朗

Abstract

The Antarctic Circumpolar Current (ACC) region is believed to play a central role in the global ocean circulation that affects the Earth's climate and material circulations. For better understanding of these circulations in the ACC region, detailed knowledges on the ACC dynamics are imperative. Several observational studies have shown that the isopycnal slope associated with the ACC, hence the magnitude of the ACC, is insensitive to the changes in the winds over the region. This interesting aspect, known as the eddy compensation and eddy saturation, has been suggested to be associated with eddy-mean flow interactions in the ACC region. The eddy compensation and the eddy saturation have been studied mainly by idealized models with zonally uniform assumptions. However, satellite observations show that there is significant inhomogeneity in surface eddy kinetic energy (EKE) in the ACC region, with large EKE in regions called as "the hotspots". However, spatial heterogeneity of the eddy-mean flow interactions that generate the EKE distribution has not been investigated quantitatively in realistic conditions. Although idealized channel models suggest the unrealistic downstream development of the hotspots, this problem has been overlooked in previous studies and mechanisms generating the realistic zonal extent of the hotspots are still in a veil. Therefore, we investigate detailed characteristics of spatial heterogeneity of the eddy-mean flow interactions with the regional Lorenz energy cycle concept. Then, initiation and termination mechanisms of the hotspots are explored from energetic viewpoint. In this study, we utilize results from an eddy-resolving Ocean General Circulation Model (OGCM), named OGCM for the Earth Simulator (OFES), in which many characteristics of the ACC, including a length scale of the hotspots, are well reproduced.

First, the eddy-mean flow interactions are estimated quantitatively based on the Lorenz energy cycle concept. It is confirmed that the classical Lorenz energy cycle includes non-

negligible errors in the ACC region due to the large density fluctuation from the global reference state, which results in the underestimation of the baroclinic energy conversion rate. It turns out that the modified Lorenz energy cycle that takes into account the finite density fluctuation is more appropriate in the ACC region. An analysis based on this modified Lorenz energy cycle shows that five major hotspots are responsible for more than 70% of the EKE generation and dissipation over the ACC region. The energy conversion is dominated by the baroclinic pathway in the four hotspots, while the mixed barotropic and baroclinic instability is important in the region near the Campbell Plateau. We also calculate the work done by the Ekman transport and the horizontal pressure work as a proxy of the available potential energy gain from the westerlies. The advantage of this quantity against the vertical mean density flux is that it is independent from the reference states defined arbitrarily. It is shown that the westerlies can supply sufficient energy locally to initiate the baroclinic instability in the Indian and Pacific sectors of the ACC, whereas the non-local process is important in the Atlantic sector. These results indicate that the mechanisms responsible for the eddy-mean flow interactions are different among five hotspots. We thus need to consider each hotspot one by one to reveal the mechanisms of eddy-mean flow interactions in more detail and their responses to the external forcing, instead of integrating values over the whole ACC as in the previous studies.

In order to investigate the mechanisms for determining the horizonal scale of the hotspots, we conduct the heat budget and EKE budget analyses. The heat budget for the hotspots demonstrates that the heat flux caused by the transient eddies counterbalances to the heat flux due to the standing meanders. The heat flux due to the standing meanders converges in the northern part of the ACC but diverges in the southern part, resulting in the enhancement of the meridional density gradient. This forms a favorable condition for the baroclinic instability. The zonal distribution of the EKE is related to that of the standing heat flux well, suggesting that

the meridional temperature gradient associated with this standing heat flux directly controls the initiation and termination of the hotspots. To reveal the mechanisms responsible for the initiation and termination of the hotspots, each component of the EKE equation for each hotspot is evaluated. The OFES results demonstrate that a large part of the EKE, generated through the baroclinic energy conversion, is balanced by the diabatic dissipation at their generation sites. The remaining part of the EKE is radiated by the advection and pressure fluxes from the upstream side in the hotspots to the downstream side, where it converges. Although the pressure flux convergence plays a secondary role in the horizontal transport of the EKE, it plays a central role in the local EKE sink. It is shown that the vertical pressure flux transports the EKE downward from the depth of eddy energy production above the main thermocline towards the ocean bottom. The EKE converged near the bottom is dissipated due to the diabatic process, indicating that the vertical redistribution of the EKE is the key process for a rather limited zonal extent, i.e. the "downstream decay", of the hotspots. These results show large contrast to the previous studies based on idealized channel models for the ACC, which suggest that the EKE radiation through the horizontal pressure flux sustains the relatively large EKE even in further downstream of the eddy growth region. Therefore, it is concluded that the baroclinicity associated with the major standing meanders in the ACC region directly controls the initiation and termination of the hotspots through the vertical redistribution of the eddy energy. This process also determines the zonal width of the hotspots as well as the magnitude of eddy-mean flow interactions within the hotspots, hence governing most of the eddy-mean flow interactions within the whole ACC region.

Table of Contents

Chapter 1. Introduction

The Antarctic Circumpolar Current (ACC) is a unique strong current in the Southern Ocean flowing eastward under the southern Hemisphere westerlies. The ACC is associated with rather steep tilt of isopycnal surfaces that is manifested by large density gradient in the meridional direction. It has been suggested that the subsurface water draws up to the surface along these tilted isopycnals (e.g. Marshall and Speer 2012). Due to the lack of the continental block at the latitude band of the Drake Passage (56˚S-59˚S), the ACC circulates the globe through the Drake Passage and connects the three major ocean sectors directly. This zonally unblocked structure of the ACC supplies direct pathways for interbasin tracer exchanges (Talley 2013 and references threin). Also, the Southern Ocean is known as a critical component of the global meridional overturning circulation, which connects the ocean interior to the sea surface adiabatically (Marshall and Speer 2012; Talley 2013; Rintoul 2018). It has been shown that as much as 80% of deep waters come back to the surface in the Sothern Ocean and are exposed to the atmosphere, which is responsible for 40 % of the oceanic uptake of anthropogenic CO_2 (Le Quéré et al. 2009). The upwelled deep water is also considered as a major factor in the high melting rate of the base of ice shelf near Antarctica (Rignot et al. 2013). The precise knowledge of the ACC structure and its variations are thus crucial to predict the climate variabilities and climate changes.

It has been considered that eddy-mean flow interactions are essential in momentum balance in the ACC. Since there is no zonal boundary at the latitude band of the Drake Passage, a zonal momentum imparted by the westerlies should be balanced by the topographic form stress (which results from the pressure gradient between the eastern and western side of the topography) (Munk and Palmén 1951), to overcome the issue of unrealistically strong barotropic flow known as “Hidaka’s dilemma” (e.g. Olbers et al. 2012). The similar pressure gradient between the eastern and western side of isopycnal surfaces, called the interfacial form stress, transfers imparted momentum downward (Johnson and Bryden 1989) and results in the

momentum sink around the major topographies by the topographic form stress (Masich et al. 2015). To obtain further insights on the ACC dynamics, the eddy-mean flow interactions have been discussed from the zonally averaged viewpoints, based on the assumption that eddy activities are evenly distributed along the ACC (e.g. Karsten and Marshall 2002; Marshall and Radko 2003; Abernathey et al. 2011). In these zonally averaged models, however, an unrealistic barotropic flow was assumed for the background mean flow, which simply advects the entire flow field and does not interact with the baroclinic component of the flow (Abernathey et al. 2011). A remarkable feature revealed from these idealized model studies is that the isopycnal slopes are insensitive to the changes in the wind forcing. This insensitivity of the isopycnal slope is thus considered to be responsible for an insensitivity of the zonal baroclinic transport of the ACC to the wind forcing, which is referred to as "the eddy saturation" (Munday et al. 2013 and references therein). The baroclinic instability also plays an important role in the meridional overturning circulation. The wind-driven Eulerian overturning circulation with the northward (southward) flow in the surface (subsurface) layer called "Deacon cell" (Döös and Webb 1994) is counterbalanced by the eddy-induced circulations of the opposite direction. This phenomenon is known as "the eddy compensation" (Munday et al. 2013 and references therein).

Although the degree of eddy saturation and eddy compensation taking place in the real ocean is under debate, there are observational evidences from satellite altimetry that surface eddy activities have increased in recent decades (Meredith and Hogg 2006; Thompson and Garabato 2014; Hogg et al. 2015). No increase in the isopycnal tilt is also shown from limited observations (Böning et al. 2008; Firing et al. 2011; Chidichimo et al. 2014). Despite these efforts, detailed mechanisms responsible for "the eddy saturation" and "the eddy compensation" have not been understood because oceanic observations are sparse both in space and in time to resolve eddy-mean flow interactions. Modeling studies using eddy-resolving ocean general

circulation models (OGCM) are thus necessary to better understand roles of eddy activities in the real ocean.

An important missing feature in the zonally-averaged viewpoint in previous studies is the representation of the ACC's inhomogeneity aspects. Although eddy activities has been assumed to be uniformly distributed over the ACC in theoretical studies, Thompson and Garabato (2014) proposed a concept of "intermittent ACC", which refers that the real ACC can be divided into broad regions of weak eddy activities (hereafter called the free zone) and several limited areas of large eddy activities (hereafter called the hotspots) from analyses of outputs from an eddy-resolving OGCM. They also suggested that large transient eddy activities are localized in the vicinity of standing meanders associated with the significant topography and that eddy-mean flow interactions are weak in the regions far from the standing meanders. In fact, their analysis based on the Eliassen-Palm tensor (Plumb 1986) revealed that the eddy forcing along the streamlines of the ACC decelerates the mean flow particularly within the meandering sections in the equilibrium state through localized eddy activities. They proposed an additional mechanism of the eddy saturation, in which these hotspots mainly respond to the wind changes instead of the ACC-wide response.

Eddy-mean flow interactions associated with standing meanders in the ACC are also believed to play a key role in the closure of the global meridional overturning through a subduction and obduction process (Rintoul 2018 and references therein). Sallée et al. (2010) found that the location of the mixed layer trough, which provides a favorable condition for the subduction, is localized near the standing meanders. They also pointed out that the eddy-induced bolus velocity is important for the water mass transport in the vicinity of the ACC. In addition, analyses of the eddy diffusivities have shown that the interaction of transient eddies

with standing meanders enhances cross frontal transport in the lee of topography (Naveira Garabato et al. 2011; Thompson and Sallée 2012).

Despite the above importance of eddy-mean flow interactions in the ACC dynamics, their spatial heterogeneity has not been investigated quantitatively for realistic conditions. For example, although Thompson and Garabato (2014) found localized eddy forcing in the lee of major topographies, a quantitative argument on the role of localized eddy momentum sink in the eddy-mean flow interactions within the whole ACC region was not discussed. In addition, the eddy energy sink in the Southern Ocean has not been clearly determined yet. Contrary to the situation in the mid-latitude regions, where the eddies propagate westward and eddy energy dissipates near the western boundaries (Zhai et al., 2010), such a graveyard for eddies is unknown in the latitude band of the Drake Passage.

Other studies using idealized models also suggested that a standing meander destabilizes the zonal flow, resulting in an initiation of the hotspots of eddy activities (Bischoff and Thompson 2014; Abernathey and Cessi 2014; Chapman et al. 2015; Nadeau and Ferrari 2015; Barthel et al. 2017; Youngs et al. 2019). In particular, Chapman et al. (2015) showed that, while the zonal width of eddy growth region due to baroclinic energy conversion is $O(100)$ km, energy flux by the pressure in the density coordinate, known as the eddy Montgomery flux, maintains the high eddy activities spreads in the zonal direction of $O(1000)$ km further downstream of the growth region. Chapman et al. (2015) thus concluded that the hotspots of eddy activities in the Southern Ocean are characterized as the downstream development similar to the atmospheric storm tracks over the ocean (e.g. Hoskins and Valdes 1990; Chang and Orlanski 1993; Chang 1993; Orlanski and Sheldon 1993; Chang et al. 2002; Danielson et al. 2006; Kaspi and Schneider 2013). The downstream development is also demonstrated to some extent in other idealized models (Bischoff and Thompson 2014). However, as is shown in Fig.

1-1, such downstream development is not observed in the satellite altimeter data, indicating that there is a large gap in our understanding of the spatial scale of the hotspots between the results from idealized models and observations. Detailed investigation on termination mechanisms that suppress the downstream development in the realistic ACC is necessary.

Therefore, the first purpose of this thesis is to investigate characteristics of spatial heterogeneity of the eddy-mean flow interactions in the ACC, with particular focuses on their relations to the localized standing meanders and on quantitative understanding of the roles of hotspots in the eddy-mean flow interactions in the whole ACC. The second purpose is to reveal initiation and termination mechanisms of the hotspots from the energetic viewpoint. We also discuss the ACC response to the changes in wind forcing in the realistic configuration for our better understanding of the eddy saturation process. For these purposes, outputs from an eddy-resolving OGCM is utilized and analyzed in detail. Description and validation of the model appear in Chapter 2. In Chapter 3, we estimate the locality of eddy-mean flow interactions with the regional Lorenz energy cycle concept. A role of the wind-driven Ekman flows for the eddy-mean flow interactions is also investigated. The mechanism to determine the horizonal scale of the hotspots is investigated in Chapter 4 using the heat budget analysis and eddy kinetic energy budget. Chapter 5 provides a discussion and summary of this thesis.

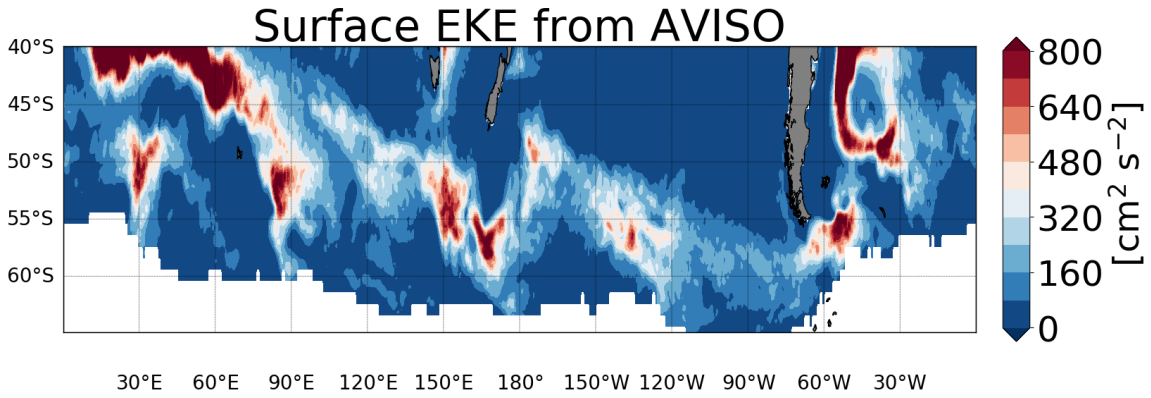

Fig. 1-1. Horizontal distribution of the surface EKE from the satellite altimetry observations for the period of 2001-2010. The derivation of the EKE is shown in Chapter 2.

Chapter 2. Model description and validation

2.1. Model description

In the present study, we utilize results from an eddy-resolving Ocean General Circulation Model (OGCM), named OGCM for the Earth Simulator (OFES) (Masumoto et al. 2004). OFES is a three-dimensional, finite difference primitive equation model based on the Modular Ocean Model ver. 3 (MOM3) developed at GFDL (Pacanowski and Griffies 2000), and optimized for the massively-parallel computational architecture of the Earth Simulator at Japan Agency for Marine-Earth Science and Technology. The model covers quasi-global regions between 75˚S and 75˚N. The horizontal grid spacing is 0.1° x 0.1°, which is reasonably fine to reproduce realistic meso-scale eddies and associated disturbances within the ACC region (Hallberg 2013; Griffies et al. 2015). There are 54 levels in vertical, with varying distance between the levels from 5m at the surface to 330m at the maximum depth of 6,065m. The model topography is constructed from the 1/30° bathymetry dataset created by the OCCAM project at the Southampton Oceanography Centre (obtained through GFDL/NOAA). The partial cell method (Pacanowski and Gnanadesikan 1998) is included to fit the bottom topography into the model as realistic as possible. The major topographies in the ACC region such as the Kerguelen Plateau are well reproduced in OFES. A scale-selective damping of bi-harmonic operator is adopted for horizontal mixing process to suppress computational noises. The vertical mixing processes are parametrized by the K-Profile Parametrization scheme (Large et al. 1994).

Following the spin up by climatological wind stress obtained from the NCEP/NCAR reanalysis (Kalnay et al. 1996) for 50 years, the hindcast run is forced by the daily mean wind stress from 1950 to present. The surface heat flux is calculated by the bulk formula (Rosati and Miyakoda 1988) with the NCEP/NCAR reanalysis outputs for the atmospheric variables and the sea surface temperature (SST) simulated in OFES. The freshwater flux is also obtained from the precipitation rate from the same reanalysis data. Since the sea-ice process as well as the contribution from the river run-off are not included in OFES, the sea surface salinity is

restored to the monthly mean values of the World Ocean Atlas 1998 (Boyer et al. 1998a,b,c) with a relaxation time scale of 6 days. Although the formation of deep waters is not well reproduced due to the lack of sea-ice, eddy activities in the ACC region are largely reproduced realistically (see Chapter 2.2.2 in detail). In this study, outputs at 3-day intervals for a period of 2001-2010 are utilized in Chapters 3 and 4, and 1992-2002 in Chapter 5. See Sasaki et al. (2006, 2008) for more detailed model settings.

2.2 The model validation

2.2.1. The volume transport

The ACC transport through the Drake Passage and the Southern Annular Mode (SAM) index are shown in Fig. 2-1. Each time series is smoothed with a 25 month running mean. The SAM index, which is a proxy for the meridional shift and magnitude of the westerlies, is defined as follows:

$$\mathrm{SAM} = SLP^{*}_{40^{\circ}\mathrm{S}} - SLP^{*}_{65^{\circ}\mathrm{S}}, \tag{2.1}$$

where $SLP^{*}_{40^{\circ}\mathrm{S}}$ and $SLP^{*}_{65^{\circ}\mathrm{S}}$ stand for normalized zonally averaged sea level pressure at 40˚S and 65˚S for every month, respectively (Gong and Wang 1999). The sea level pressure is obtained from the NCEP/NCAR reanalysis. The average and standard deviation of the smoothed ACC transport for the period 1956-2017 is 143 ± 3.0 Sv. Since recent estimates of the observed transports are 154 Sv by Firing et al. (2011) and 173 Sv by Donohue et al. (2016), the transport in OFES is underestimated but reasonably well simulated. The smaller bias in the transport is also seen in other model studies (e.g. Treguier et al. 2010; Bishop et al. 2016). The reason why GCMs tend to underestimate the zonal transport is beyond the scope of this thesis, but it may be related to an underestimation of the bottom friction or viscosity. Several studies (Nadeau and Ferrari 2015; Marshall et al. 2017; Jouanno and Capet 2020) have pointed out that

the circumpolar transport increases with increased bottom friction in idealized models. They suggest that larger friction damps eddies, which eventually results in a weaker energy sink and increased zonal transport. We will revisit this point later in Chapter 5.

In spite of the underestimation of the transport, the small temporal variation in the magnitude of the zonal transport across the Drake Passage suggests that the eddy saturation is well represented in OFES. While the correlation coefficient between the ACC transport and the SAM index shown in Fig. 2-1 is 0.69 with a very small p-value, the regression coefficient to the SAM index is only 2.6 ± 0.25 Sv with the 99% confidence level, indicating the insensitivity of the ACC transport to the westerlies during the analysis period. It is noted that the ACC transport varies interannually associated with the interannual variability in the SAM index, which is consistent with other model studies (e.g. Treguier et al. 2010; Langlais et al. 2015).

2.2.2. Horizontal distributions of the surface Eddy Kinetic Energy

The horizontal distributions of surface eddy kinetic energy (EKE) structure are compared between the OFES outputs and the Archiving, Validation, and Interpretation of Satellite Oceanographic data (AVISO; Ducet et al. 2000) for the model validation. The AVISO data have a spatial resolution of 0.25˚ x 0.25˚ and daily temporal resolution. The transient eddy is defined as the deviations from time-mean:

$$x' = x - \overline{x}, \tag{2.2}$$

where the overbar indicates the time averaging in the period between 2001 and 2010. Eddies defined by the Eq. (2.2) contain variabilities on all time scales simulated in OFES, not just mesoscale eddies. Therefore, some studies apply a temporal lowpass filter to focus on mesoscale eddies (e.g. Chapman et al. 2015; Foppert 2019). However, it is difficult to

distinguish mesoscale eddies from seasonal variabilities because those time scales overlap with each other in the Southern Ocean. It is also known that a temporal filtering generally leads to non-negligible residuals in the energy analysis (Liang 2016). We thus define eddies by the Eq. (2.2) in this study.

The EKE can be calculated as follows:

$$EKE = 0.5\left(\overline{u'^2} + \overline{v'^2}\right). \tag{2.3}$$

The surface zonal (u) and meridional (v) currents are calculated from the geostrophic balance,

$$u = -\frac{g}{f}\frac{\partial \eta}{\partial y}, \tag{2.4}$$

and

$$v = \frac{g}{f}\frac{\partial \eta}{\partial x}, \tag{2.5}$$

where η is the absolute dynamic topography (ADT), g is the acceleration of the gravity, and f is the Coriolis parameter. Horizontal distributions of the EKE from OFES and AVISO are shown in Fig. 2-2. The ACC region in the AVISO data is defined by the southern ACC Front (sACCf) associated with $-98.5\mathrm{cm}$ ADT contour as the southern boundary and Subantarctic Front (SAF) associated with $-3.5\mathrm{cm}$ ADT contour as the northern boundary (Kim and Orsi 2014). The ACC region in OFES is defined as the area bounded by the $-160\mathrm{cm}$ and $-30\mathrm{cm}$ sea surface elevation contours, which represent the sACCf and SAF in the simulated results, respectively (Roquet et al. 2011). The definition of the SAF (sACCf) above is designed as a boundary between the ACC and subtropical (subpolar) region (Orsi et al. 1995). Eddy activities exceeding $400\ \mathrm{cm^2\ s^{-2}}$ are confined in the five relatively narrow regions, which are located downstream of the major standing meanders of the ACC fronts (Thompson and Garabato 2014) and seem to be related to nearby significant bottom reliefs (Katsumata 2017). For example, the

large EKE region at around 80˚E is located downstream of the Kerguelen Plateau. The zonal distribution of the surface EKE emphasizes the sudden transition from strong to weak eddy activities. The meridionally averaged EKE anomalies from the zonal mean within the ACC region are shown in Fig. 2-3. Each profile is 10˚ moving averaged. The overall structures of eddy distribution in OFES show a good agreement with the observation. In the following analyses, we call the region where the 10˚ moving averaged EKE anomaly is positive (negative) as "hotspot" (free zone). Five major hotspots are defined under this definition and are named as Region 1 through Region 5. The zonal extent of these five hotspots are summarized in Table 2-1. We neglect a very narrow hotspots between 335˚E and 342˚E in OFES since the EKE of this hotspot is much weaker than that in other hotspots. The zonal extent and position of Region 1, Region 2, and Region 3 in OFES agree well with the observations, suggesting that the model captures the initiation and termination mechanism of the hotspots in these areas. On the other hand, OFES underestimates the zonal extent of Region 4 and Region 5. While the entrances of these hotspots are well represented in OFES, the zonal extent are smaller than that in the observation. This may result from the bias of the thermal structures south of 60˚S discussed in Section 2.2.3. It is also noted that OFES tends to overestimate the EKE in some areas. In the observations, the EKE anomalies in the Kerguelen Plateau and the Drake Passage are $200\ \mathrm{cm^2\ s^{-2}}$ at most, while anomalies in OFES reach $400\ \mathrm{cm^2\ s^{-2}}$ (Fig. 2-3). Despite these defects shown above, OFES represents the realistic sudden decay of the EKE, suggesting that OFES can be considered as a good proxy for the real world and provides useful dataset to analyze the initiation and termination mechanisms of the hotspots.

2.2.3. The thermal structure

To validate the stratification and thermocline structures in OFES, we compare the potential density and potential temperature distributions with the outputs of Southern Ocean State Estimate (SOSE). SOSE is the eddy-permitting state estimate product of a numerical model (MITgcm) constrained by the least square method to fit available observations including data from Argo floats, satellite observations, and hydrographic profiles. The SOSE products cover the Southern Ocean from 25˚S to 77˚S with the spatial resolution of 1/6˚ x 1/6˚ and 42 levels in vertical. The detailed model setting is shown in Mazloff et al. (2010). At first, we compare the zonal mean structure of the stratification in OFES with that in SOSE, showing that the key climatological features of the hydrography are well represented in OFES. For example, the constant density surfaces rise southward due to the thermal wind balance of the ACC (Fig. 2-4). Especially, the 27.60σ kg m^{-3} density surface, which roughly corresponds to the boundary between the upper and lower cells of the meridional overturning circulation (Marshall and Speer 2012), is getting shallower to the south from about 1500 m depth at 40°S and outcrops to the surface in a region south of 60˚S. The distribution of the potential temperature shows that the thermocline structures in OFES are also similar to that in SOSE. While the thermocline is developed in the upper 1000m depth north of 55˚S, such strong stratifications are absent in the ACC region.

In addition to the zonally averaged structure, the frontal structure in the ACC is also well represented in OFES. We show the meridional section along 80˚E and 95˚E as an example of thermal structures in the hotspots (Fig. 2-5, 6). In the upstream region in the hotspot of Region 2 (80˚E), for example, the thermal structure shows rapid transition across the sharp topography at around 53˚S from warmer condition to the north to colder condition to the south, forming the favorable condition for the baroclinic instability. This steep isopycnal tilting is relaxed in the downstream region in the hotspot (95˚E) both in the OFES and SOSE results (Fig. 2-6).

Therefore, the zonal variations of the thermal structures, particularly the steep isopycnal tilting and its relaxation within the hotspots, are well represented in the OFES results.

Although the good agreements about stratification structures between OFES and the assimilated product are demonstrated, there are also significant discrepancies between the two results. One example is that the deep waters heavier than 27.80σ kg m^{-3} occupies the larger area south of 60˚S at 225˚E (135°W) in Region 4 (Fig. 2-7). The density surface of 27.84σ kg m^{-3} is located at a depth of 1800 m at 65˚S in the OFES result, whereas the same density surface in the SOSE is located around 2800 m depth, which might be a cause of the EKE bias seen in Fig. 2-2. A lack of the sea-ice process in OFES seems to be a possible reason for this bias. Nevertheless, the good agreement in the zonal transport, EKE distribution and mean stratification with SOSE encourages us to look further into the eddy-mean flow interactions in OFES.

Table 2-1. The five hotspots defined from the EKE anomalies for OFES and observation.

[GW]	OFES	Observation
Region 1	23˚E – 41˚E	22˚E - 38˚E
Region 2	78˚E – 101˚E	77˚E - 101˚E
Region 3	146˚E – 180˚E	145˚E - 177˚E
Region 4	211˚E – 232˚E	209˚E - 242˚E
Region 5	293˚E – 321˚E	292˚E – 336˚E

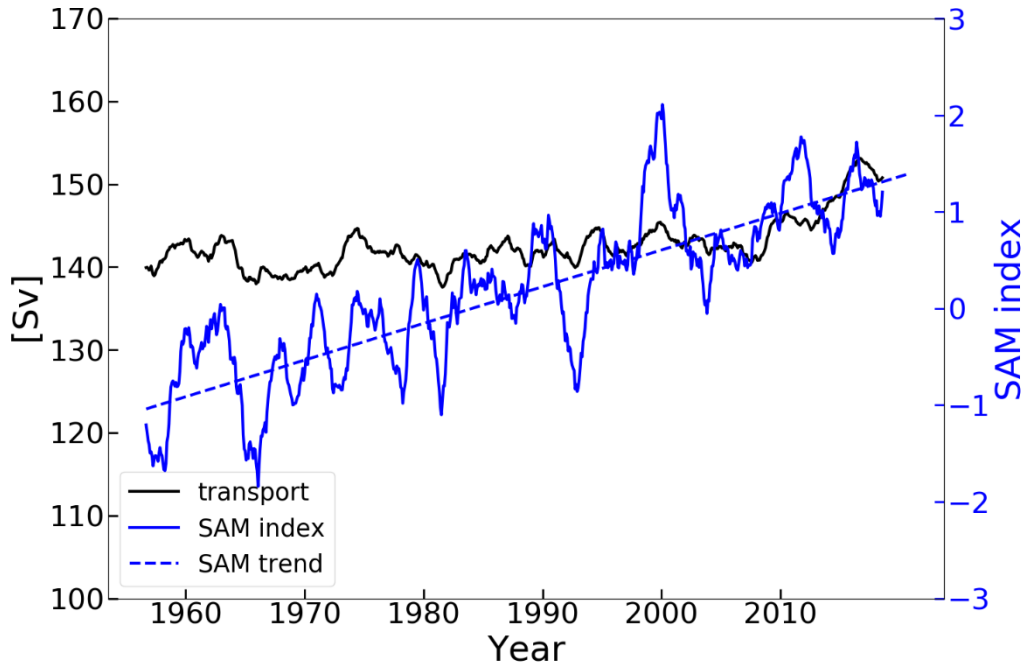

Fig. 2-1. Time series of the ACC transport through the Drake Passage (black solid line) and the SAM index variability (blue solid line) with its trend shown by the dashed blue line. Each time series is smoothed with a 25 month running mean.

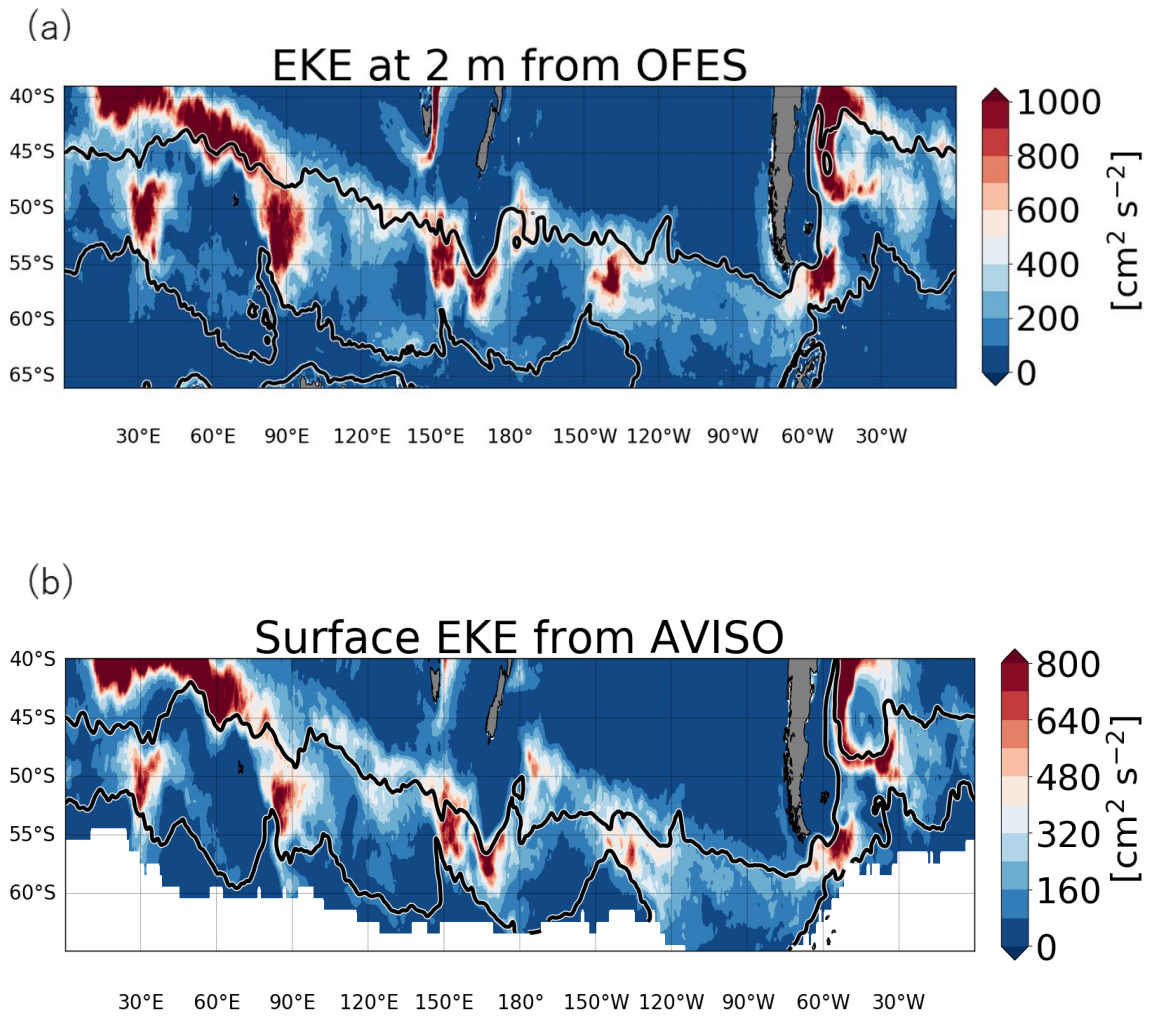

Fig. 2-2. Horizontal distribution of the surface EKE from (a) OFES and (b) satellite altimetry observations. The northern and southern black contours represent the Subantarctic Front and the southern ACC Front, respectively. The definitions for each front are shown in the main text.

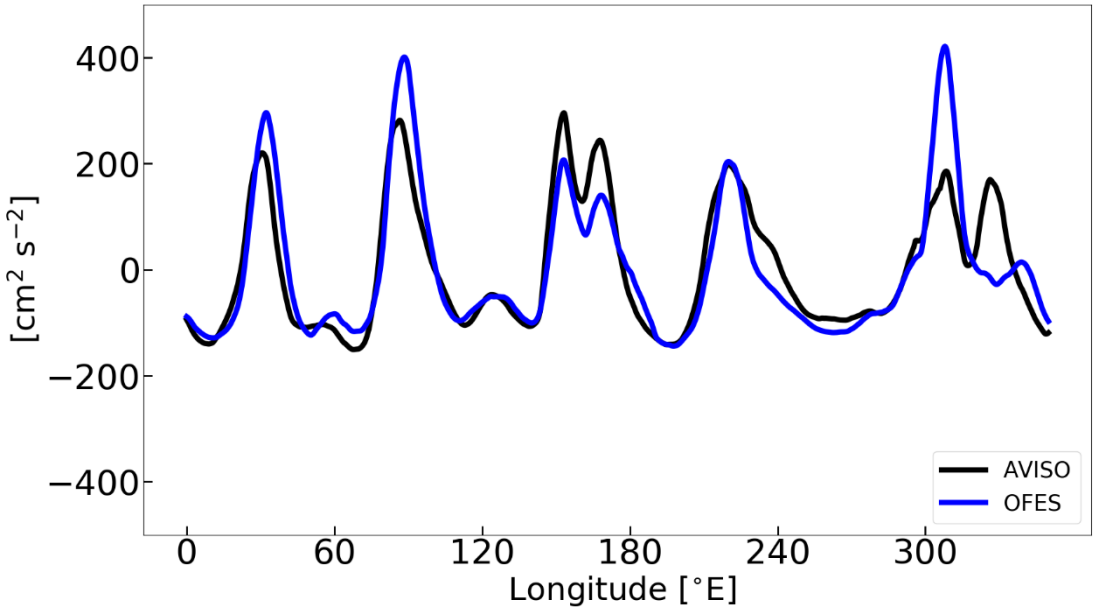

Fig. 2-3. Surface EKE anomalies from those zonal mean obtained from AVISO (black line) and OFES (blue line). These anomalies are plotted as a function of longitude and averaged over the meridional extent of the ACC region and smoothed with a 10˚ running mean.

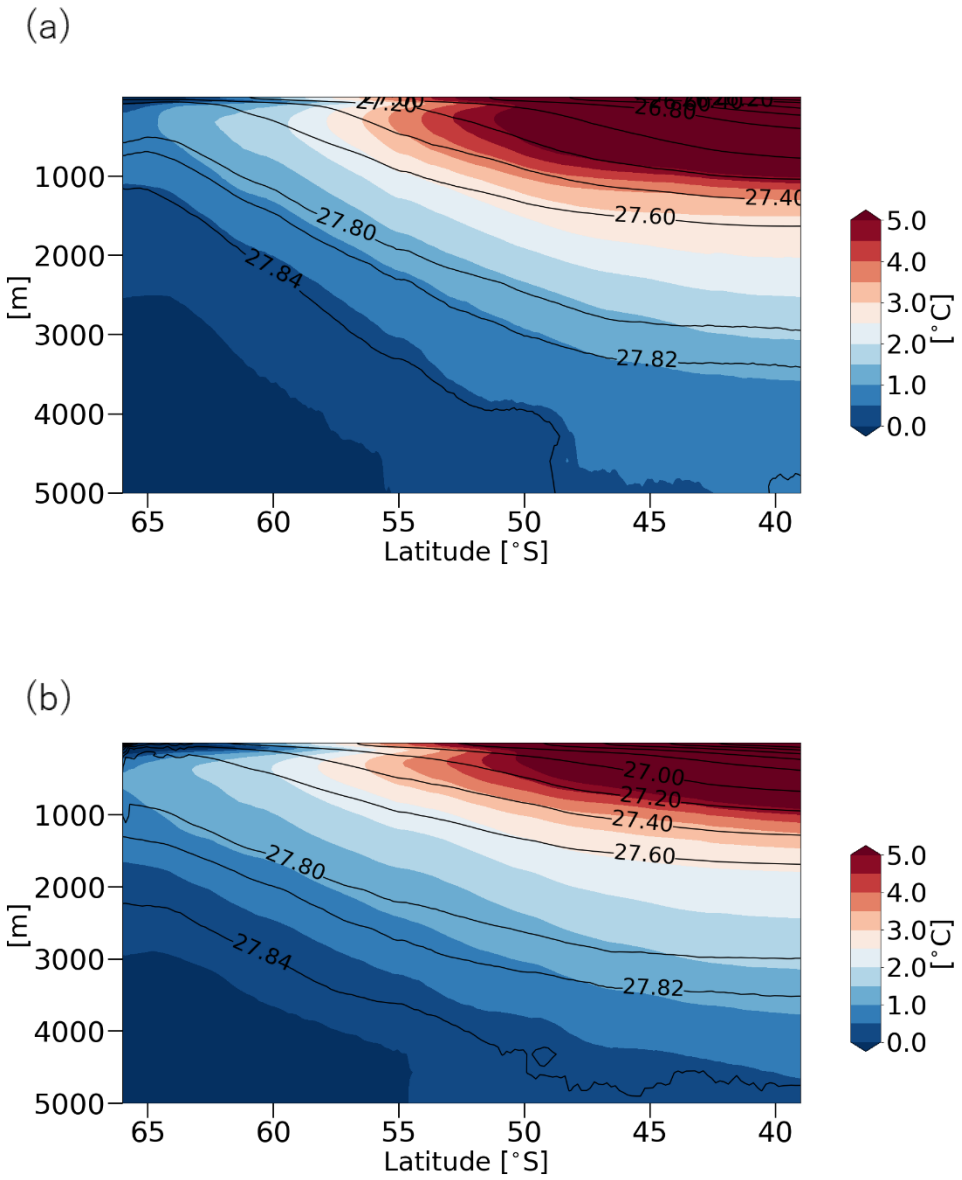

Fig. 2-4. Meridional sections of the zonally averaged potential temperature in (a) OFES and (b) SOSE. Black contours in (a) and (b) represent the zonally averaged potential density.

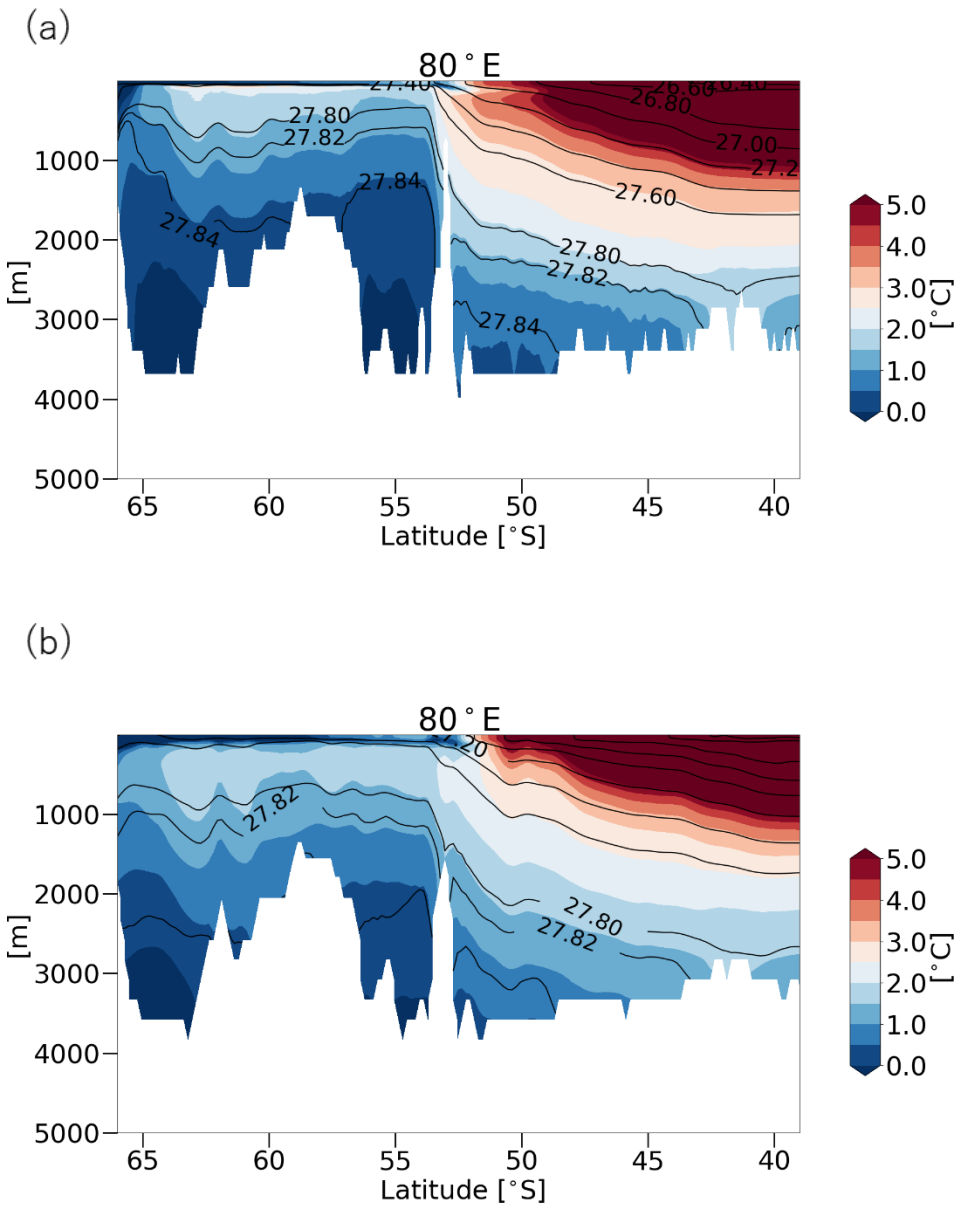

Fig. 2-5. Meridional sections of the potential temperature along 80˚E from (a) OFES and (b) SOSE. Black contours represent the potential density at the same section.

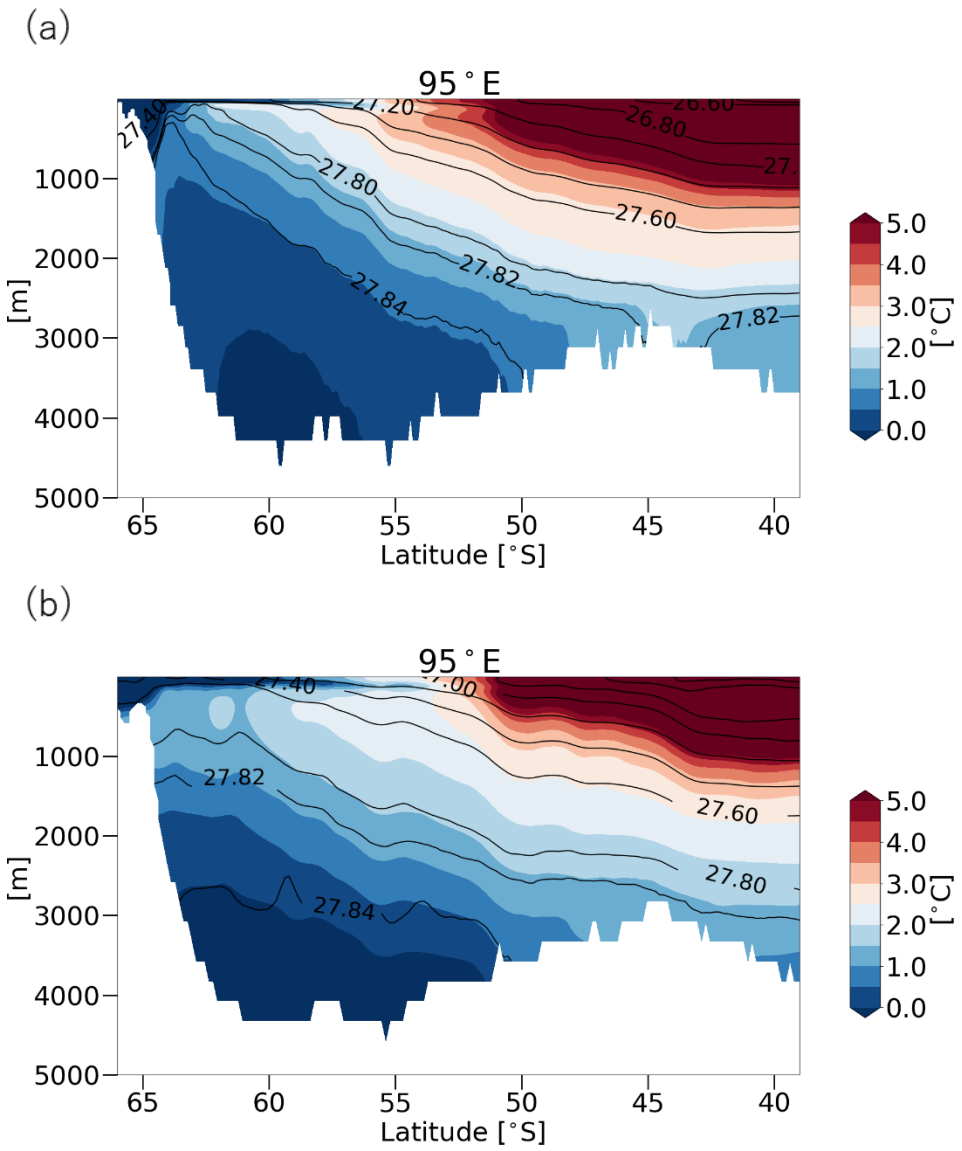

Fig. 2-6. Same as Fig. 2-5 but along 95˚E.

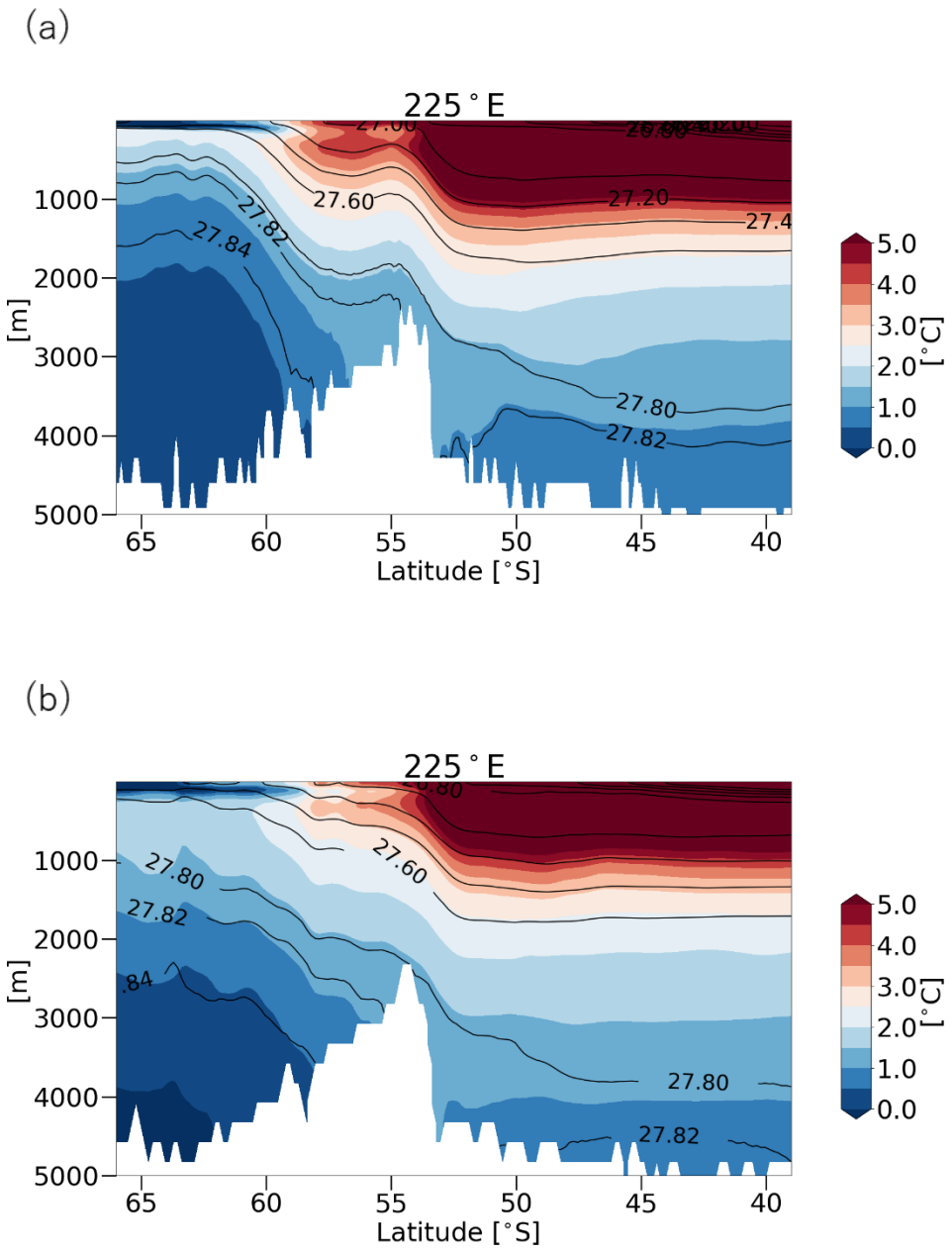

Fig. 2-7. Same as Fig. 2-5 but along 225˚E.

Chapter 3. Quantitative estimation of eddy-mean flow interactions in the ACC

In this chapter, we adopt the Lorenz Energy Cycle (LEC) to answer the following question; how much the five hotspots can explain the eddy-mean flow interactions and eddy energy sink over the ACC region. We first revisit the LEC concept in order to define the baroclinic conversion rate that is appropriate for higher latitude regions. Then, using the outputs of OFES, the energy conversions between the mean flow and eddies are estimated.

3.1. Energetics framework

The LEC developed by Lorenz (1955) is a powerful diagnostic tool for studying eddy-mean flow interactions and has been utilized to estimate energy budgets of the Southern Ocean in previous researches (Chen et al. 2014, 2016; Wu et al. 2017; Youngs et al. 2017; Jüling et al. 2018). The LEC can quantify eddy-mean flow interactions as the energy conversion rates among energy reservoirs. While the energy conversions associated with the kinetic energy in the LEC are valid in general, the energy exchange between the mean and eddy available potential energy (APE) depends on the assumption that the density fluctuations from the reference state is small enough, which is sometimes denoted as "the LEC limit" (Scotti and White 2014; Zemskova et al. 2015). Since the isopycnal slope is steep in the Southern Ocean, the stratification of the ACC is rather different from the global reference state. An application of the LEC is thus likely to include non-negligible errors as suggested by Scotti and White (2014). We revisit the classical LEC and the modified LEC by Zemskova et al. (2015), and estimate the errors of the LEC in the ACC region in this section.

3.1.1 Governing equations for OFES

OFES is governed by the primitive equations under the Boussinesq assumption:

$$\frac{D\boldsymbol{u_h}}{Dt} + f\boldsymbol{k} \times \boldsymbol{u_h} = -\frac{1}{\rho_0}\nabla_h p + \boldsymbol{D_h}, \tag{3.1}$$

$$\frac{\partial p}{\partial z} = -\rho g, \qquad \nabla \cdot \boldsymbol{u} = 0, \tag{3.2}$$

and

$$\frac{DT}{Dt} = H_T, \qquad \frac{DS}{Dt} = H_S, \tag{3.3}$$

where $\boldsymbol{u} = (u, v, w)$ is the three-dimensional velocity, $\boldsymbol{u}_h$ is its horizontal component, and $\boldsymbol{k}$ is the vertical unit vector; T and S are the potential temperature and salinity, respectively; $\rho_0 = 1035$ kg m^{-3} is the constant reference density; $\boldsymbol{D}_h$ represents a viscosity, ∇_h is the horizontal component of the three-dimensional gradient operator ∇, and $\frac{D}{Dt} = \frac{\partial}{\partial t} + \boldsymbol{u} \cdot \nabla$ is the material derivative. The variable H_T (H_S) is the change rate of potential temperature (salinity) due to the vertical mixing process parameterized by the KPP scheme and air-seas exchange of heat (salinity). The density is determined by the nonlinear equation of state $\rho = \rho(T, S, \rho_0 g z)$. Combining two equations in (3.3), the potential density referred to a depth of 2000 m (we simply call this quantity the "potential density" and denoted as σ unless otherwise stated hereafter) and the in-situ density (denoted as ρ) follow

$$\frac{D\sigma}{Dt} = \alpha(T, S, 2000) H_T + \beta(T, S, 2000) H_S, \tag{3.4}$$

$$\frac{D\rho}{Dt} = \alpha(T, S, z) H_T + \beta(T, S, z) H_S + \gamma(T, S, z) w, \tag{3.5}$$

with $\alpha(T, S, z) = \left(\frac{\partial \rho}{\partial T}\right)_{S,z}$, $\beta(T, S, z) = \left(\frac{\partial \rho}{\partial S}\right)_{T,z}$, and $\gamma(T, S, z) = \left(\frac{\partial \rho}{\partial z}\right)_{T,S}$ (see APPENDIX of Chen et al. (2014) for a derivation of the Eqs. (3.4) and (3.5)).

3.1.2 The classical Lorenz Energy cycle (LEC)

With the separation of Eq. (2.2) between the mean field and eddy turbulences, the mean kinetic and APE are respectively defined as

$$K_M(\boldsymbol{x}) = \frac{1}{2}\rho_0\left(\overline{u}^2 + \overline{v}^2\right), \tag{3.6}$$

$$P_M^{(LEC)}(\boldsymbol{x}) = -\frac{1}{2}\frac{g}{\partial_z \sigma_{bg}^{(LEC)}(z)}\,\overline{\rho^*}^2, \tag{3.7}$$

and the eddy kinetic energy (EKE) and the eddy available potential energy are defined as

$$K_E(\boldsymbol{x}) = \frac{1}{2}\rho_0\left(\overline{u'^2} + \overline{v'^2}\right), \tag{3.8}$$

$$P_E^{(LEC)}(\boldsymbol{x}) = -\frac{1}{2}\frac{g}{\partial_z \sigma_{bg}^{(LEC)}(z)}\,\overline{\rho'^2}\,. \tag{3.9}$$

Here, $\sigma_{bg}^{(LEC)}(z)$ is the horizontal average of the time-mean potential density (Von Storch et al. 2012). The fluctuation of the density from the reference state is defined by

$$\rho^*(t,x,y,z) = \rho(t,x,y,z) - \rho_{bg}^{(LEC)}(z), \tag{3.10}$$

where $\rho_{bg}^{(LEC)}(z)$ is the horizontal average of the time-mean in-situ density. It is noted that the mean and eddy APE above are the same as those for the quasi-geostrophic flow (e.g. Olbers et al. 2012), while the quasi-geostrophy is not a necessary condition.

According to Chen et al. (2014), the mean flow and eddy energy equations satisfy

$$\begin{aligned}&\frac{\partial}{\partial t}K_M + \nabla\cdot(\overline{\boldsymbol{u}}K_M) + \rho_0\nabla\cdot\left(\overline{u}\,\overline{u'\boldsymbol{u'}} + \overline{v}\,\overline{v'\boldsymbol{u'}}\right) + \nabla\cdot\left(\overline{\boldsymbol{u}}\,\overline{p^*}\right)\\ &\quad = -g\overline{\rho^*}\,\overline{w} - \rho_0\left[-\overline{u'\boldsymbol{u'}}\cdot\nabla\overline{u} - \overline{v'\boldsymbol{u'}}\cdot\nabla\overline{v}\right] + X(K_M),\end{aligned} \tag{3.11}$$

$$\begin{aligned}&\frac{\partial}{\partial t}K_E + \nabla\cdot\left(\overline{\boldsymbol{u}}K_E + \overline{\boldsymbol{u'}\frac{1}{2}\rho_0\left(u'^2 + v'^2\right)}\right) + \nabla\cdot\left(\overline{\boldsymbol{u'}p'}\right)\\ &\quad = -g\overline{\rho' w'} + \rho_0\left[-\overline{u'\boldsymbol{u'}}\cdot\nabla\overline{u} - \overline{v'\boldsymbol{u'}}\cdot\nabla\overline{v}\right] + X(K_E)\end{aligned} \tag{3.12}$$

$$\frac{\partial}{\partial t}P_M^{(LEC)} + \nabla\cdot\left(\overline{\boldsymbol{u}}P_M^{(LEC)}\right) + \nabla_h\cdot\left(-\overline{\rho'\boldsymbol{u}_h'}\,\frac{g}{\partial_z\sigma_{bg}^{(LEC)}}\overline{\rho^*}\right)$$
$$= g\overline{\rho^*}\overline{w} - \frac{g}{\partial_z\sigma_{bg}^{(LEC)}}\overline{\rho'\boldsymbol{u}_h'}\cdot\nabla_h\overline{\rho^*} + X(P_M^{(LEC)}), \tag{3.13}$$

$$\frac{\partial}{\partial t}P_E^{(LEC)} + \nabla\cdot\left(\overline{\boldsymbol{u}}P_E^{(LEC)}\right) + \nabla\cdot\left(-\frac{g}{2\partial_z\sigma_{bg}^{(LEC)}}\overline{\boldsymbol{u}'\rho'^2}\right)$$
$$= g\overline{\rho'w'} + \frac{g}{\partial_z\sigma_{bg}^{(LEC)}}\overline{\rho'\boldsymbol{u}_h'}\cdot\nabla_h\overline{\rho^*} + X(P_E^{(LEC)}), \tag{3.14}$$

where p^* is the combined sea surface elevation and hydrostatic pressure fluctuations referenced to the background pressure field, $p^* = p - p_{ref}(z)$, $X(\cdot)$ is the source/sink term calculated as the residual from the respective balance equation. The energy cycle associated with the Eqs. (3.11) - (3.14) i.e. the LEC is illustrated in Fig. 3-1(a).

The second term of the right-hand side in the Eqs. (3.11) and (3.12), i.e.

$$BTR = \rho_0\left[-\overline{u'\boldsymbol{u}'}\cdot\nabla\overline{u} - \overline{v'\boldsymbol{u}'}\cdot\nabla\overline{v}\right], \tag{3.15}$$

is the barotropic conversion rate (BTR) due to eddy-mean flow interactions. A positive value of the BTR means that the barotropic instability transfers the mean flow energy into the EKE. Similarly, the second term of the right-hand side of the Eqs. (3.13) and (3.14), i.e.

$$BCR^{(LEC)} = \frac{g}{\partial_z\sigma_{bg}^{(LEC)}}\overline{\rho'\boldsymbol{u}_h'}\cdot\nabla_h\overline{\rho^*}, \tag{3.16}$$

is the baroclinic conversion rate (BCR) of the LEC, whose positive sign indicates that eddies extract the mean APE from the mean stratification. The first term on the right-hand side of the Eqs. (3.12) and (3.14), i.e.

$$VEDF = -g\overline{\rho'w'} \tag{3.17}$$

is the vertical eddy density flux (VEDF), which drains the EKE from the stratifications. Positive values of the VEDF are associated with the convective process, with dense fluid sinking and light fluid rising in baroclinic instability (Zhai and Marshall 2013; Aiki et al. 2016). The third term of the left-hand side of (3.12), i.e. $\nabla\left(\overline{\boldsymbol{u}'p'}\right)$, is the divergence of the three-dimensional energy flux by the eddy pressure flux, of which the vertical component $\partial_z\left(\overline{w'p'}\right)$ represents redistribution of the EKE in vertical (Zhai and Marshall 2013). We will show this vertical pressure flux plays a significant role in an energy redistribution process in Chapter 4.

3.1.3 The modified LEC and comparison with the original LEC

If the density fluctuation of the Eq. (3.10) is not small, the quadratic form of the APE Eqs. (3.7) and (3.9) are not valid (Scotti and White 2014 and references therein). This is because the contribution from the higher order of the Taylor's expansion of the Eq. (3.10), which is dropped under the LEC limit, become non-negligible. While the kinetic energy equations of the Eqs. (3.11) and (3.12) are valid in general, the APE equations of the Eqs. (3.13) and (3.14) should be modified. We thus define the local APE without the small fluctuation assumption following Scotti and White (2014) and Zemskova et al. (2015):

$$P(\boldsymbol{x},t) = g\int_{\sigma_{bg}(z,t)}^{\sigma(\boldsymbol{x},t)}\Big(z - z_{bg}(s,t)\Big)\,ds\,, \tag{3.18}$$

where t is time, z_{bg} is the reference height and σ_{bg} is the reference potential density defined by the relationship $z_{bg}\big(\sigma_{bg}(z,t),t\big) = z$. The integral above is calculated in the potential density coordinate (a variable s represents the potential density as the integral variable). Here, the reference height z_{bg} is for a given value of the potential density σ, the volume contained below $z_{bg}(\sigma,t)$ equals the volume of all parcel of fluid heavier than or equal to σ. This

reference states can be calculated efficiently with the aid of the probability density function method developed by Tseng and Ferziger (2001). In the LEC limit, the Taylor's expansion of the Eq. (3.18) converges to the quadratic form:

$$P(\boldsymbol{x},t) \approx -\frac{1}{2}\frac{g}{\partial_z \sigma_{bg}}\left(\sigma-\sigma_{bg}\right)^2, \tag{3.19}$$

which reproduces the mean and eddy APE (the Eqs. (3.7) and (3.9)) in the LEC limit. It is noted that since the in-situ density is not conservative, APE definition in this study is based on the potential density referenced to 2000m depth as is done in previous studies (Aiki and Richards 2008; Scotti and White 2014; Zemskova et al. 2015; Aiki et al. 2016; Zhu et al. 2018).

The time-average of the APE can be decomposed into mean and eddy parts (Scotti and White 2014):

$$P_M(\boldsymbol{x}) = g\int_{\overline{\sigma_{bg}}(z)}^{\overline{\sigma}(\boldsymbol{x})}\left(z-\hat{z}_{bg}(s)\right)ds\,, \tag{3.20}$$

and

$$P_E(\boldsymbol{x}) = \overline{P}-P_M = \overline{g\int_{\overline{\sigma_{bg(z)}}}^{\sigma(\boldsymbol{x})}\left(z-\hat{z}_{bg}(s)\right)ds}\ . \tag{3.21}$$

Here, $\hat{z}_{bg}$ is the mean reference height defined by the relation $\hat{z}_{bg}\left(\overline{\sigma_{bg}}(z)\right)=z$. The mean and eddy APE shown above are governed by the following equations;

$$\begin{aligned}&\frac{\partial}{\partial t}P_M+\nabla\cdot(\overline{\boldsymbol{u}}P_M)+\nabla\cdot\left(g\left(z-\hat{z}_{bg}\right)\overline{\boldsymbol{u}'\sigma'}\right)\\ &=g\overline{w}\left(\overline{\sigma}-\overline{\sigma_{bg}}\right)-\left[\frac{g}{\partial_z\overline{\sigma_{bg}}}\overline{\boldsymbol{u}'\sigma_h'}\cdot\nabla_h\overline{\sigma}+g\overline{w'\sigma'}\left(\frac{\partial_z\overline{\sigma}}{\partial_z\overline{\sigma_{bg}}}-1\right)\right]+X(P_M),\end{aligned} \tag{3.22}$$

$$\frac{\partial}{\partial t}P_E + \nabla\cdot(\overline{\boldsymbol{u}}P_E) + \nabla\cdot\left(\overline{\boldsymbol{u}'\int_{\overline{\sigma(\boldsymbol{x})}}^{\sigma(\boldsymbol{x},t)}\left(z_{bg}(\overline{\sigma(\boldsymbol{x})},t) - z_{bg}(s,t)\right)ds}\right)$$
$$= g\overline{\sigma' w'} + \left[\frac{g}{\partial_z\overline{\sigma}_{bg}}\overline{\boldsymbol{u}'\sigma_h'}\cdot\nabla_h\overline{\sigma} + g\overline{w'\sigma'}\left(\frac{\partial_z\overline{\sigma}}{\partial_z\overline{\sigma}_{bg}} - 1\right)\right] + X(P_E), \tag{3.23}$$

which leads to the modified LEC by Zemskova et al. (2015) (Fig. 3-1b). The first term of the right-hand side of Eq. (3.23) is equivalent to the VEDF in the original LEC, and therefore we also call $-g\overline{\sigma' w'}$ the VEDF hereafter. The BCR of the modified LEC is defined as

$$BCR = \left[\frac{g}{\partial_z\overline{\sigma}_{bg}}\overline{\boldsymbol{u}'\sigma_h'}\cdot\nabla_h\overline{\sigma} + g\overline{w'\sigma'}\left(\frac{\partial_z\overline{\sigma}}{\partial_z\overline{\sigma}_{bg}} - 1\right)\right]$$
$$= BCR^{(LEC)} + BCR_v, \tag{3.24}$$

where $BCR_v = g\overline{w'\sigma'}\left(\frac{\partial_z\overline{\sigma}}{\partial_z\overline{\sigma}_{bg}} - 1\right)$ is the vertical component of the BCR which reduces to zero in the LEC limit. Although this modified BCR is derived by the Zemskova et al. (2015), its spatial distribution in the Southern Ocean is discussed for the first time in this study. Other energy transfers among energy reservoirs have the same forms with the classical LEC.

To assess the validity of the LEC limit, we calculate the probability distribution function for the fluctuations of the mean potential density field from the global reference field. Figure 3-2a shows that the probability distribution of the density fluctuation exceeding 0.1 kg m^{-3} reaches about 80%. Although large fluctuations larger than 1.0 kg m^{-3} are confined within the surface mixed layer, the deviations in the interior ocean are also non-negligible. To confirm this, we calculate the probability distribution confined in the layer between 300 m and 2000 m depths, where eddy-mean flow interactions are active in the ACC region (Abernathey and Cessi 2014). According to Fig. 3-2b, the high probability density appears in the density range between 0.1 kg m^{-3} and 1.0 kg m^{-3} in this case, suggesting that the LEC limit is not satisfied in the interior of the Southern Ocean either. It is noted that the density fluctuations are also non-negligible even if the background state is calculated from the potential density field

confined in the Southern Ocean as is done in several previous studies (Wu et al. 2017; Jüling et al. 2018).

The large fluctuations in the potential density lead to a substantial error of the BCR. We estimate the baroclinic energy pathway, i.e. $P_M \rightarrow P_E \rightarrow K_E$, for the LEC and the modified LEC over the ACC region, respectively. The ACC region is defined as the area bounded by the -160cm and -30cm sea surface contours in the meridional direction (see Section 2.2.2). The results shown in Fig. 3-3 indicate that the BCR of the LEC is 30% smaller than that of the modified LEC. This mismatch is caused by the second term of the Eq. (3.24), which is included in the residual term in the LEC (Fig. 3-3a). Therefore, the residual term of the classical LEC includes the substantial part of the baroclinic energy conversion in addition to the eddy APE diffusion and transport. In this stage, it is found that the classical LEC underestimates the BCR, and therefore we utilize the modified Lorenz diagram in this chapter. It is this modified diagram that makes it possible to evaluate the detailed energy conversions quantitatively in the ACC region.

3.2 Results

3.2.1 Basic structures of the EKE in the ACC

We first examine the basic structures of eddy activities in the ACC region. Horizontal distribution of the vertically averaged EKE is shown in Fig. 3-4(a). Figures for horizontal distributions in this thesis are drawn with a spatial average over 0.5˚ x 0.5˚ boxes to reduce small-scale noise. The hotspots defined in Section 2.2.2 are indicated by green latitude lines. Although the hotspots are defined by the surface EKE, the large values of vertically averaged EKE are confined well within the hotspots, suggesting that the eddies have vertically coherent structures in some extent. The maximum values of EKE exceed $200\ \text{cm}^2\ \text{s}^{-2}$ in the regions

inside of the five hotspots, while the EKE is weaker than $80\ \mathrm{cm^2\ s^{-2}}$ in the free zone, indicating non-uniformity in the zonal direction of the eddy activities in the ACC.

Figure. 3-4(b) shows spatial distributions of the mean wind energy input at the sea surface. The mean wind energy input is calculated using $W_{wind} = \overline{\boldsymbol{\tau}} \cdot \overline{\boldsymbol{u_0}}$, where $\overline{\boldsymbol{\tau}}$ is the mean surface wind stress and $\overline{\boldsymbol{u_0}}$ is the mean total surface velocity (Zhai and Marshall 2013). Since the surface wind stress associated with westerlies over the Southern Ocean reaches as high as $0.1\ \mathrm{N\ m^{-2}}$ and is more or less uniformly distributed along the ACC path, the energy input is also large in a wide area within the ACC, where the input exceeds $2.0 \times 10^{-2}\ \mathrm{W\ m^{-2}}$, except for the Drake Passage. The atmospheric winds thus tend to homogeneously input the energy into the ocean, indicating that local features in the EKE do not originate from the distribution of the external forcing.

To depict the relation between the standing meanders and the hotspots, we show the horizontal distribution of the bathymetry with the sea surface elevation (Fig. 3-5a). Although we focus on Region 3 as an example, the results below are applicable to other hotspots. Figure 3-5(a) indicates that the ACC in Region 3 is guided by the standing meanders associated with the Southeast Indian Ridge from (140˚E, 50˚S) towards (180˚E, 65˚S), which is highlighted by the bathymetry shallower than 3200m depth. The mean meridional velocity averaged from the ocean surface to the ocean bottom along the 58˚S latitude line (Fig. 3-5b) suggests that the wavelength of the standing meanders is about 500km, which is also confirmed by the fast Fourier transform (not shown). If we consider the standing meanders as the stationary Rossby waves as suggested in Hughes (2005), the zonal length scale of the above-mentioned standing meanders matches the dispersion relationship:

$$k^2 + l^2 = \frac{\beta}{\overline{u}}, \tag{3.25}$$

where k (l) is the zonal (meridional) wave number, $\overline{u}$ is the mean zonal velocity, and β is the beta constant. The derivation of the dispersion relation for the stationary Rossby wave is documented in Hughes (2005). According to the Eq. (3.25) with $l = 0$, the mean zonal velocity $\overline{u} = 10\text{cm s}^{-1}$ and beta constant $\beta = 1.0 \times 10^{-11}\ \text{m}^{-1}\ \text{s}^{-1}$, the length scale of the stationary Rossby wave L_x is approximated to $L_x \sim \left(2\pi \frac{\overline{u}}{\beta}\right)^{\frac{1}{2}} = 628$ km, which is comparable to the zonal wavelength of standing meanders (Fig. 3-5b). Since the typical length scale of eddies in the ACC is the first baroclinic Rossby radius of deformation (about 25km at 44˚S) (Williams et al. 2007), there is a moderate scale separation between standing meanders and eddies as suggested in an observational study (Williams et al. 2007) and idealized models (Bischoff and Thompson 2014; Chapman et al. 2015).

The vertical profiles of the EKE averaged meridionally within the ACC remarkably emphasize the heterogeneity of eddy activities (Fig. 3-6). The EKE shows vertically coherent structures inside the hotspot regions, with the maximum values larger than $80\ \text{cm}^2\ \text{s}^{-2}$ even in the layer deeper than 2000 m depth. On the other hand, deep reaching eddy activities are absent outside the hotspots. Although the surface EKE is relatively large in the region of 105˚E-130˚E and 330˚E-350˚E outside of the hotspots, the eddy activities are confined in the upper 1000 m depth in these regions. Therefore, the downward spread of EKE is a significant characteristic of the hotspots. The reason for this vertically coherent structure is discussed in Chapter 4 in detail.

3.2.2 The energy diagram analysis

The modified energy diagram shown in Fig. 3-7 summarizes exchanges among energy reservoirs in the entire ACC region. The ACC region as a whole receives 705 GW of the mean

kinetic energy from the wind forcing. While a large part of this gain is mainly dissipated within the Ekman layer (discussed in Chapter 3.3), 41% of the wind energy input is converted to the mean APE through the $VMDF = g\left(\overline{\sigma} - \overline{\sigma_{bg}}\right)\overline{w}$. The westerlies drive surface light waters northward and bring up the relatively dense waters below the surface, which stores the APE through the isopycnal tilting. From the energetic viewpoint, this energy conversion from the mean kinetic energy to the APE sustains the Deacon cell, which is a wind-driven meridional overturning circulation with the northward surface flow and the southward subsurface flow (e.g. Döös and Webb 1994; Marshall and Radko 2003; Marshall and Speer 2012). The mean APE stored in the tilted isopycnals is released through the baroclinic instability and generates eddy APE, indicated by the BCR in the energy diagram, of which 87% is converted to the EKE through the convective process represented by the VEDF. The magnitude of the VEDF reaches 220 GW and most of the EKE generated by the baroclinic instability is dissipated within the EKE reservoir. On the other hand, the value of 6 GW of the BTR is an order of magnitude smaller than that of the VEDF, indicating that the baroclinic energy pathway is dominant for the wind energy sink in the ACC. This result is consistent with the observational study by Phillips and Rintoul (2000), which suggests that the eddy-mean flow interactions in the Southern Ocean is dominated by the baroclinic energy conversion and the Reynolds stress plays only secondary roles.

While previous studies (Chen et al. 2014; Wu et al. 2017) already investigated the energy balance over the entire Southern Ocean, contributions from the previously mentioned five hotspots have not been discussed quantitatively yet. The values integrated over each hotspot for the wind energy input, BTR, BCR, VEDF, and EKE sink are summarized in Table 3-1. The sum of VEDF (the EKE sink i.e. $X(K_E)$) over the five hotspots reaches 161 GW (158 GW), which corresponds to 73 % (72 %) of the value integrated over the entire ACC. The BCR over the five hotspots also explains 72 % of that over the entire ACC region. On the other hand, the

wind energy input over the five hotspots, 240 GW, is 34 % of that integrated over the entire ACC, 705 GW. This percentage corresponds to the ratio of the area of five hotspots to the area of ACC. Therefore, while the energy gain from the atmosphere is uniformly distributed over the ACC, the local dynamics in the five hotspots is responsible for large part of the energy release. This result supports importance of the local negative-feedback mechanism of the eddy saturation suggested in Thompson and Garabato (2014) from the energetic viewpoint. The contribution from the barotropic instability is also concentrated in the five hotspots although those values are small compared to the baroclinic instability as mentioned above.

3.2.3. Horizontal distribution of the energy conversion rate

In this subsection, we analyze spatial distributions of each conversion term to explore localized features of eddy-mean flow interactions in more detail. The vertically integrated distributions of the conversion rates (i.e. the BCR, VEDF, and BTR) are presented in Fig. 3-8. The VEDF distributions show widespread positive values in regions downstream of the standing meanders, indicating that the eddy activity is enhanced there and systematically works to flatten isopycnals. It has been shown by Witter and Chelton (1998) that the ridge topography stabilizes the mean flow in the upstream region of the standing meander. This stabilization no longer works in the downstream region and the potential energy stored in the topographically steepened isopycnals is released through baroclinic instability (Rintoul 2018). We revisit this point in Chapter 4.1.2. In Region 2 as a typical example, values of the VEDF exceeds 8.0×10^{-2} W m^{-3} just downstream region of the standing meander at around 80˚E, 54˚S and are larger than 4.0×10^{-2} W m^{-3} at the northern flank of the jet. The area-integrated value of the VEDF in Region 2 reaches 44 GW (Table 3-1), which is about 67% of the local mean wind energy input. The large VEDF concentrated within the hotspots are also shown in other regions,

but their meridional positions are different among each other. While large energy conversions in the VEDF tend to appear in the southern part of the ACC in the Indian sector, they occupy the northern part in the Pacific sector. This difference in the meridional location may result from the relative position of the ACC to the westerlies. Although the ACC axis shifts southward from around 50°S in the Indian Ocean to beyond 60˚S in the South Pacific Ocean, the axis of the westerlies stays at around 55˚S (Fig. 3-4(b)). Therefore, the wind forcing accelerates southern (northern) part of the ACC in the Indian (Pacific) sector. It is also noted that the horizontal distribution of the BCR is collocated with that of the VEDF, indicating that large part of the BCR becomes the net source of the eddy energy.

Similar to the VEDF and BCR, relatively large values of the BTR are confined in regions downstream of the standing meanders as expected from the EKE distributions. For example, the elongated dipole structures of the BTR are observed in the region 47˚S - 50˚S, 33˚E -38˚E (Region 1 in Fig. 3-8), where the contours of sea surface elevation are densely packed together (not shown). The BTR seems to play secondary roles except for Region 3. The area integrated value of the BTR in Region 1, Region 2, Region 4, and Region 5 is smaller than 10% of the VEDF at most (Fig. 3-8). On the other hand, the BTR in Region 3 contributes rather large part of the energy conversions compared to the other hotspots. This is because the ACC jet becomes narrow across the Campbell Plateau and generates the large horizontal current shear, which is favorable condition for the barotropic instability. It is also noted that the negative BTR is observed inside the hotspots as documented in Wu et al. (2017). According to Nakamura (1993) and Youngs et al. (2017), baroclinic eddies in the horizontal shear flow tend to strengthen the horizontal shear through the irreversible barotropic decay of eddies. This effect called the barotropic governor may be reflected in the negative BTR. On the other hand, as noted in Chen et al. (2014) and Matsuta and Masumoto (2021), negative values of the energy conversion rates do not necessarily indicate the mean flow acceleration due to non-locality of eddy-mean flow

interactions. The mean kinetic energy gain from the BTR is not always used locally. It may be transported to elsewhere by non-local interactions or advective process, resulting in no gain of the mean kinetic energy locally.

We now summarize the energy pathway of each hotspot in Table 3-1. Since the energy pathways for Region 1, Region 2, and Region 4 are similar, we examined Region 2 as the representative case. The magnitude of VEDF in Region 2 is as large as 44 GW as seen above, which is comparable to the local wind energy input. This result suggests that the eddy induced density transport effectively weakens the wind-driven isopycnal steepening, which is consistent with the reduced isopycnal tilt inside the hotspots (compare Fig. 2-5(a) and Fig. 2-6(b) as an example). On the other hand, since the barotropic energy conversion rate and the EKE export/import are weak in this region, almost all the converted EKE through the baroclinic instability is dissipated within the hotspots by the viscosity and/or the bottom drag.

Although the baroclinic energy pathway is also dominant in Region 3, the BTR value of 9.5 GW is equivalent to about 40% of the VEDF, suggesting possibility of the mixed barotropic and baroclinic instability in this region. Moreover, the VEDF is suppressed compared to that in Region 2 in spite of the same amount of the wind energy input. Youngs et al. (2017) suggested that the baroclinic conversion tends to be suppressed with the increase in the BTR due to the barotropic governor discussed above. They also showed that contribution from the barotropic instability becomes important with increasing magnitude of the wind stress. With strong wind, the jet becomes narrow and increases its shear, resulting in the favorable condition for the barotropic governor in their idealized model. However, the magnitude of the wind stress averaged over Region 3 in OFES (Fig. 3-9) is 0.19 N/m^2, which is comparable to the value in Region 1 (0.20 N/m^2) and Region 2 (0.20 N/m^2). These results suggest that the width of the jet is more important factor than the magnitude of the wind itself for the onset of the barotropic

instability in OFES. Therefore, it is suggested that the contribution from the barotropic energy pathway may be controlled by the jet structure, which is likely to be associated with the topography. This result is different from Nakamura (1993), who concluded that the jet width has no effects on the barotropic governor.

Before closing this section, it is worth noting that the VEDF in Region 5 shows the largest values among the hotspots although the wind energy input is smaller than the VEDF. The baroclinic energy pathway is also dominant in Region 5 as in the case for the regions in the Indian Ocean sector and the Pacific sector. However, the situation in Region 5 is quite different from the other regions since the ACC shifts large extent in latitudinal direction from 58°S at the entrance to 48°S at the exit of the Drake Passage. The South Atlantic western boundary current called Malvinas Current (Piola and Matano 2001) originates from the ACC region downstream of the Drake Passage, which confluences with the Brazil Current (e.g. Mason et al. 2017). The warm and salty subtropical water originated from the Brazil Current may supply the potential energy to the ACC region. A detailed mechanism of eddy-mean flow interactions in the Drake Passage thus cannot be explained by the local dynamics and needs to be investigated in more detail in a future work.

3.3 APE gain from the westerlies

In the previous sections, the eddy energy is shown to be generated through the baroclinic energy pathway. For the next step, the relationship between the wind forcing and eddy generation needs to be investigated from the energetic viewpoint in detail. In many previous studies, the energy conversion between the mean kinetic energy and the mean APE called the vertical mean density flux (VMDF) $g\overline{w}(\overline{\sigma} - \overline{\sigma_{bg}})$ has been considered as the energy source for the baroclinic instability (Fig. 3-1). The wind energy input to the mean kinetic energy reservoir

is converted to the mean APE through the VMDF, resulting in the baroclinic conversion. Although this interpretation is not wrong theoretically, the magnitude of the VMDF should be treated in practice with its dependency on arbitrarily defined background states. In our case, we obtain 288 GW of the VMDF based on the background state obtained from the global potential density field (Fig. 3-7). However, if we alternatively adopt the horizontal averaging of the time-mean potential density over the Southern Ocean as the background reference field as in Wu et al. (2017), the integrated value of the VMDF reduces to 130 GW. This discrepancy is reconciled by the energy transport associated with the mean pressure flux $\nabla \cdot (\overline{\boldsymbol{u}}\overline{p^*})$, which also depends on the background state. The single use of the VMDF would lead to misunderstanding of the situation.

Therefore, we directly estimate the mean available potential energy (MAPE) generations due to the wind stress based on the wind data and the sea surface height gradient. According to Roquet et al. (2011), the energy input on the geostrophic flow can be obtained as follows:

$$\boldsymbol{\tau} \cdot \boldsymbol{u_g}(z=0) = \boldsymbol{\tau} \cdot \left(\frac{1}{\rho_0 f}\boldsymbol{k} \times \nabla_h p_0\right) \tag{3.26}$$

$$= \boldsymbol{U_E} \cdot \nabla_h p_0 \tag{3.27}$$

$$= \rho_0 g \boldsymbol{U_E} \cdot \nabla_h \eta \tag{3.28}$$

where f is the Coriolis parameter, $\boldsymbol{u_g}(z=0)$ is the geostrophic flow at the surface, $\boldsymbol{k}$ is the vertical unit vector, $\boldsymbol{U_E}$ is the wind driven Ekman transport, p_0 is the surface pressure and η is the sea surface elevation. Assuming the horizontal Ekman flow $\boldsymbol{u}_E$ is vertically uniform within the Ekman layer, the Eq. (3.27) can be rewritten as:

$$\rho_0 g \boldsymbol{U_E} \cdot \nabla_h \eta \approx \rho_0 g D_E \, \boldsymbol{u_E} \cdot \nabla_h \eta \,, \tag{3.29}$$

$$= \rho_0 g D_E \frac{\Delta z}{\Delta t} \,, \tag{3.30}$$

where D_E is the Ekman layer depth, Δt is the time increment, and $\Delta z = -\boldsymbol{u_E} \cdot \nabla_h \eta \, \Delta t$ is the vertical fluctuation due to the Ekman flow against the sea surface slope, which stores the available potential energy in the parcel. Therefore, the energy input on the geostrophic flow of the Eq. (3.28) can be considered as the MAPE generation by the surface wind forcing. The differences between the raw wind energy input $\overline{\boldsymbol{u_0}} \cdot \overline{\boldsymbol{\tau}}$ and the Eq. (3.28), which corresponds to the wind force on the ageostrophic flow, are used to sustain the Ekman spiral against the dissipation in the surface Ekman layer (Wang and Huang 2004; Roquet et al. 2011).

According to Fig. 3-10, the MAPE generation by the Ekman transport are uniformly distributed over the ACC region with its maxima located around Region 1, Region 2, Region 3, Region 4, and the SAF of the Indian sector associated with the closely packed sea surface elevation (not shown). On the other hand, the MAPE generation is relatively small in the Drake Passage, suggesting that the dominant energy source may not be the wind forcing in Region 5. The Ekman work integrated over each hotspot is summarized in Table 3-2. The APE gain over the five hotspots is 35% of that over the entire ACC region, showing the uniformly distributed APE input from the wind. In Region 1, Region 2 and Region 4, where the local baroclinic instability is dominant, the VEDF is comparable to the MAPE generation by the Ekman transport, indicating that large part of the wind energy input to the geostrophic flow is balanced by the baroclinic instability. On the other hand, the VEDF is about 60% of the wind APE input in Region 3, where the mixed instability works. The baroclinic instability in Region 3 may be suppressed in some extent due to the barotropic governor. This remaining 40% of the MAPE gain is stored in the mean stratification or transported to elsewhere. In addition, the VEDF is larger than the APE gain in Region 5. This suggests that, together with the wind stresses, the non-local energy transport from the western boundary current and its extension play a role in supplying the energy in the downstream region of the Drake Passage. These characteristics are also supported by the viewpoint of APE gain from the wind forcing.

Before closing this section, we evaluate whether the Eq. (3.28) represent the APE gain correctly. With simple calculation, we can modify the mean kinetic energy equation of the Eq. (3.11) with the pressure flux equation as is done in Aiki et al. (2016):

$$\frac{\partial K_M}{\partial t} + \nabla \cdot (\overline{\boldsymbol{u}} K_E) + \rho_0 \nabla \left(\overline{u} \overline{u' \boldsymbol{u}'} + \overline{v} \overline{v' \boldsymbol{u}'} \right) = -MHPW - BTR + X(K_M), \tag{3.31}$$

where $MHPW = \overline{\boldsymbol{u_h}} \cdot \overline{\nabla_h p}$ is the mean horizontal pressure work, which represents the net kinetic energy loss by the ageostrophic component of the horizontal velocities in the direction of the mean pressure gradient. It is noted that MHPW is independent of the background states. According to Table 3-2, the MHPW integrated in a typical Ekman layer depth of the 84 m in the Southern Ocean (Roach et al. 2015) is nearly equivalent to the APE gain estimated from the wind stress and sea surface height. It is also confirmed that the integrated values of the MHPW does not change with different values of the Ekman layer depth from 63 m to 208 m. Therefore, it is revealed that the wind stress data can be used as a proxy of the APE gain that is independent from the reference state.

3.4. Summary

In this chapter, we have evaluated the energy pathways in each hotspot associated with the standing meander and over the entire ACC, using outputs of an eddy resolving OGCM. It is shown that the classical LEC includes non-negligible errors in the ACC region, which originates from the large density fluctuations due to the steep isopycnals. Because of this error, the modified diagram developed by Zemskova et al. (2015), which includes the vertical component of the BCR, is more appropriate in the ACC region. Based on this modified energy cycle diagram, it is found that energy conversion related to eddy-mean flow interactions are concentrated on the five hotspots. It is also revealed that the sum of the EKE dissipation in

these five hotspots explains more than 70% of the total EKE dissipation over the ACC region, suggesting that large part of eddies generated in the hotspots die near their nurseries. In other words, the hotspots act as eddy graveyards as the western boundaries in the mid-latitude. The eddy energy dissipation is investigated further in the next chapter.

According to energy conversion rates for each hotspot, we have shown that the five hotspots can be divided into the three types from the energetic viewpoints. In Region 1, Region 2, and Region 4, the EKE is generated through the pure baroclinic energy conversion, whereas the baroclinic and barotropic mixed instability dominates in Region 3. The baroclinic energy conversion is suppressed compared to the energy input from the wind forcing, and the barotropic conversion is responsible for the 40% of EKE generation in Region 3. This difference in the partitioning between barotropic and baroclinic instabilities may be related to the barotropic governor as suggested in Youngs et al. (2017). In Region 5, wind energy input is insufficient to explain the baroclinic energy conversion, suggesting that the non-local process is important in the Atlantic sector. These results suggest that the responses to the changes in wind stress may be different depending on the regions. Although only integrated values of energy conversion rates over the whole ACC region are discussed in previous studies, mechanisms responsible for eddy-mean flow interactions are shown to be different among five hotspots. We thus should treat three types of the hotspots one by one to reveal mechanisms of eddy-mean flow interactions in more detail and their roles in the eddy saturation process.

Finally, we calculated the work done by the Ekman transport and the horizontal pressure work as a proxy of the mean APE gain. The advantage of this quantity against the VMDF is that it is independent from the background states defined arbitrarily. Our results suggest that the westerlies can supply sufficient energy to initiate the baroclinic conversions except for Region 5 near the Drake Passage. It is also shown that the APE gain estimated from the wind

stress and sea surface height is a good approximation to the “true” energy conversion between the mean kinetic energy and APE, suggesting that the APE gain in the ACC region, and in turn the baroclinic conversion rate, can be estimated from the sea surface observations.

Table 3-1. Area-integrated values of the mean wind input, the BTR, the BCR, the VEDF, and the diabatic EKE sink i.e. $X(K_E)$ of the Eq. (3.12) in each hotspot. The values integrated over the five hotspots (*Sum*) and the entire ACC (*ACC*) are also shown.

[GW]	Wind	BTR	BCR	VEDF	Sink
Region 1	48	-0.3	27	24	21
Region 2	66	-2.1	49	44	38
Region 3	64	9.5	26	24	28
Region 4	32	1.5	22	18	19
Region 5	30	1.6	58	51	52
Sum	240	10	182	161	158
ACC	705	5.8	253	220	219

Table 3-2. Same as Table 3-1 but for the MAPE gain by the Ekman transport (*APE gain*) and the MHPW of the Eq. (3.31) integrated within the upper 84m depth.

[GW]	*APE gain*	MHPW
Region 1	29	31
Region 2	39	41
Region 3	41	42
Region 4	23	23
Region 5	18	17
Sum	150	154
ACC	425	438

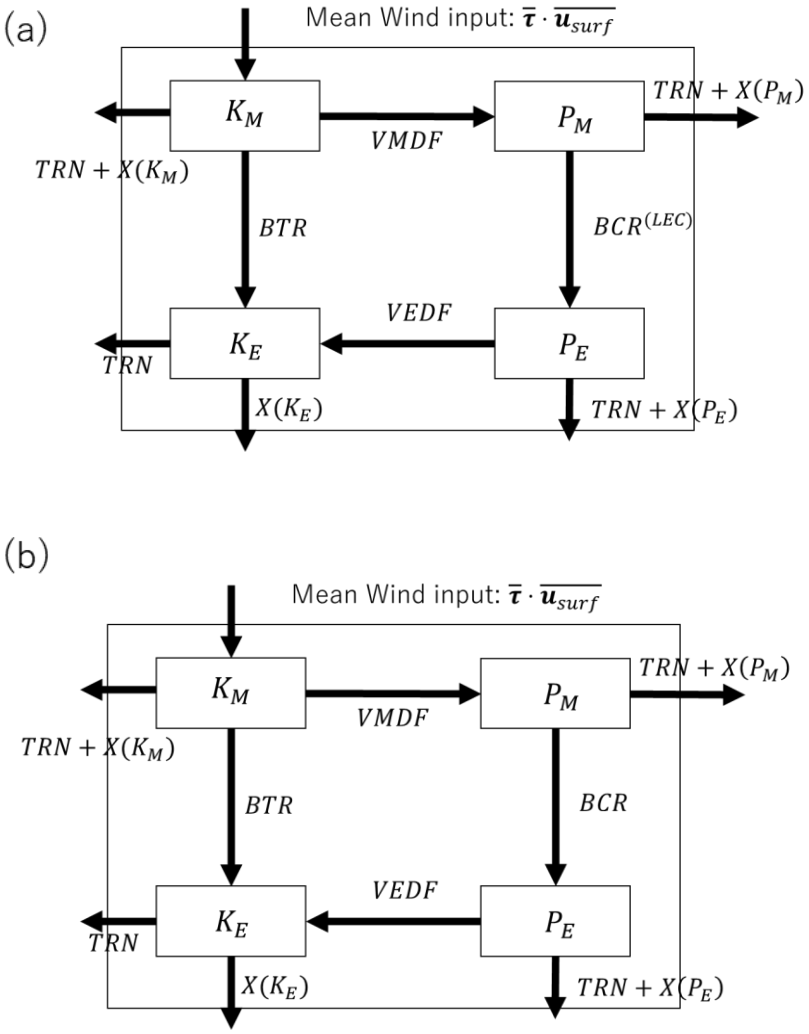

Fig. 3-1. Schematic of energy transfer between mean and eddy kinetic energy and mean and eddy APE from the viewpoint of (a) the LEC and (b) the modified LEC by Zemskova et al. (2015). Black arrows connecting the energy reservoir represent the energy transfer associated with the barotropic conversion (BTR), the baroclinic conversion (BCR), the vertical mean density flux (VMDF), and the vertical eddy density flux (VEDF). Black arrows toward outside of the box indicate the energy sink of the target region due to the adiabatic transport (TRN) and the diabatic source/sink including the surface forcing ($X(\cdot)$). Since we especially focus on the EKE budget in this study, the $X(K_E)$ is distinguished from the transport process.

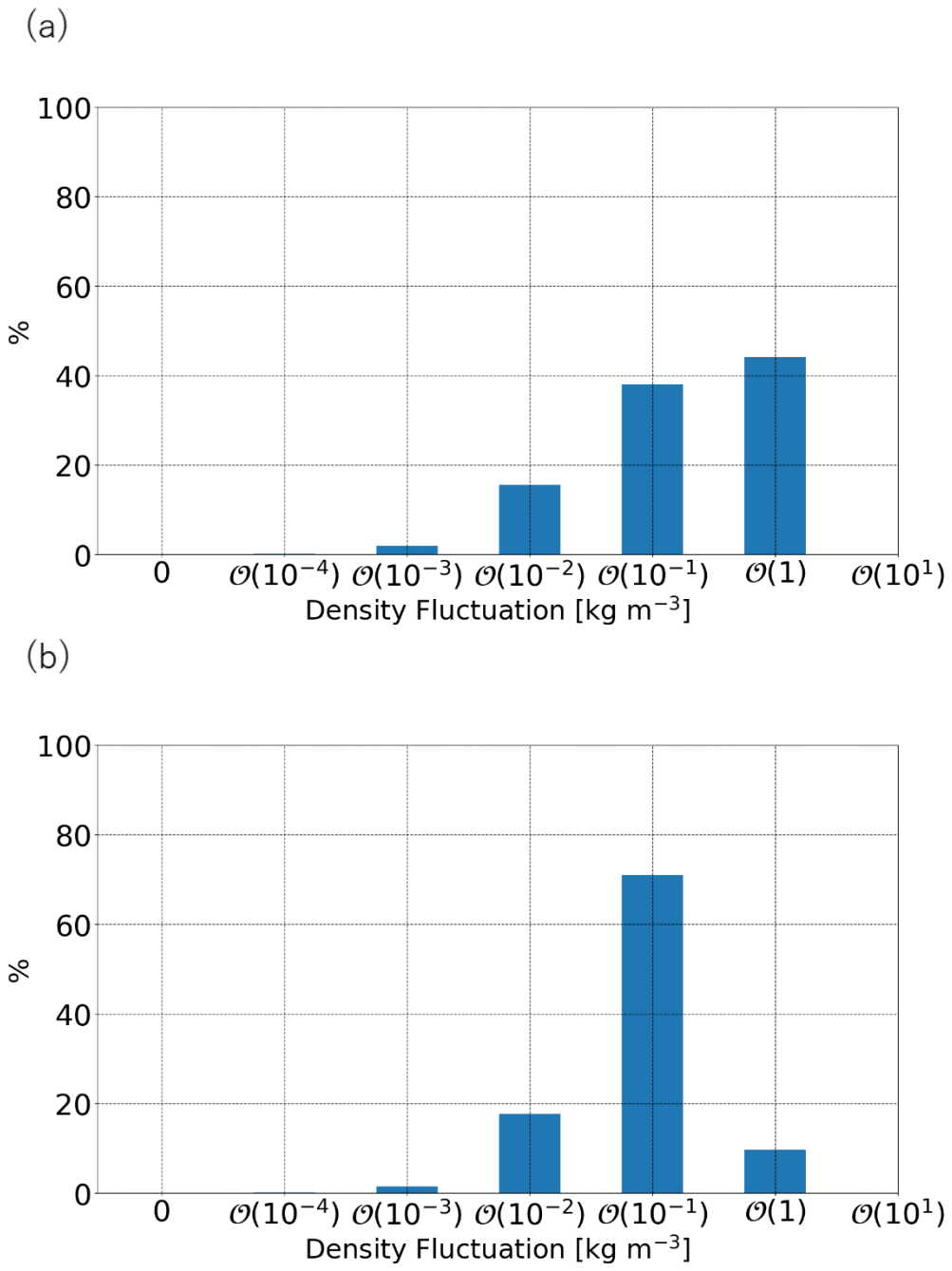

Fig. 3-2 (a) Probability density distributions for potential density fluctuations from the global reference state. (b) is same as (a) but obtained for the layer between 319m and 2119m depth.

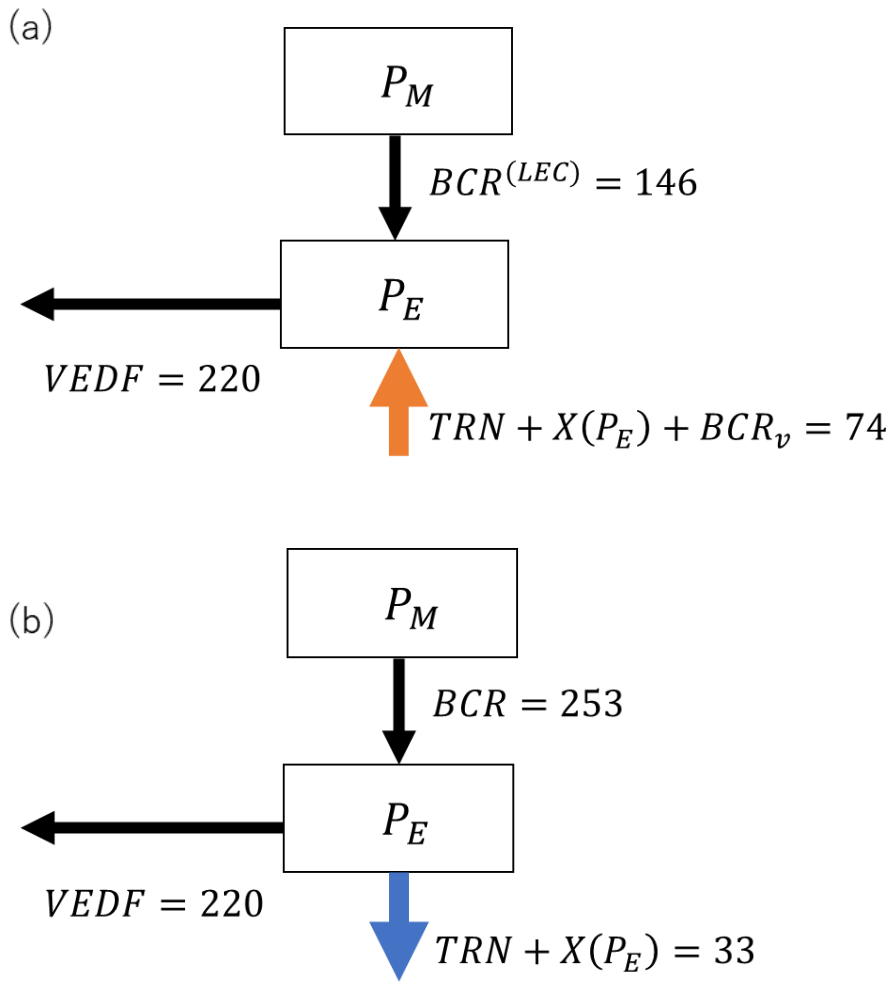

Fig. 3-3. Comparison for the baroclinic energy pathway between (a) the classical LEC and (b) the modified LEC. The unit of each value is GW (10^9W). A red (blue) arrow emphasizes the eddy APE source (sink) for the eddy APE reservoir. The BCR_v of the Eq. (3.24) is explicitly denoted in (a), while this term is neglected in Fig. 3-1(a). The terminology for other components is common to Fig. 3-1.

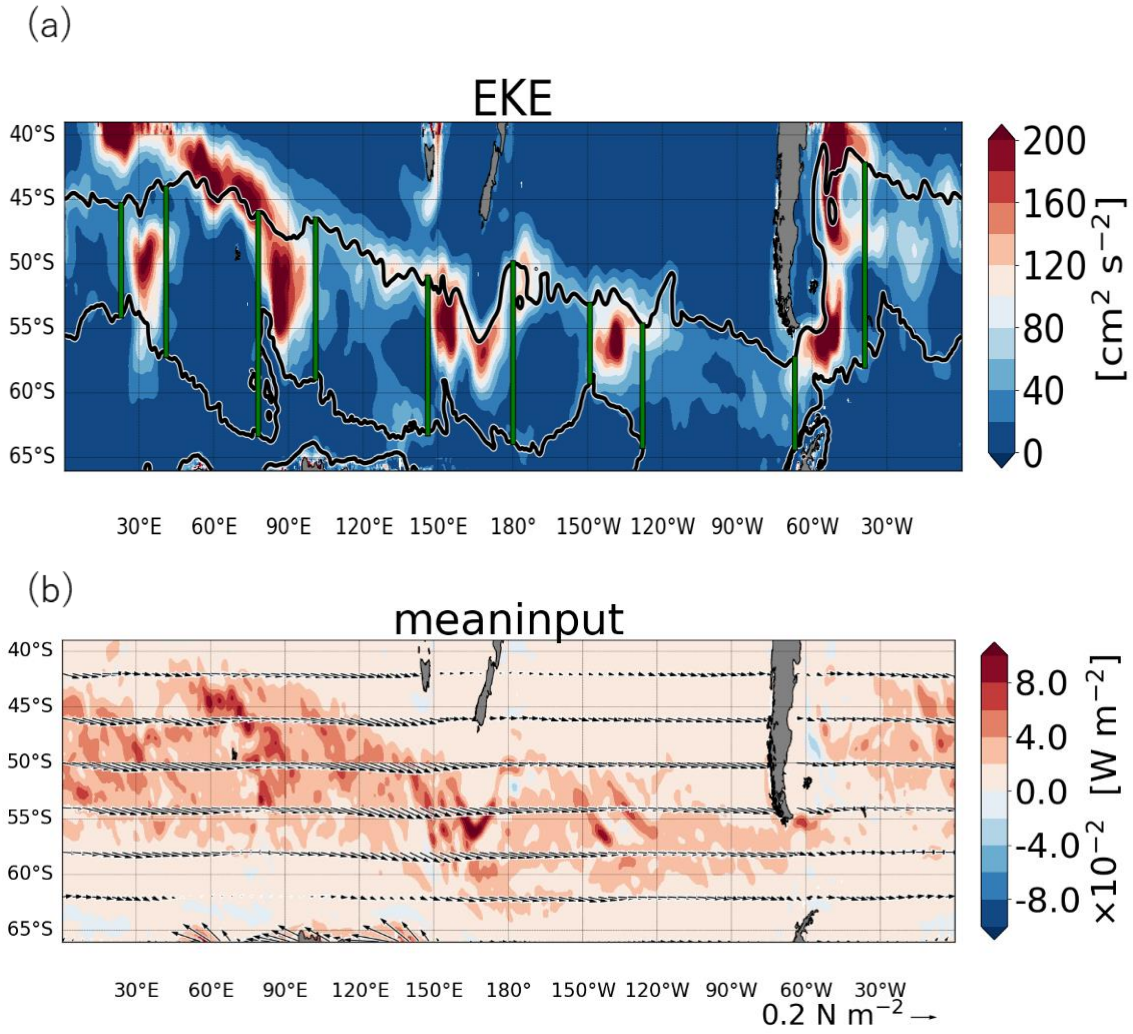

Fig. 3-4. (a) Horizontal distribution of the vertically averaged EKE. The northern and southern black contour represent the Subantarctic Front and the southern ACC Front defined in Chapter 2.2.2, respectively. The five major hotspots named as Region 1 to Region 5 are indicated by the green meridional lines (see Chapter 2.2.2 for the definition of the hotspot). (b) The mean wind energy input with the wind stress vectors represented by the black arrows.

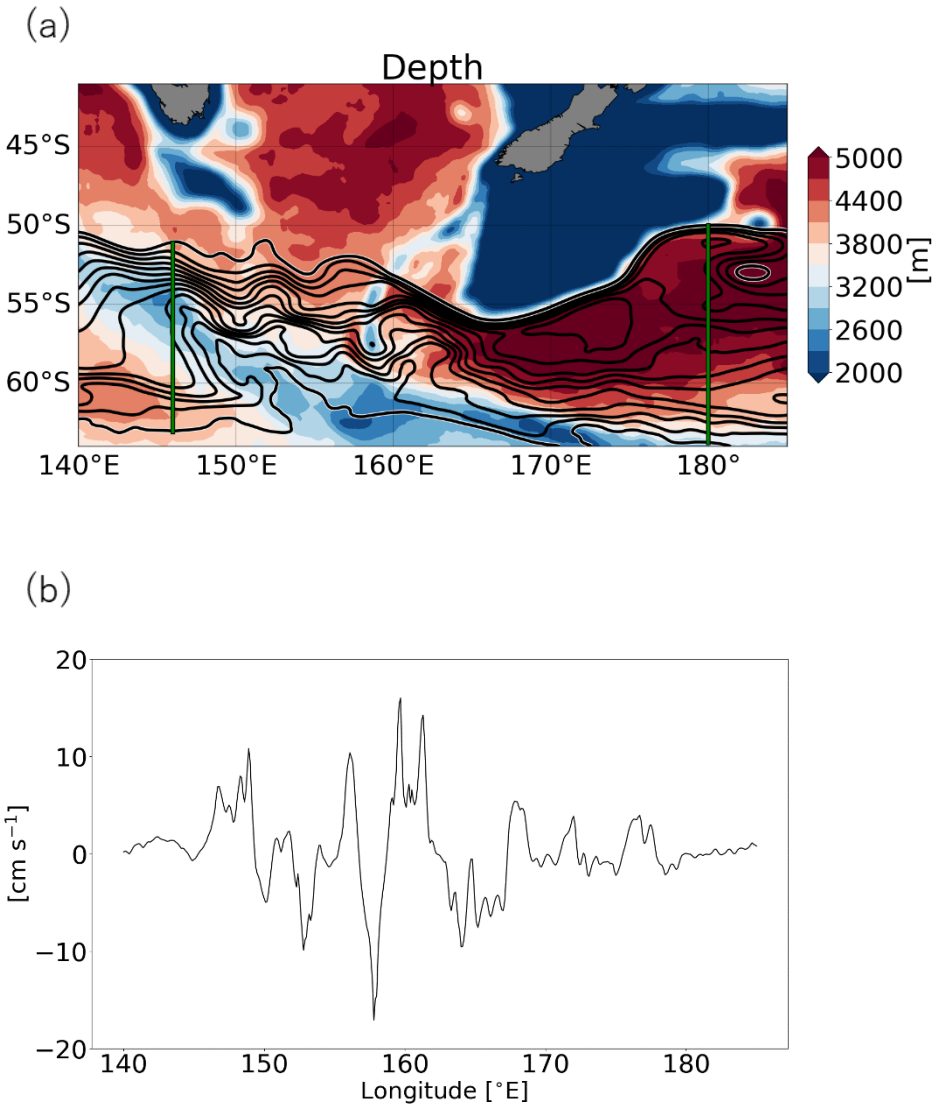

Fig. 3-5. (a) Horizontal distribution of the bathymetry in the region between 140˚E and 185˚E. Black contours indicate the sea surface elevation between −160cm and −30cm from the south to the north with a contour interval of 10cm. (b) Zonal distribution of the mean meridional velocity along the latitude line of 58˚S.

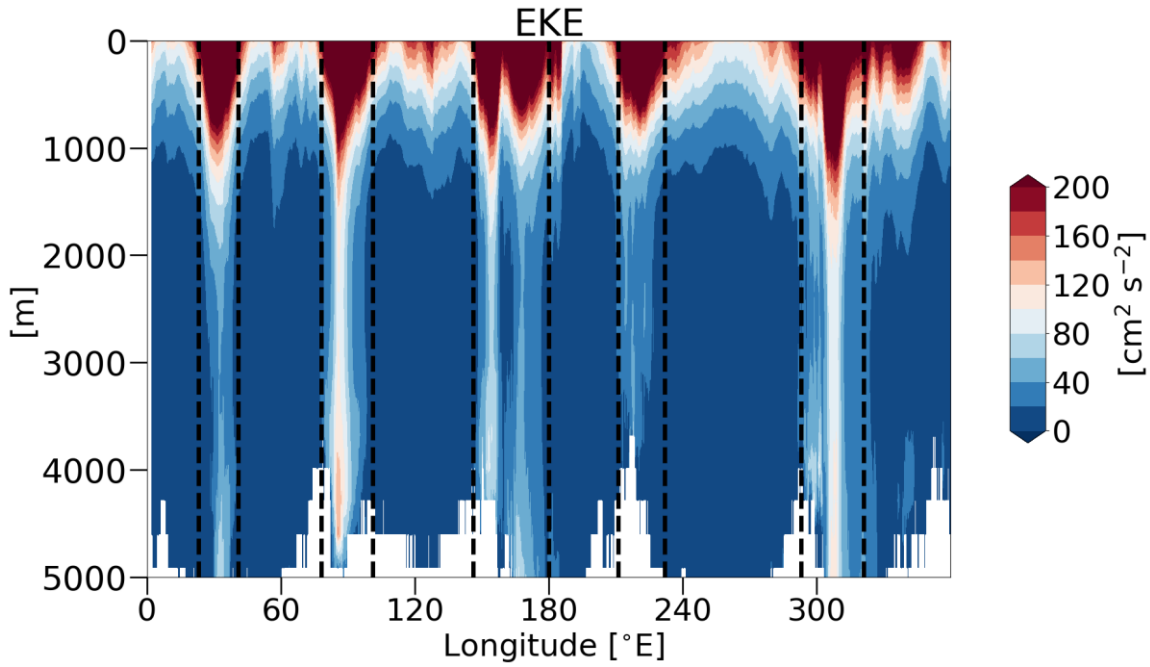

Fig. 3-6. Vertical distribution of the EKE averaged meridionally within the ACC region. Vertical dotted lines indicate zonal boundaries of the hotspots shown in Fig. 3-4(a).

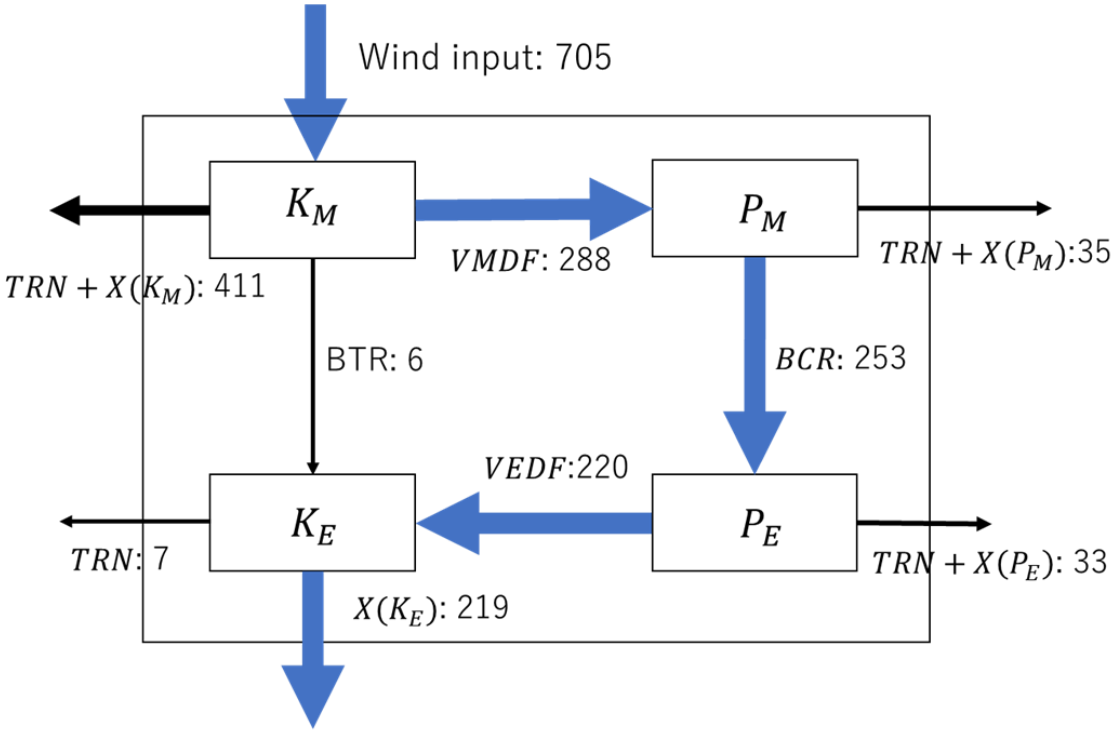

Fig. 3-7. The modified energy diagram in GW (10^9W) calculated over the ACC. The baroclinic energy pathway (Wind input → $VMDF$ → BCR → $VEDF$ → $X(K_E)$) is emphasized by thick blue arrows.

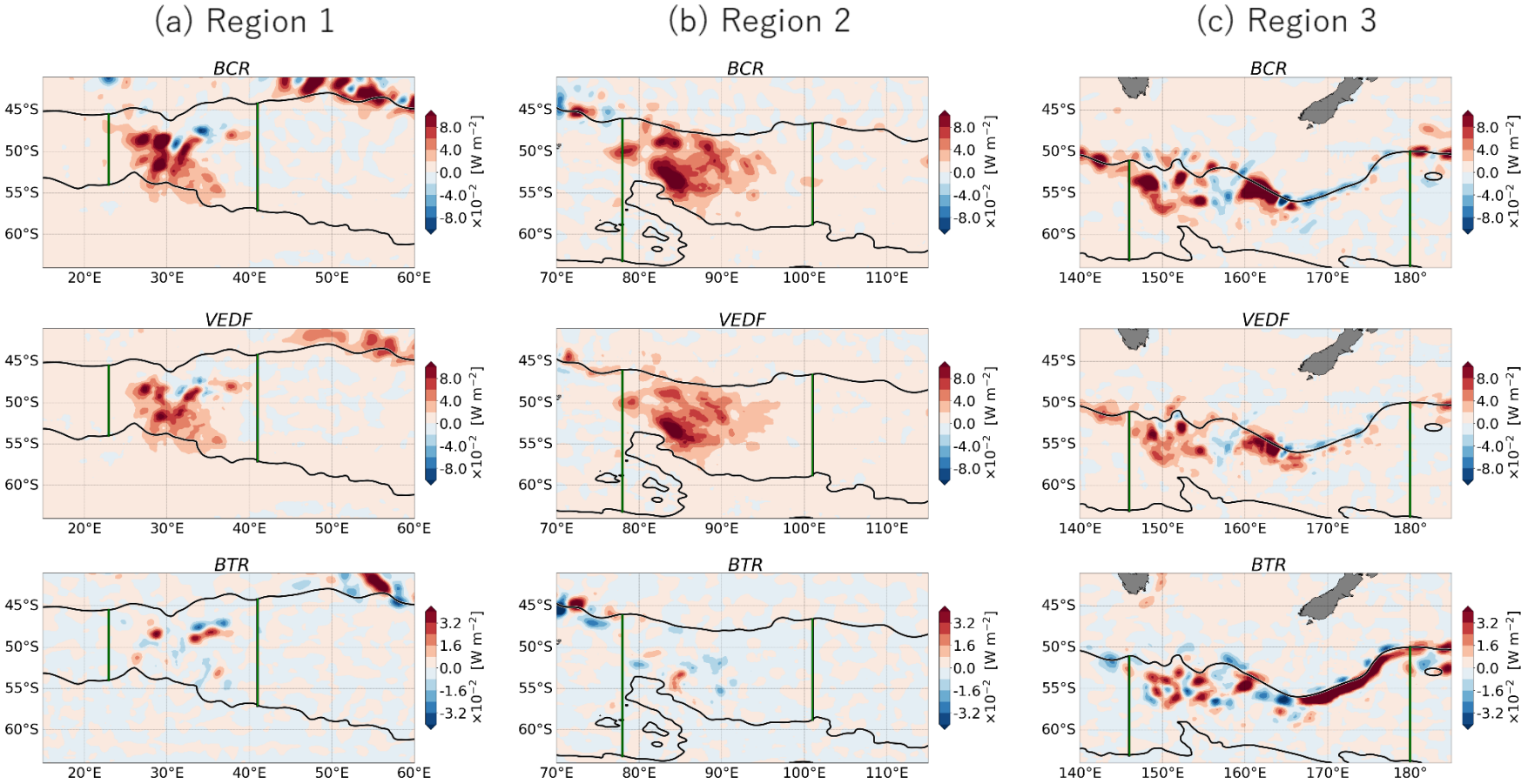
(a) Region 1
(b) Region 2
(c) Region 3
BCR
VEDF
BTR
45°S
50°S
55°S
60°S
20°E
30°E
40°E
50°E
60°E
70°E
80°E
90°E
100°E
110°E
140°E
150°E
160°E
170°E
180°
8.0
4.0
0.0
-4.0
-8.0
3.2
1.6
-1.6
-3.2
×10⁻² [W m⁻²]

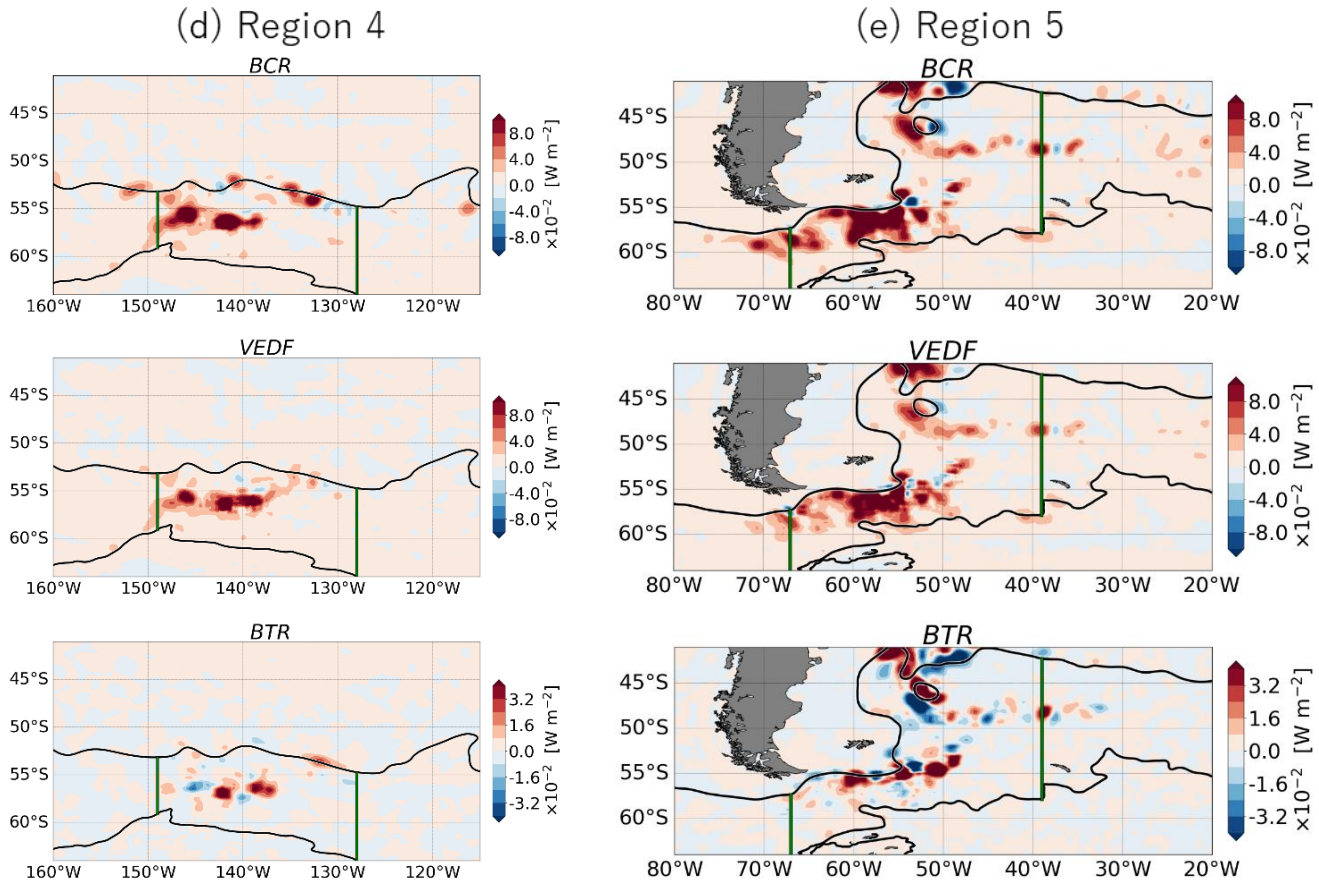

Fig. 3-8. Horizontal distributions of the BCR (top panels), VEDF (middle panels) and BTR (bottom panels) integrated through the water column around the (a) Region 1, (b) Region 2, (c) Region 3, (d) Region 4, and (e) Region 5. Black contours and green meridional lines are same as Fig. 3-4(a).

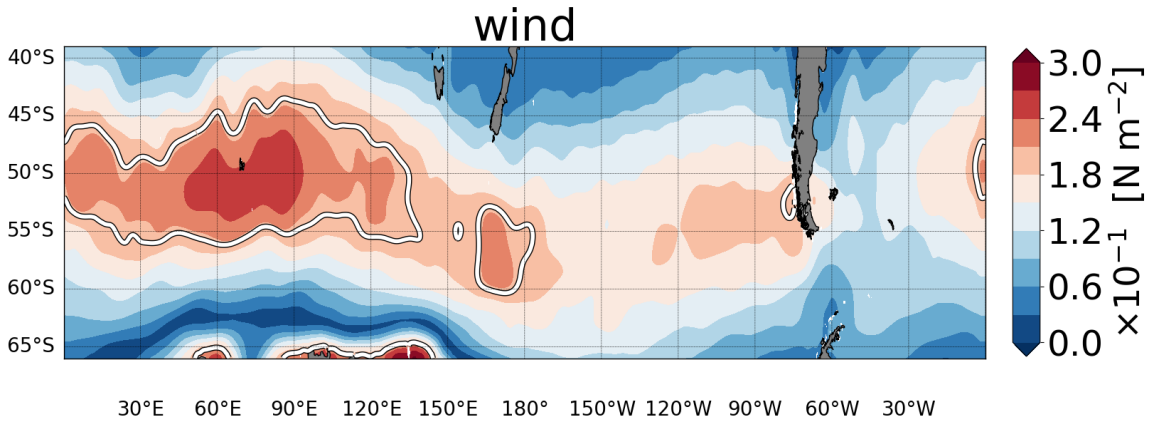

Fig. 3-9. Horizontal distribution of the magnitude of the wind stress. The wind stress exceeds 0.2 N m^{-2} in the regions surrounded by the white contours.

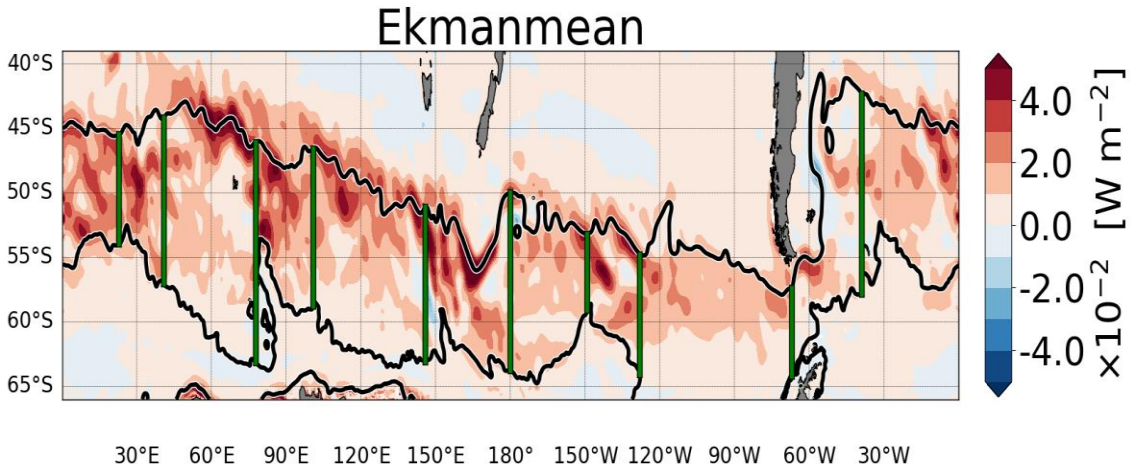

Fig. 3-10. Same as Fig. 3-4(a), but for the MAPE generation due to the Ekman transport.

Chapter 4. Initiation and termination of the hotspots

It is shown in Chapter 3 that large eddy activities in the ACC are concentrated in the five hotspots, which is quite different from the zonally uniform condition. The next question to be answered is how do the eddy activities generate and decay within the hotspots. In order to reveal the initiation and termination mechanisms in the hotspots, we conduct the heat budget analysis to distinguish the mean fields in the hotspots from those in the free zones. Then, we analyze the eddy kinetic energy equation to clarify the process responsible for the termination of the eddy activities in the hotspots.

4.1. Heat budget analysis

4.1.1 Formulation of the heat budget analysis

Previous studies have pointed out that standing meanders steepen isopycnal tilt in the idealized channel models for the ACC (e.g. Bischoff and Thompson 2014). This can be considered as an enhancement of the density gradient due to the upgradient meridional heat flux associated with standing meanders. We call the degree of isopycnal tilt affected by this upgradient heat flux "the baroclinicity" of the mean flow. To explore whether the same situation develops in the realistic OGCM, the thermodynamic equation is considered:

$$\frac{\partial T}{\partial t} = -\nabla \cdot (\boldsymbol{u}T) + H_T, \tag{4.1}$$

where T is the potential temperature, $\boldsymbol{u} = (u, v, w)$ is the three-dimensional velocity, H_T is the change rate of potential temperature due to the vertical mixing parameterized by the KPP scheme and air-sea exchange of heat.

Taking the time-averaging of the Eq. (4.1), we obtain the mean temperature balance as follows:

$$-\nabla \cdot \left(\overline{\boldsymbol{u}T}\right) + \overline{H_T} = 0. \tag{4.2}$$

The time-mean temperature flux can be decomposed into three parts

$$\overline{\boldsymbol{u}T} = [\overline{\boldsymbol{u}}][\overline{T}] + \left(\overline{\boldsymbol{u}}^{*}[\overline{T}] + [\overline{\boldsymbol{u}}]\overline{T}^{*} + \overline{\boldsymbol{u}}^{*}\overline{T}^{*}\right) + \overline{\boldsymbol{u}'T'}, \tag{4.3}$$

where the square brackets [.] denote the zonal average and the superscript * denotes the standing eddy component, i.e. the deviation from the zonal mean (Bischoff and Thompson 2014). It is noted that the "standing eddy" in our formulation does not always indicate stationary waves. It includes all of the zonal variability such as a standing meander. Each term of the Eq. (4.3) is associated with the zonal-mean flux, standing eddy fluxes in parenthesis, and transient eddy flux, respectively. In the zonally averaged view, the zonal-mean flux mainly results from the Ekman heat transport (Volkov et al. 2010; Treguier et al. 2010). The transport of the zonally-averaged temperature by the currents associated with the standing meander $\overline{\boldsymbol{u}}^{*}[\overline{T}]$ and the transport of the standing component of temperature by the zonal-mean flow $[\overline{\boldsymbol{u}}]\overline{T}^{*}$ are also significant for the local dynamics (Bischoff and Thompson 2014), although they vanish in the zonal mean.

To address the depth dependency of the heat balance, we define the cumulative integral of the heat convergence

$$HC(x,y,z) = HC_{zonal} + HC_{stand} + HC_{trans}, \tag{4.4}$$

where each component is defined as the cumulative integral of each component in the Eq. (4.3):

$$HC_{zonal}(x,y,z) = -\rho_0 c_p \int_{H(x,y)}^{z} \nabla \cdot \left([\overline{\boldsymbol{u}}][\overline{T}]\right) dz\,, \tag{4.5}$$

$$HC_{stand}(x,y,z) = -\rho_0 c_p \int_{H(x,y)}^{z} \nabla \cdot \left(\overline{\boldsymbol{u}}^{*}[\overline{T}] + [\overline{\boldsymbol{u}}]\overline{T}^{*} + \overline{\boldsymbol{u}}^{*}\overline{T}^{*}\right) dz\,, \tag{4.6}$$

$$HC_{trans}(x,y,z) = -\rho_0 c_p \int_{H(x,y)}^{z} \nabla \cdot \left(\overline{\boldsymbol{u}'T'}\right) dz\,, \tag{4.7}$$

where $H(x,y)$ is the depth of ocean floor and ρ_0 (c_p) is the reference density (heat capacity) of sea water. The resultant heat balance below the depth z is

$$HC_{zonal} + HC_{stand} + HC_{trans} + Q = 0, \tag{4.8}$$

where $Q(x,y,z)$ is the cumulative integral of all possible forms of diabatic heat convergences obtained as the residual.

Following Bischoff and Thompson (2014), we also define the difference of heat convergence due to standing eddies between the southern and northern part of the ACC:

$$S(x,z) = \frac{1}{2}\left(\int_{y_S(x)}^{y_C(x)} HC_{stand}\, dy - \int_{y_C(x)}^{y_N(x)} HC_{stand}\, dy\right), \tag{4.9}$$

where y_N and y_S are the latitude of northern and southern boundaries of the ACC defined as the location of -30cm cm and -160cm sea surface elevation contours, respectively, as in Section 2.2.2. Also, $y_C = 0.5\,(y_N + y_s)$ is the center of the ACC that approximately follows the Polar Front defined by the -95cm sea surface elevation contour in the OGCM results (Roquet et al. 2011). The negative (positive) sign of S implies a warming (cooling) of the northern part and cooling (warming) of the southern part, respectively, resulting in a tendency for the standing heat flux to steepen (relax) the isopycnal slope. Since this study focuses on the interior ocean, our analysis of the Eq. (4.9) is adopted in the layers below 565m depth. It is confirmed that our results do not change qualitatively if the upper bound changes between 493m and 1113m depths.

4.1.2. The cumulative integral of the heat convergence/divergence

Fig. 4-1 represents the cumulative integrals of heat convergence integrated over the northern and southern part of the hotspots, respectively. The positive (negative) values indicate the warming (cooling). In the northern part, the heat balance is dominated by the balance between the transient and standing eddy components. The standing component works as heating, while the transient eddy component works as the cooling. Both components increase from a depth of 4000 m upward to a depth of 500 m. This vertical distribution is consistent with the deep reaching structure of eddies in the hotspot shown by Fig. 3-6. The zonal mean component, on the other hand, shows the weak contribution lower than 20% of the value of standing component above 3000 m depth. Although the return flow of the Deacon cell transports subsurface waters poleward and contribute to the subsurface warming, this component is insufficient to solely balance with the transient eddy component. The diabatic component is also negligible below the 500 m depth, indicating that the vertical mixing in the interior ocean is very weak. This result is consistent with the observational evidence by Ledwell et al. (2011) who showed the diapycnal diffusivity is small in the thermocline west of the Drake Passage.

The heat balance in the southern part of the hotspots is also dominated by the standing and transient eddy components, but the heating and cooling signs are reversed. The standing (transient) component works as cooling (heating) in the southern part. As a result, the standing component acts to warm the northern part and cool the southern part, which enhances the meridional temperature gradient. In order to quantify the ability of the standing eddy heat fluxes to increase baroclinicity, we estimate the quantity S of the Eq. (4.9). Figure 4-2 shows that S has negative maxima in the longitude band of the five hotspots (emphasized by gray shaded areas), indicating that the dynamical heating and cooling by the standing meander enhances baroclinicity of the mean flow. The zonal anomaly of the EKE averaged meridionally and below the 565 m depth has coherent structures with S. The EKE anomaly increases (decreases)

as S decreases (increases) in the upstream (downstream) region within each hotspot, suggesting that the baroclinicity of the mean flow directly controls transient eddy activities.

Figure. 4-3 shows the heat budget in the free zone. While the baroclinic instability is dominant in the mean heat balance in the hotspots, the transient eddy component is less important in the free zone. According to Fig. 4-3(a), the heating due to the zonal mean component in the northern part is cancelled by the standing eddy cooling instead of the eddy component. Since the width of the ACC is relatively broad in the free zone (Fig. 3-4(a)), the standing eddies relax the isopycnal tilt with $S > 0$ (Fig. 4-2) except for the Southeast Pacific, which counterbalances the isopycnal steepening by the wind-driven upwelling. Although S is negative in the Southeast Pacific, amplitudes of the S are much smaller than those in the hotspots. As a result, the eddy component in the free zone is small, suggesting that the baroclinic instability is less important in the free zone compared to the hotspots. The heat balance in the southern part of the free zone shows the similar tendency of small contribution of the transient eddies.

The heat budget below the 565 m depth is summarized in Fig. 4-4. In the northern part of the hotspots, the standing and transient eddies compensate each other with those magnitudes exceeding 250 TW, whereas the zonal mean component is only 47 TW. In the free zone, the value of zonal mean component is 68 TW, which is comparable to that of the transient eddy component of 63 TW. The sum of the zonal mean and transient eddy component is counteracted by the standing eddies. In the southern part, the transient eddy heating is cancelled by the standing component in the hotspots as is the case for the northern part of hotspots. In the free zone, there is little heat divergence/convergence of each component. Therefore, it is demonstrated that the standing component is responsible for the transient eddy growth, whereas

the large EKE is limited within the hotspots in OFES. These results support the idea suggested by Bischoff and Thompson (2014) in their idealized model.

It should be noted that the standing component of the heat flux originates from the standing meanders. As shown in Sokolov and Rintoul (2007), the ACC is composed from multiple jets, which are merged downstream of significant topographies. A merger of multiple jets results in the upgradient heat flux associated with the standing meanders. For example, while the ACC is composed from several narrow jets at 130˚E (Fig. 4-5(a)), the multiple jets start to join at around 140˚E along the ridge (see the region between 50˚S and 55˚S in Fig. 4-5(b)). These narrow jets are joined in the region between 145˚E and 150˚E to form a relatively wide jet in the latitude band between 53˚S and 58˚S (Fig. 4-5(c)). A merge of the northern and southern branches of the ACC results in the large meridional temperature gradient, which is favorable for the baroclinic instability. It is also worth noting that although the vertical shear of the mean flow is not small in the upstream region of standing meanders (see the region between 50˚S and 55˚S in Fig. 4-5(b) as an example), the growth rates of the unstable modes seem to be reduced in this region. In fact, this region is not included in Region 3 (Table 2-1). This is because the meridional slope (northward deepening) of the topography increases the meridional potential vorticity gradient, which makes the background flow stable (Witter and Chelton 1998), resulting in the relatively weak eddy activities in the upstream region of the standing meanders. In the downstream region of the topography, the jets are no longer stabilized by the topography, and the APE stored in the topographically steepened isopycnals can be released. This is why the intensity of the upgradient heat flux associated with the standing meanders is a good indicator of the instability of the ACC. The schematic figure of this mechanism is shown in Fig. 4-6.

4.2. Downstream decay of the hotspots

In the previous section, we demonstrated that the large EKE is limited within the hotspots in OFES. This result is contrary to the previous studies with the idealized models (Bischoff and Thompson 2014; Chapman et al. 2015), which suggests that large eddy activities are sustained far downstream of the eddy growth site (i.e. the downstream development), in spite of the weak baroclinicity outside of the eddy growth region. Therefore, unlike the idealized models for the ACC, whose results are similar to the atmospheric storm track (e.g. Chang and Orlanski 1993), the hotspots in OFES indicate the "downstream decay" structure of the EKE instead of the downstream development.

In order to investigate mechanisms responsible for the "downstream decay", the EKE budget of the Eq. (3.12) is examined in this section:

$$0 = -g\overline{\rho' w'} - \nabla \cdot \left(\overline{\boldsymbol{u}} K_E + \overline{\boldsymbol{u}' \frac{1}{2} \rho_0 \left(u'^2 + v'^2 \right)} \right) - \nabla \cdot \left(\overline{\boldsymbol{u}_a' p'} \right) + \rho_0 \left[-\overline{u' \boldsymbol{u}'} \cdot \nabla \overline{u} - \overline{v' \boldsymbol{u}'} \cdot \nabla \overline{v} \right] + X(K_E), \tag{4.10}$$

where $\boldsymbol{u}_a = (u_a, v_a, w)$ is the ageostrophic flow. Since the horizontal geostrophic flow is normal to the pressure gradient, only ageostrophic flow contributes to the divergence of pressure flux, i.e. $\nabla \cdot \left(\overline{\boldsymbol{u}' p'} \right) = \nabla \cdot (\overline{\boldsymbol{u}_a' p'})$. The first term in the right-hand-side of the Eq. (4.10) is the VEDF, the second term is the convergence of the advection (ADV), the third term is the convergence of pressure flux (PRESS), the fourth term is the BTR, and the last term is the source and/or sink. Figure 4-7 summarizes the zonal distributions of each component in the Eq. (4.10) integrated meridionally and vertically within the ACC for Region 1 through Region 5. The vertically and meridionally averaged EKE is also shown in Fig. 4-7. As an example, we describe the EKE budget in Region 1 (Fig. 4-7(a)). The EKE shows its maximum near the center of hotspot and decays rather quickly from 40 $\mathrm{cm^2\ s^{-2}}$ to 20 $\mathrm{cm^2\ s^{-2}}$ within the eastern

half of the hotspot. This EKE distribution is governed by two competing processes: growth by the VEDF associated with the baroclinic instability and decay by the dissipation. The horizontal distribution of the EKE has the similar shape with that of the VEDF, which supports the idea shown in Section 4.1 that the baroclinicity of the mean flow directly controls the initiation and termination of the hotspots. The zonal distribution of the VEDF is consistent with the baroclinicity associated with the heat flux of the standing component shown in Fig. 4-2. The VEDF has the maximum with its magnitude exceeding $2.0\ \mathrm{W\ m^{-1}}$ at around 31˚E and decrease suddenly in the eastern half of the hotspot.

The advection and pressure flux also contribute to the EKE distribution. While both advection and pressure flux are not negligible, the advection dominates in the zonal transport (Fig. 4-7(a)). The advection redistributes the EKE from the generation sites in the upstream region west of 31°E with the negative values (i.e. the divergence) towards the downstream region of the hotspots east of 31°E with the positive values (i.e. the convergence). This seems to be responsible for a displacement of EKE maximum from the VEDF maximum by 2˚ eastward. The pressure flux convergence, on the other hand, doesn't work systematically, and its amplitude is smaller than that of the advection, indicating that the energy radiation plays secondary roles in determination of the zonal extent of hotspot. Noting that the total transport of the advection and pressure fluxes (not shown) is not negligible, but its amplitude is small compared to the dissipation. Large part of the EKE generated through the baroclinic instability, therefore, dissipates locally near its generation site.

It should be noted here that the EKE budget for other hotspots (Fig. 4-7 (b)-(e)) is similar to that for Region 1. A sudden transition from strong to weak EKE in the eastern half of the hotspot is also observed in other hotspots. The VEDF seems to be responsible for the initiation and termination of each hotspot except for Region 3, where values of the BTR are larger than

that of the VEDF in the longitude band between 170˚E and 180˚E (Fig. 4-7(c)). Same as Region 1, the dissipation overcomes the transport terms in other hotspots, suggesting that the local energy sink is ubiquitous over the hotspots.

The EKE budget shown above is different from the atmospheric storm track over the ocean. According to Chang and Orlanski (1993), the time-averaged VEDF is confined in the upstream region where the growth rates of unstable modes are large, indicating that the initiation mechanism for the hotspots in OFES is similar to that of the atmospheric storm track. The transport process, on the other hand, is rather different between the present hotspots and the typical storm track. In the atmospheric storm track, a large part of the EKE generated through baroclinic instability is radiated from its generation sites by the pressure flux. The EKE radiated from the generation site expands further downstream with weak convergence of the pressure flux, which sustains large eddy activities even in the region where the mean flow is relatively stable. A possible mechanism of storm tracks termination is the friction over land. Other studies suggest that the barotropic energy conversion from the EKE to the mean flow i.e. the barotropic decay is also responsible for the storm track termination (e.g. Orlanski 1998; Frisius et al. 1998). On the other hand, in the hotspots of OFES, the divergence of EKE due to the advection and the pressure fluxes is small compared to the dissipation in the eddy growth region. Moreover, most of the EKE radiated from the generation site converges in the eastern half of the hotspot as is shown above. This indicates that almost all the EKE generated in the hotspots dissipates inside the hotspots as shown in Table 3-1. The small values or positive values of the barotropic conversion rate (Fig. 4-7) indicate that the barotropic decay is absent in the hotspot of OFES. Therefore, from the energetic viewpoints, it is the local EKE dissipation near the generation sites that distinguishes the simulated hotspots in the ACC from the typical atmospheric storm tracks over the ocean.

The spatial distribution of the advection term integrated vertically supports this idea (Fig. 4-8). Positive (negative) values represent the divergence (convergence). The advection vectors originated from the western half of the hotspots converge into the eastern half of the hotspots, indicating that most of the energy generated within the hotspots cannot pass through the eastern boundary of the hotspots. The pressure fluxes also show the similar distributions (Fig. 4-9). In addition, the ageostrophic pressure fluxes seem to contribute to the formation of the meridional energy distributions as well as the eastward energy transport inside the hotspots. For example, the EKE is supplied from the extension of the Agulhas Return Current at around (47˚S, 83˚E) in Region 2, generating the cross-frontal energy radiation across the SAF. The divergence of the pressure fluxes also shows positive and negative values alternately in the core of the hotspots in all the hotspots, suggesting that the pressure flux works to homogenize the EKE distribution within the hotspots.

In the case of the atmospheric storm track over the ocean (e.g. Chang and Orlanski 1993) and idealized channel models for the ACC (e.g. Chapman et al. 2015), the ageostrophic pressure flux extends downstream without any prominent convergences. This is because the pressure flux convergence during eddy growing stage is balanced by the pressure flux divergence during eddy decay stage, resulting in the near-zero time-averaged values of pressure flux divergence (e.g. Chang and Orlanski 1993; Danielson et al. 2006). However, the time-averaged pressure flux itself is large over the downstream region in such models. This is not the case in OFES. The ageostrophic pressure flux as well as the advection vectors becomes small in the eastern half of the hotspots, leading to the downstream decay.

4.3. Vertical redistribution of the EKE

In order to reveal a detailed mechanism of the EKE sink, we analyze the vertical transport of the EKE. Figure 4-10 shows vertical distributions of the VEDF, the source/sink of the EKE, i.e. $X(K_E)$ in the Eq. (4.10), the divergence of the 3-dimensional eddy pressure flux $\nabla \cdot (\overline{\boldsymbol{u}'p'})$, the vertical derivative of the vertical pressure flux $\partial_z(\overline{w'p'})$, and the divergence of the advection, respectively. Each value is obtained by averaging over the ACC region in the meridional direction. We focus on the Indian Ocean sector including Regions 1 and 2 as a representative case. According to the VEDF distribution (Fig. 4-10(a)), the EKE generation has a deep structure with its maximum strength in the upper 1000m depth and relatively strong values penetrate down to a depth deeper than 3000m. The zonal positions of the active eddy generation area coincide with the locations of the hotspot. The distribution of the source/sink terms (Fig. 4-10(b)) is different from that of the VEDF. Large EKE dissipation indicated by negative values is observed within the layer below 3000m depth inside the hotspots, indicating that the EKE does not dissipate at its birth site. This discrepancy in the vertical location between the energy generation and the energy sink is compensated through a non-local process by the pressure flux (Fig. 4-10(c)). While the energy flux by the pressure flux converges in the lower layer deeper than 3000m depth, it diverges in the upper 3000m depth, where the EKE production is prominent as seen in Fig. 4-10(a). This vertical communication seems to be achieved by the vertical pressure flux, $\overline{w'p'}$ (Fig. 4-10(d)). Inside the hotspots, the vertical eddy energy flux diverges in the upper 3000m depth, whose distribution and magnitude are almost identical to those for the divergence of the 3-dimensional pressure flux. The vertical pressure flux converges below the 3000m depth. The difference between convergences of the vertical pressure flux and 3-dimensional pressure flux is contributed from the horizontal eddy pressure work below the 3000m depth. This overall pattern of downward pressure flux supports the idea that the vertical pressure flux redistributes the EKE from the generation sites in the upper 3000m depth towards the bottom, where the viscosity and bottom friction efficiently work.

Once the eddies evolve to have a deep reaching structure, they can interact with bottom topography. It is noted that the advection of the EKE is confined within the upper 1000m depth (Fig. 4-10(e)). Therefore, while the EKE advection is more important for the horizontal transport than the pressure flux (Fig. 4-7), it plays a secondary role in the vertical EKE redistribution.

Nikurashin et al. (2013) suggested that the interaction between eddies and rough topography dramatically enhances the EKE dissipation compared to the case of the flat bottom. Moreover, Jouanno and Capet (2020) suggested that the downstream development of the storm track in the idealized model is weakened when mesoscale ($\mathcal{O}(10-100\,\mathrm{km})$) topography is represented. Therefore, the unrealistic downstream development of the eddy activities shown in the idealized models of the ACC in previous studies (Bischoff and Thompson 2014; Chapman et al. 2015) is likely to result from the underestimate of the dissipation associated with the topography or the vertical redistribution. On the other hand, it is demonstrated in OFES that the downstream decay results from the vertical EKE redistribution due to pressure flux and the associated eddy-topographic interactions.

The results shown in this and previous sections are schematically summarized in Fig. 4-11. The EKE is generated in the upper 3000m depth by the baroclinic instability. While the advection transports the EKE to the downstream region within the hotspot in some extent, a large amount of the EKE is transported downward by the vertical pressure flux. The EKE converges near the bottom, where eddies dissipate by the bottom friction and the viscosity. In reality, energy dissipation associated with small-scale processes, such as the generation of internal waves by the rough topography (e.g. Trossman et al. 2016), may be important as the energy sink. Since the horizontal viscosity has a substantial contribution to the mean kinetic energy dissipation in OFES (Aiki et al. 2011), it may also play some roles in the EKE

dissipation. This view is also valid for the hotspots in the Pacific and Atlantic sectors. The vertical energy redistributions in these sectors are summarized in Appendix to this chapter.

4.4. Comparison with the Subantarctic Front region

In Sections 4.2 and 4.3, it is shown that eddy activities of the hotspots are characterized as its downstream decay. However, this is not the case for the SAF region as shown below. According to the EKE distribution shown in Fig. 3-4, the EKE is relatively large along the SAF for the free zone. We thus analyze the SAF between 100˚E and 140˚E as an example of the SAF region and discuss reasons for differences between the hotspots and the SAF.

4.4.1. Energetics of the SAF

Fig. 4-12 shows horizontal distributions of the divergence of the advection and pressure fluxes in this region. The convergences of the EKE advection and ageostrophic pressure flux are absent along the SAF, but amplitudes of the fluxes themselves are comparable to those inside the hotspots. This indicates that the eddies propagate to the east without decay in the SAF. The EKE budget for the SAF region, defined as the region surrounded by the blue contours in Fig. 4-12, are also shown in Fig. 4-13. It is confirmed that our results are not sensitive to the definition of the meridional extent of the SAF region. The EKE generation due to the VEDF and the EKE sink due to the dissipation are two dominant terms of opposite sign as in the case for the hotspots, although those values are rather small compared to those in the hotspots. In contrary to the hotspots, the convergence of the EKE advection and pressure flux are negligible, suggesting that eddies propagate towards downstream. Thus, the EKE is almost constant with the value of around 10 $cm^2\ s^{-2}$ along the SAF. The energetics shown here for the SAF region is similar to that of the atmospheric storm track (Chang and Orlanski 1993).

The longitude – time plots of the EKE for the period of 2001-2002 (Fig. 4-14) supports the idea that the VEDF balances the EKE sink to sustain eddy activities, the condition of which is referred to as "self-maintaining". The EKE averaged in the SAF region clearly propagates eastward along the SAF with its phase speed of ~ 5 cm s^{-1}. The instantaneous EKE in this area is confined in the upper layer (not shown). The positive values of VEDF are collocated with the relatively large EKE signals in the downstream region, indicating eddies along the SAF are self-maintaining. On the other hand, in the hotspot, Region 2 for example, the eddy activities have the peaks at around 85˚E and decrease east of 90˚E. The EKE vanishes at around 105˚E, where the eastern boundary of Region 2 is located. The EKE generation associated with the VEDF is also confined within the hotspot, supporting our conclusion in Section 4.2 that the downstream development is suppressed by the efficient dissipation in the hotspot region.

4.4.2. Vertical structures of eddies in the hotspots and the SAF region

The most prominent difference in the eddy characteristics between the hotspots and SAF is the vertical structure. While the eddies in the hotspots have deep structures that reach the bottom, the eddies in the SAF are surface intensified (Fig. 4-15 (a)). In Region 2 for example (Fig. 4-15 (a)), the EKE is intensified near the bottom with its value exceeding 50 cm^2 s^{-2}, suggesting the existence of eddy-topography interactions. The eddy activities are also relatively large in the intermediate layer between 2000 m and 4000 m depths. This vertically coherent structure suddenly vanishes outside the hotspots (see Fig. 3-6). In the SAF, the surface EKE is relatively large, but its vertical structure is confined within the upper 1000 m depth.

The above difference in the vertical structures of the EKE can be explained by the vertical EKE transport. The vertical EKE redistribution in the SAF region is weak compared to that in the hotspots, although it exists (Fig. 4-16). As is the case for the hotspots, the depths of the

EKE generation (shallower than about 1500 m depth) and sink (deeper than about 2500 m depth) are different, and the vertical pressure flux transport the EKE downward. This is because the baroclinic instability always accompanies the vertical EKE redistribution by its nature (Aiki et al. 2016). However, the vertical redistribution is not strong enough for the EKE to become deep reaching.

As shown in the previous researches (Nikurashin et al. 2013; Frenger et al. 2015; Zhang and Nikurashin 2020), the eddy-topography interactions exerted by small-scale and meso-scale topography are responsible for the dissipation of the mesoscale eddies. Since the eddies in the SAF do not interact with topography, they rarely decay. On the other hand, the deep reaching structure of the eddies in the hotspots enhances the eddy-topography interactions, which is likely to be responsible for the downstream decay of the hotspots as shown in Chapter 4.3. It is important to note here that the bottom topography shows the mean depth of 3870 m (3574 m) in the eastern half of Region 2 (the SAF region) with the spatial standard deviation of the bottom relief of 455m (445m). This suggests that the topographic roughness is qualitatively similar between the hotspots and the SAF region.

A factor causing the differences in the vertical EKE redistribution between the hotspots and the SAF is the intensity of stratifications (Fig. 4-15b). Figure 4-17 shows the meridional section across the ACC region at 85°E within Region 2, representing the condition in the hotspots, and at 120°E in the SAF region. The EKE in the SAF is surface intensified at 120˚E and the thermocline in the SAF region is well developed in the upper 1000 to 1500 m depth (Fig. 4-17(b)). On the other hand, along the section in the hotspot at 85˚E (Fig. 4-17(a)), the stratification is rather weak in the southern part of the high EKE region south of 52°S, while the stratification becomes stronger toward north, particularly in the depth range shallower than 1500 m, which is similar to the condition in the SAF region. Associated with this meridional

change in the strength of stratification is the difference in the vertical distribution of the EKE, with the deep structure reaching the bottom in the south and the shallow structure confined in the upper 1500 m depth in the north.

Based on the quasigeostropic turbulence theory and numerical experiences, Smith and Vallis (2002) showed that the vertical structure of meso-scale eddies becomes surface-intensified in the presence of the thermocline, while the eddies become vertically coherently under the weak stratification. Chemke and Kaspi (2016) also found that the barotropic component of the EKE distribution is anti-correlated with the intensity of the vertical stratifications using the ECCO2 state estimate. Our results shown in this section are consistent with these previous analyses and suggest that the intensity of the thermocline, i.e. the stratification, has a key role in determining a degree of vertical energy transport. This is one of the possible mechanisms to determine whether eddy activities develop or decay in the downstream region of the eddy growth sites. The differences between the hotspots and the SAF documented in this section are summarized in Table 4-1.

4.5. Summary and discussion

In this chapter, mechanisms responsible for the initiation and termination of the hotspots are investigated. The heat budget analysis for the mean flow suggests that the standing eddy heat flux is upgradient i.e. the flux enhances the meridional temperature gradient in the upstream region within the hotspots. The transient eddy heat flux works to compensate this standing component, suggesting that the standing component triggers baroclinic instability. Furthermore, it is shown that the large EKE is confined within the hotspots with slight zonal shift to the east of the large baroclinicity associated with the standing heat flux. These results suggest that the hotspots in the ACC are different from the atmospheric storm track. The

atmospheric storm track over the ocean sustains the high EKE values further in the downstream region, where the background flow is relatively stable in the way that eddies modify the mean flow locally and keep their activities against dissipation. The eddy activities in the ACC using the idealized models (e.g. Chapman et al. 2015) also indicate the downstream development similar to the atmospheric storm track. However, it turns out that the EKE suddenly decreases in the downstream region within the hotspots in OFES as well as observations, suggesting that the downstream development doesn't occur in the real ACC.

The EKE budget analysis suggests that the vertical EKE redistribution is responsible for such "downstream decay" of the hotspots. As shown in the schematic figure (Fig. 4-11), the vertical pressure flux transports the EKE from the upper 3000m depth, where the baroclinic energy conversion is concentrated, towards the ocean floor, where the EKE dissipation is active due to diabatic effects. As a result, a large part of the EKE generated in the hotspots is dissipated locally near the bottom. The eddies in the SAF region, on the other hand, are rarely dissipated. Although the energy fluxes are comparable to those in the hotspots, they do not show any divergence or convergence signals and just propagate along the SAF. This is consistent with the results in Chapter 3, which indicates that the free zone plays a minor role in the EKE dissipation over the ACC. These findings are summarized in the schematic figures in Fig. 4-18.

The differences in vertical structure of the eddies possibly leads to the differences in the eddy activities between the hotspots and SAF region. While eddies in the SAF region are surface intensified, eddies in the hotspots reaches the bottom due to the vertical pressure flux, which enables the EKE dissipation through the eddy-topography interactions. It is also shown that the important factor affecting the vertical EKE redistribution process is the intensity of the

stratification, which is consistent with the results in the previous studies (Smith and Vallis 2002; Chemke and Kaspi 2016).

In reality, the energy conversion to small scale motions associated with rough topography may play an important role for the bottom dissipation as shown in the previous studies (Nikurashin et al. 2013; Zhang and Nikurashin 2020). However, since the bottom dissipation process is parameterized by the KPP scheme in OFES, the rough topography may not be a necessary condition for the downstream decay. According to Chang and Orlanski (1993), the strong bottom friction suppress the downstream development of atmospheric storm tracks. In addition, Aiki et al. (2011) pointed out that the horizontal viscosity plays an important role for the dissipation of the mean kinetic energy in OFES. The horizontal viscosity may also play a major role in the EKE dissipation. Therefore, the dissipation process of the EKE should be addressed in a future work.

The unrealistic downstream development of the hotspot in the idealized models for the ACC is likely caused by the unrealistic stratifications of the thermocline and underestimation of the dissipation. In several idealized models (e.g. Abernathey et al. 2011; Bischoff and Thompson 2014; Jouanno and Capet 2020), the temperature is relaxed toward an exponential profile ranging from $0°\mathrm{C}$ at the bottom to $8°\mathrm{C}$ at the surface with a scale height of 1km in the sponge layer at the northern boundary. This temperature profile with a fixed thermal expansion coefficient of $\alpha = 2.0 \times 10^{-4}\ \mathrm{K}^{-1}$ gives the buoyancy frequency larger than the value in the hotspots in OFES (Table 4-2). While the buoyancy frequency of the idealized models is comparable to the value in the SAF region in OFES at 1041m, it is stronger at 2119m. The stronger background stratification in these idealized models contributes to suppress the vertical redistribution of the EKE. Even if the eddies become deep reaching, the EKE is difficult to dissipate at the bottom when the ocean floor is completely or nearly flat, which is a typical

condition in such idealized models (e.g. Bischoff and Thompson 2014; Chapman et al. 2015). In addition, both the horizonal and vertical viscosity are usually rather small in these models. All these factors contribute to simulate the downstream development conditions in the idealized models. Furthermore, since Chapman et al. (2015) demonstrated that the zonal extent of the topographies has small effects on the zonal length of the storm track in their idealized model, the zonal length scale of the topographies is not likely the cause of the different behavior of the hotspot in OFES and the idealized models. Therefore, our results suggest that the eddy saturation and/or compensation mechanisms based on such idealized models may be unrealistic. The eddy saturation and/or compensation mechanisms should be revisited in the future work with the models including rough topographies and appropriate stratifications.

Appendix to Chapter 4. Vertical redistribution of the EKE in the Pacific and Atlantic sectors

According to Fig 4A-1, the pressure flux in the Pacific Ocean sector plays a similar role to that in the Indian Ocean sector. The divergence (convergence) of the pressure flux (Fig 4A-1c) in the upper (lower) layer can reconcile the mismatch between the EKE generation (Fig 4A-1a) and sink (Fig 4A-1b). However, there are several differences from other hotspots in the Region 3, while the Region 4 has the same characters as the hotspots in the Indian sector. In the longitude band between 170˚E and 180˚E, the difference between the 3-dimensional (Fig 4A-1c) and vertical divergence of the eddy pressure flux (Fig 4A-1d) is prominent in the intermediate layer between 2000m and 3000m. This may result from the relatively large barotropic conversion rate (Fig. 4-7c). Although the large BTR is confined in the upper 1000 m depth (not shown), the barotropic process suppresses the baroclinic conversion as discussed in Chapter 3, which reduces the downward energy transport. In the Atlantic sector, on the other hand, the vertical structures are similar to those in the Indian sector (Fig 4A-2), because the baroclinic instability is dominant in the downstream region of the Drake Passage as shown in Chapter 3.

Table 4-1. Comparison for the eddy activities between the hotspots and the SAF region in OFES.

Characteristics	Hotspots	SAF region
Downstream structure of the eddy active region	Downstream decay	Downstream development
Vertical structure of eddies	Deep	Shallow
Vertical stratification	Weak	Strong
Topography	≈ （Mean and variability of the depth are comparable）	

Table 4-2. Comparison for the buoyancy frequency between OFES and idealized models at 1041m and 2119m.

Model	Buoyancy Frequency (s^{-1})
OFES hotspots	1.0e-3 (1041m) 0.4e-3 (2119m)
OFES SAF	2.5e-3 (1041m) 1.0e-3 (2119m)
Idealized models (e.g. Abernathey et al. 2011)	2.4e-3 (1041m) 1.4e-3 (2119m)

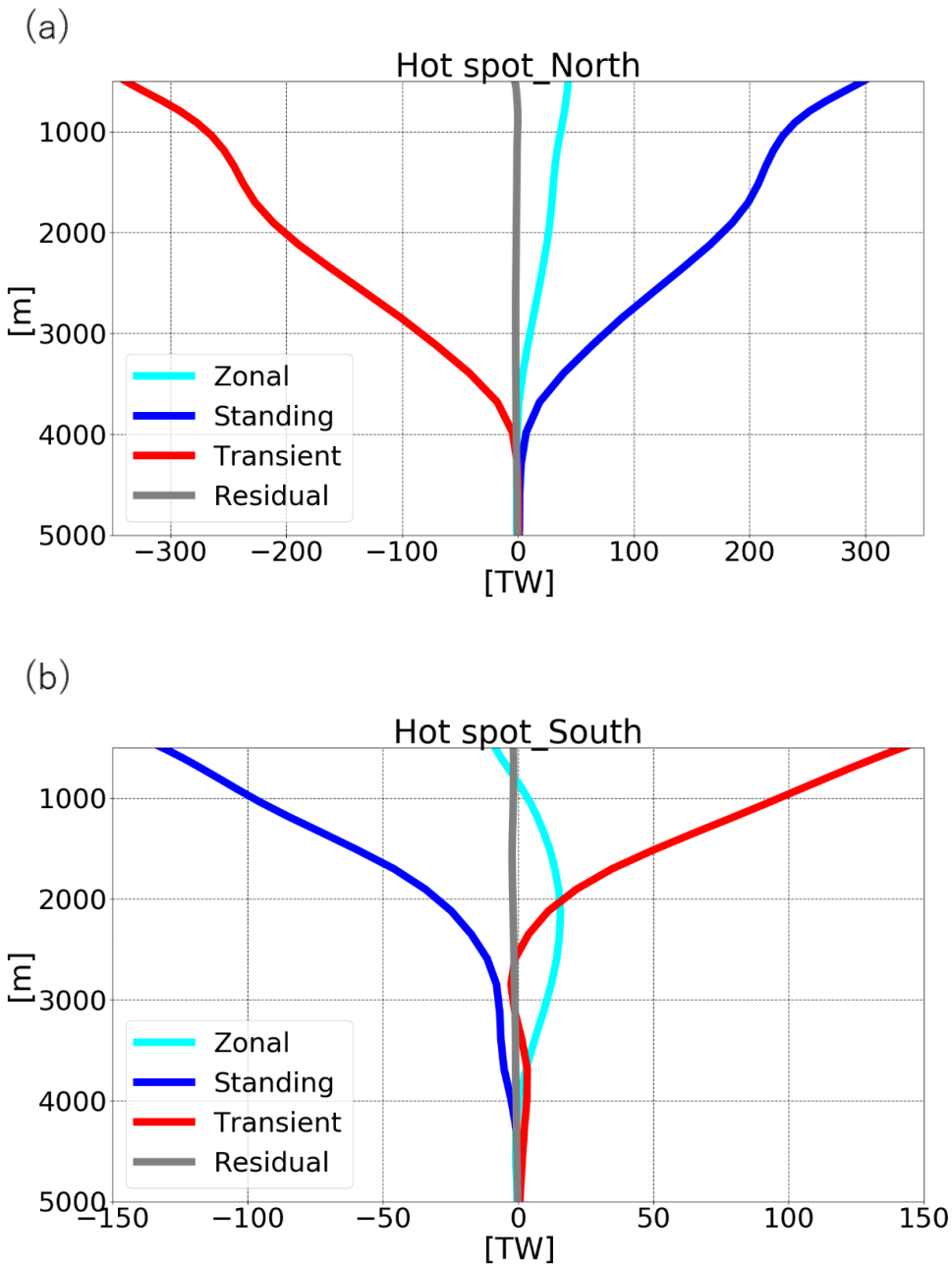

Fig. 4-1. Vertically cumulative of the heat convergence from the bottom over (a) the northern and (b) the southern parts of the five hotspots. Cyan, blue, red and gray lines represent the zonal mean component, standing eddy component, transient eddy component, and the diabatic component, respectively. It is noted that the scale of the horizontal axis of (a) and (b) are different.

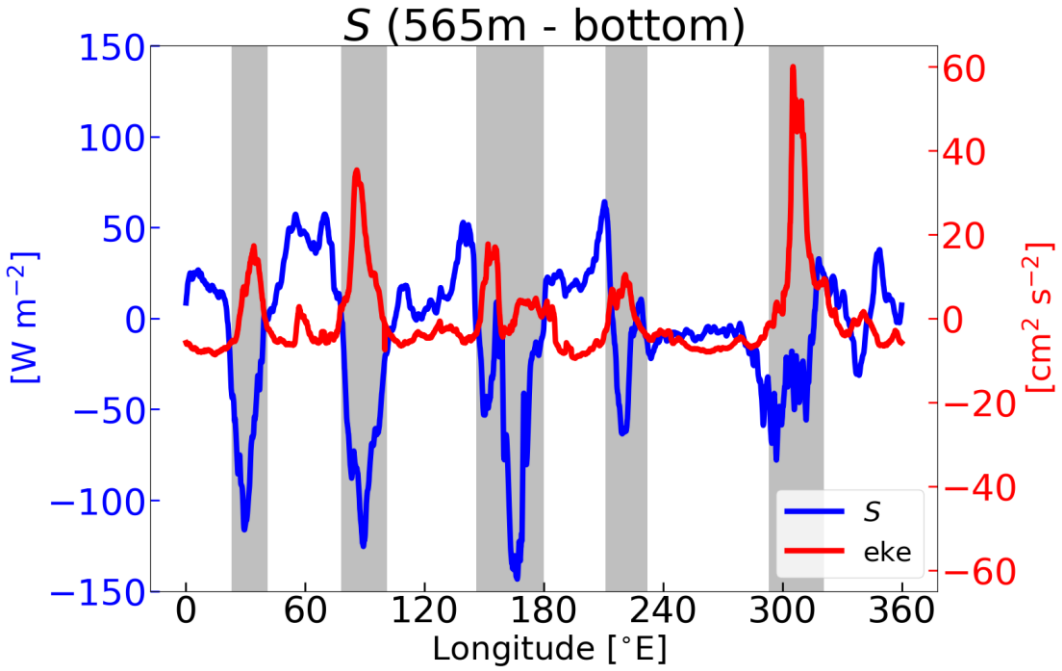

Fig. 4-2. Zonal distributions of the S defined in the Eq. (4.9) and EKE anomalies from the zonal mean below a depth of 565 m. Each distribution is smoothed with a 10˚ zonal running mean. The gray shaded areas indicate the five hotspots, respectively.

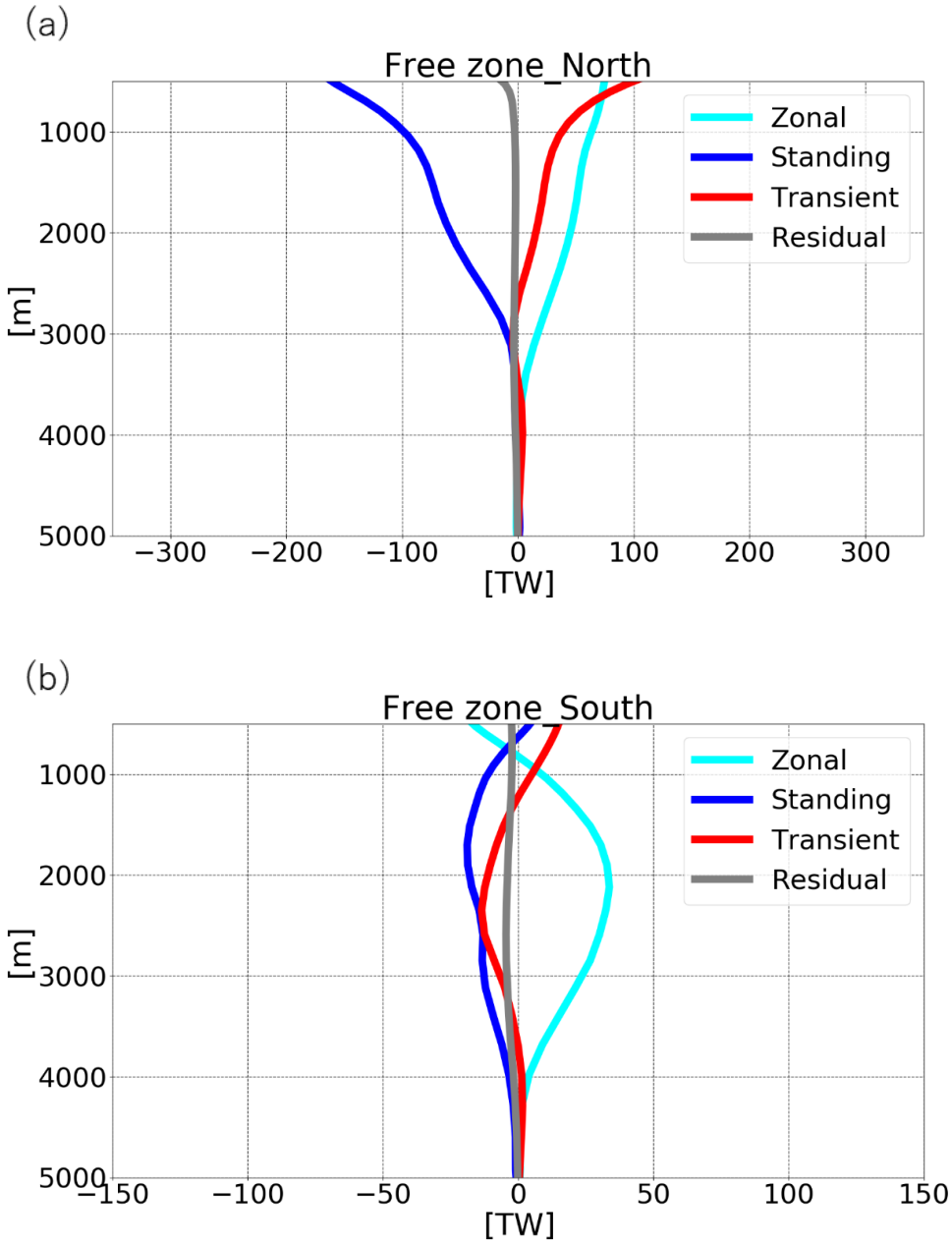

Fig. 4-3. Same as Fig. 4-1 but for the free zone.

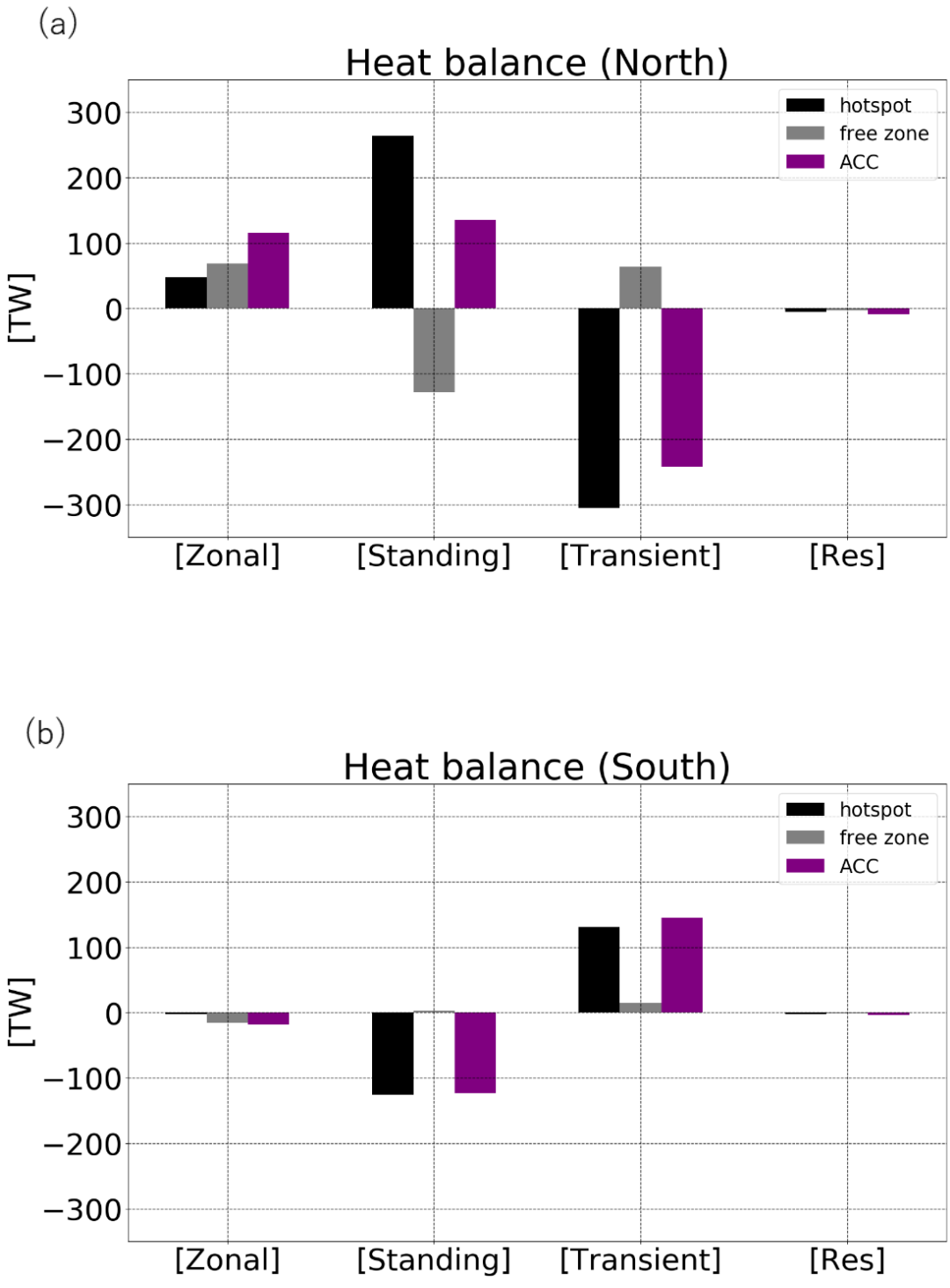

Fig. 4-4. Area- and depth-integrated values of the heat budget components over the hotspots (black bars), free zone (gray bars) and over the ACC (purple bars) integrated below a depth of 565 m in (a) the northern and (b) the southern part of the ACC region.

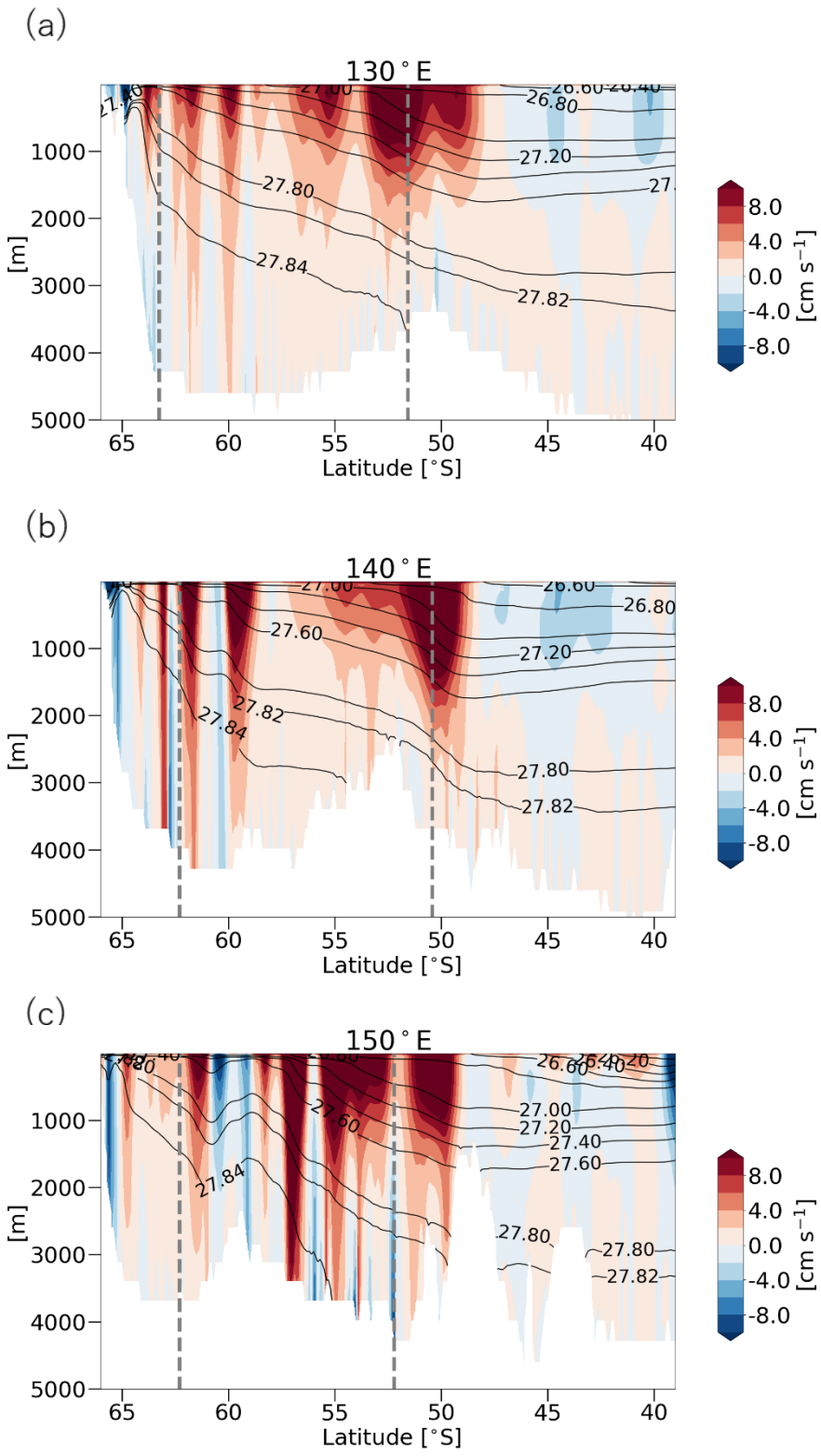

Fig. 4-5. Meridional sections of the mean zonal velocity along (a) 130˚E, (b) 140˚E and (c) 150˚E. Black contours represent the potential density referenced to the surface at the same section. The gray dashed lines at the north (south) indicate the SAF (sACCf)

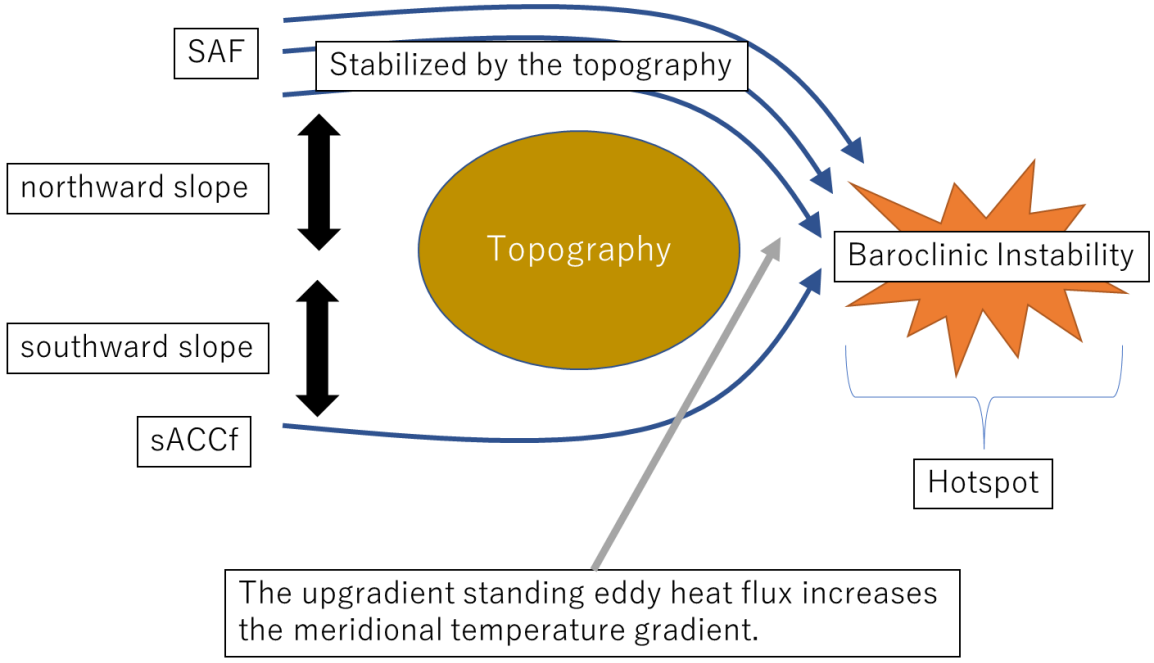

Fig. 4-6. Schematic summarizing the initiation mechanism of the hotspots. In the upstream region of the standing meander, the ACC is stabilized due to the northward downslope of the topography although multiple jets are merged along the SAF. The multiple jets are merged in the downstream region of the topography i.e. the hotspot. In the hotspot, the upgradient heat flux associated with the standing meander increases the meridional temperature gradient, which allows the mean flow to be unstable since the ACC is no longer stabilized by the topography.

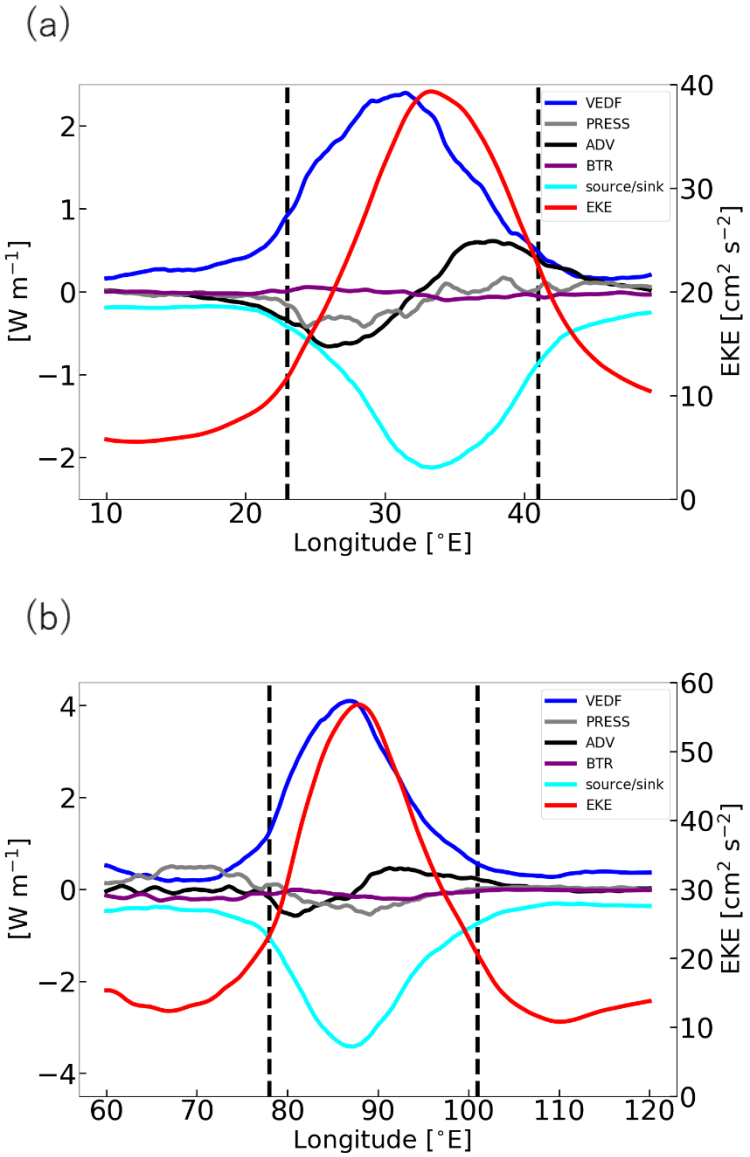

Fig. 4-7. Eddy kinetic energy budget summaries integrated vertically and meridionally in the envelope of the ACC around the five hotspots, respectively. Zonal distributions of the EKE averaged meridionally and vertically within the ACC envelope are also shown by red lines. Each distribution is smoothed with a 10˚ zonal running mean.

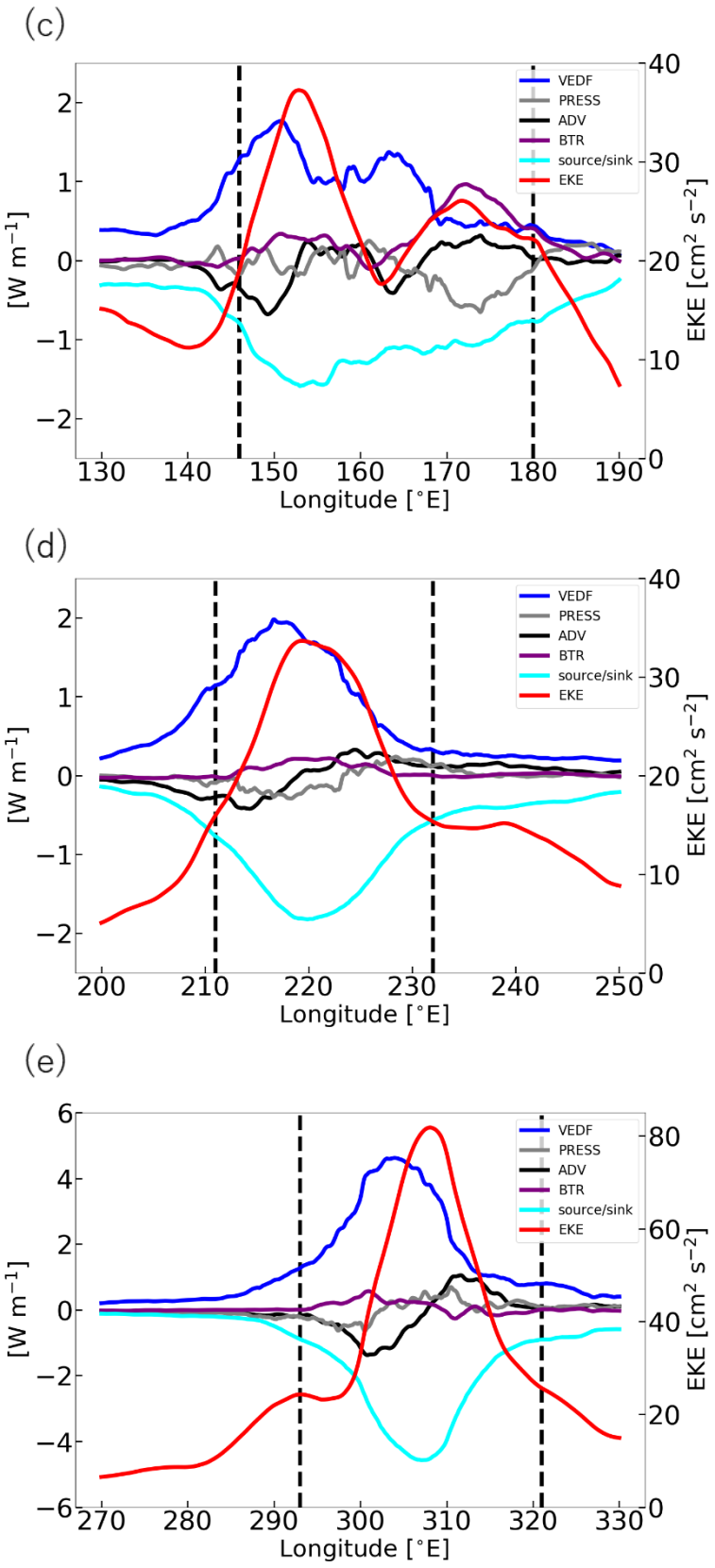

Fig. 4-7. (continued)

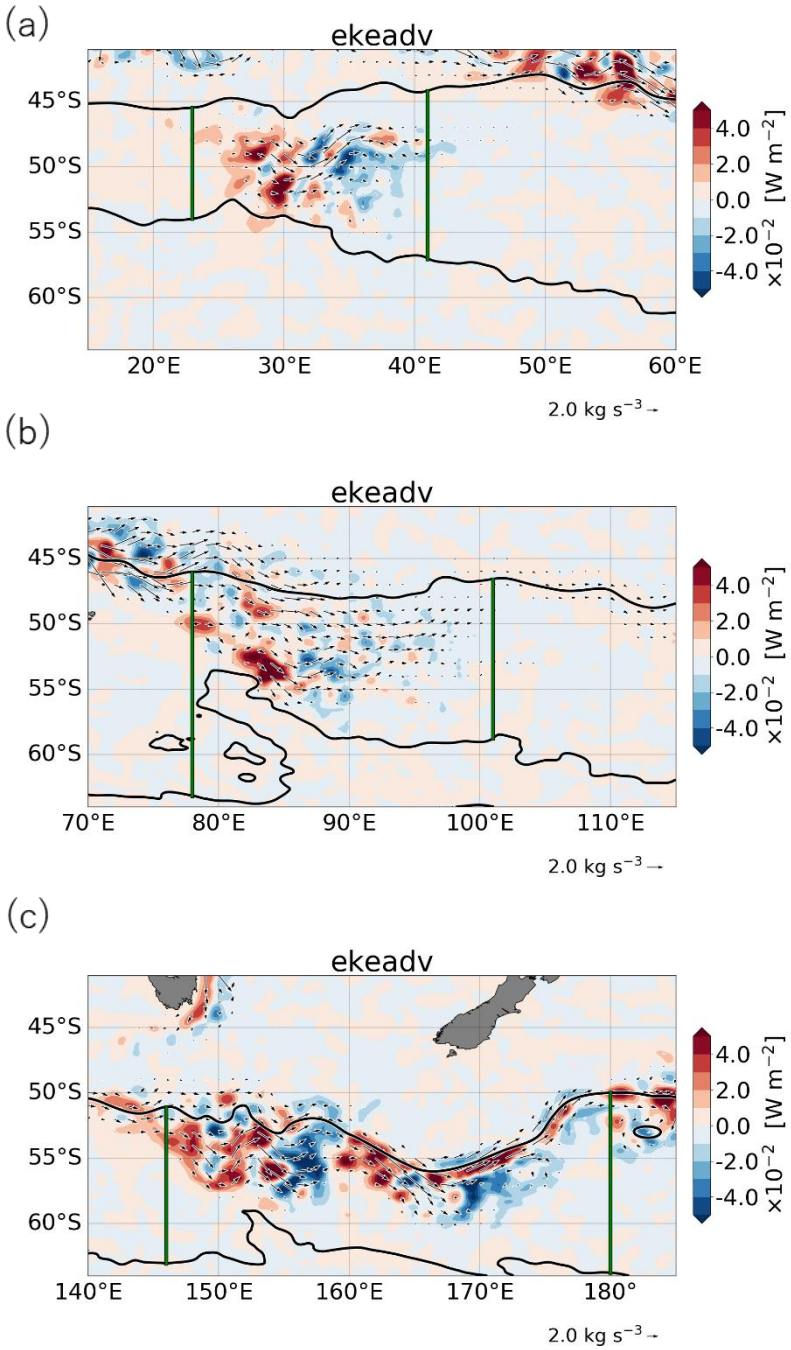

Fig. 4-8. Horizontal distributions of the divergence of the EKE advection integrated through the water column around five hotspots. Black arrows indicate the eddy advection flux vectors integrated through the water column. Vectors smaller than 0.2 kg s^{-3} are masked. The black contours and meridional green lines are the same as those in Fig. 3-4(a).

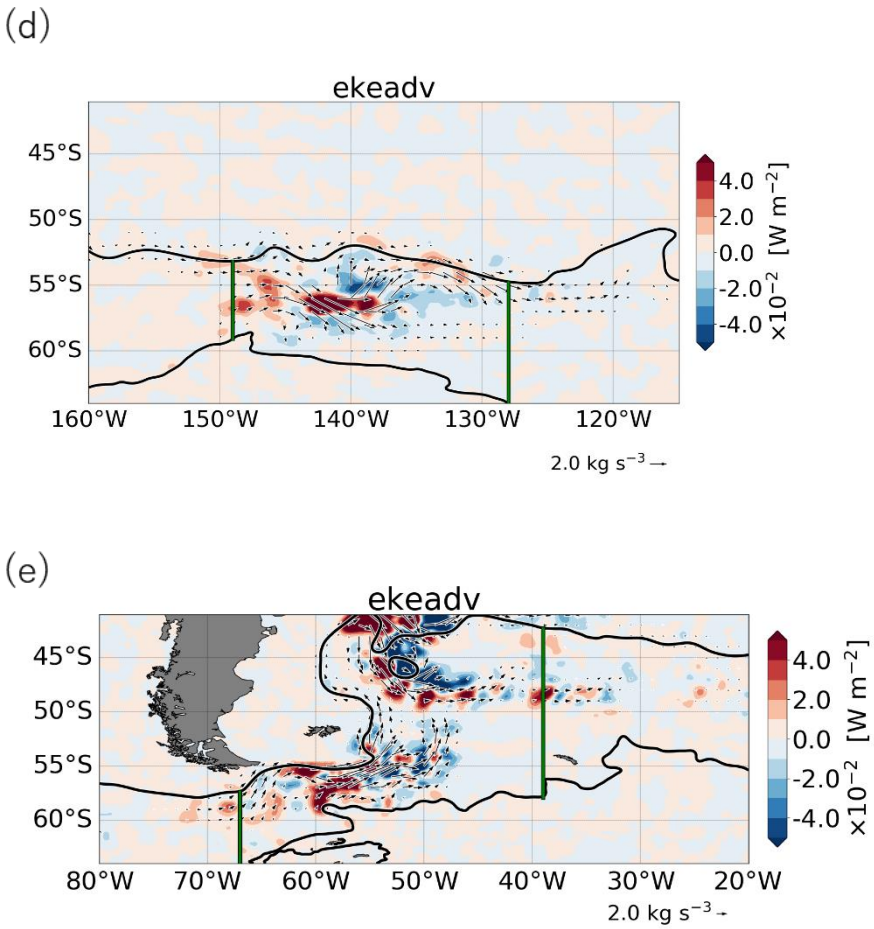

Fig. 4-8. (continued)

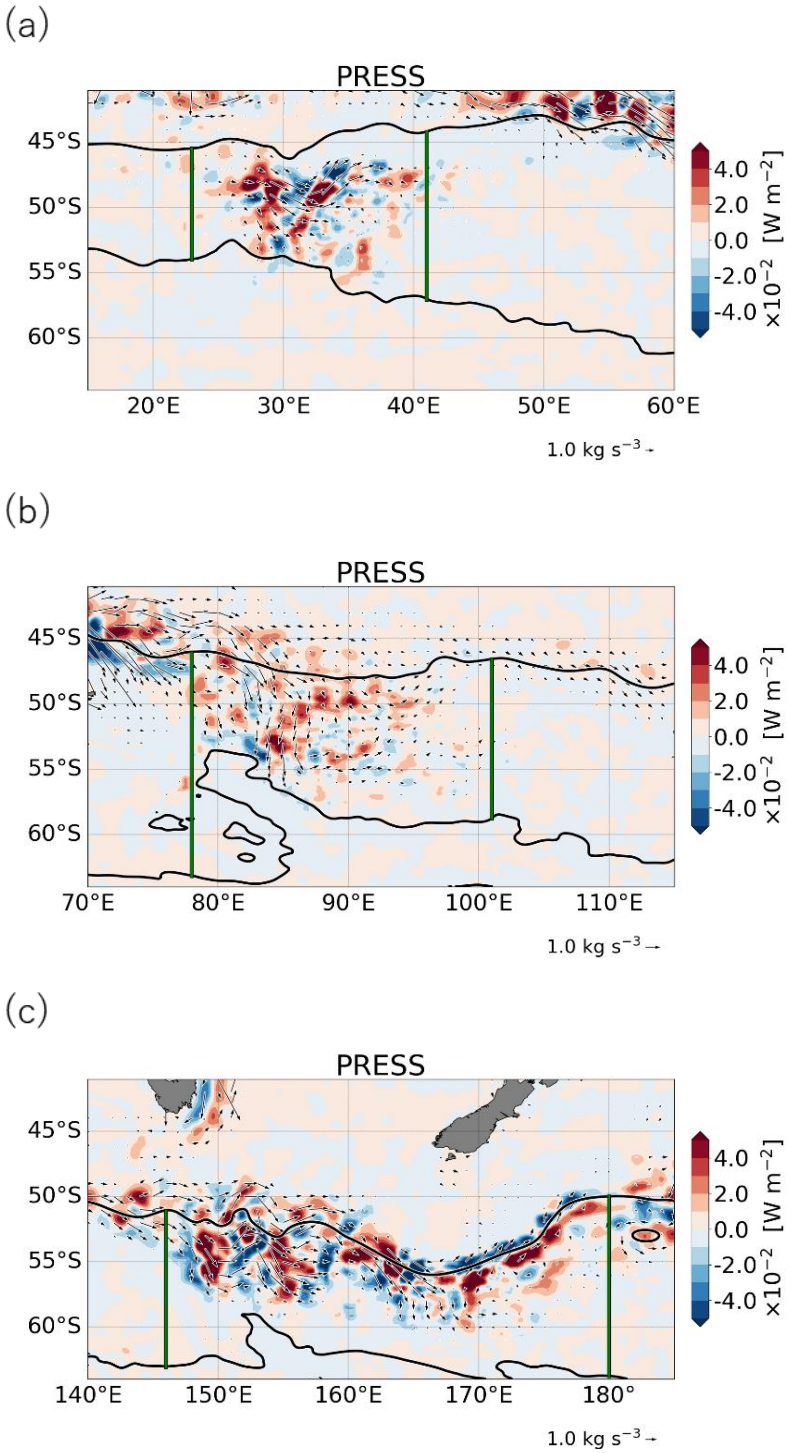

Fig. 4-9. Same as Fig. 4-8 but for the pressure flux divergence and pressure flux vectors.

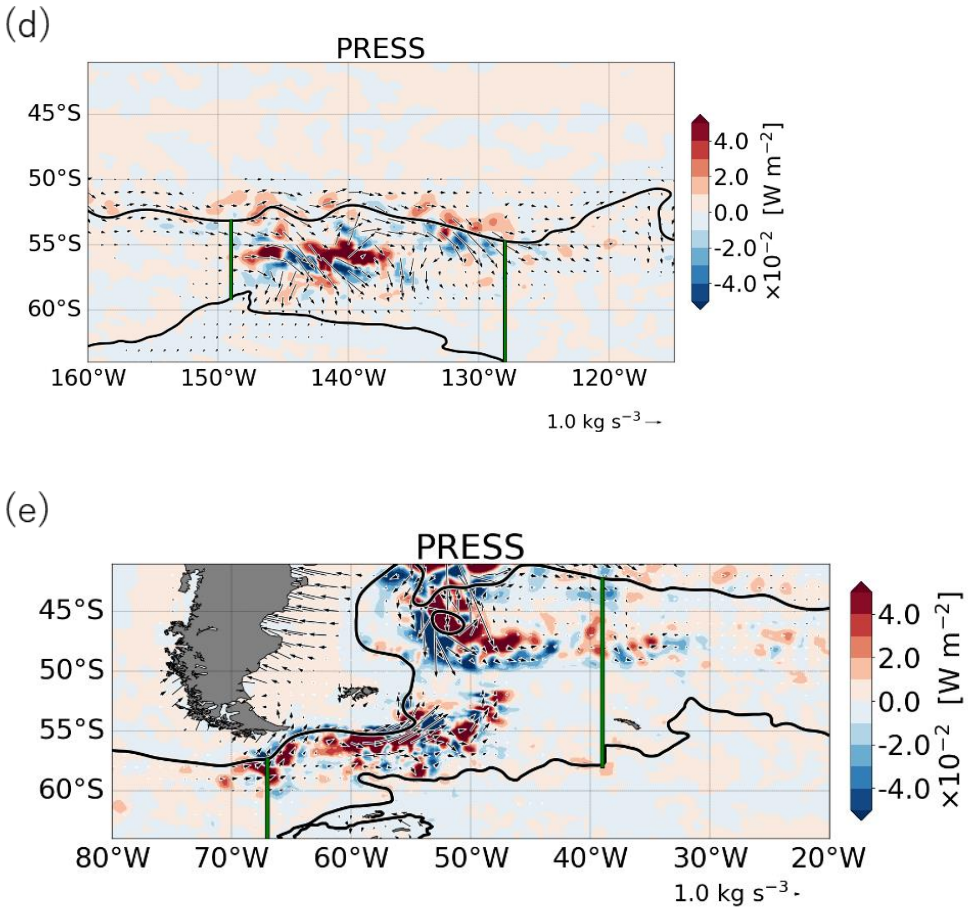

Fig. 4-9. (continued)

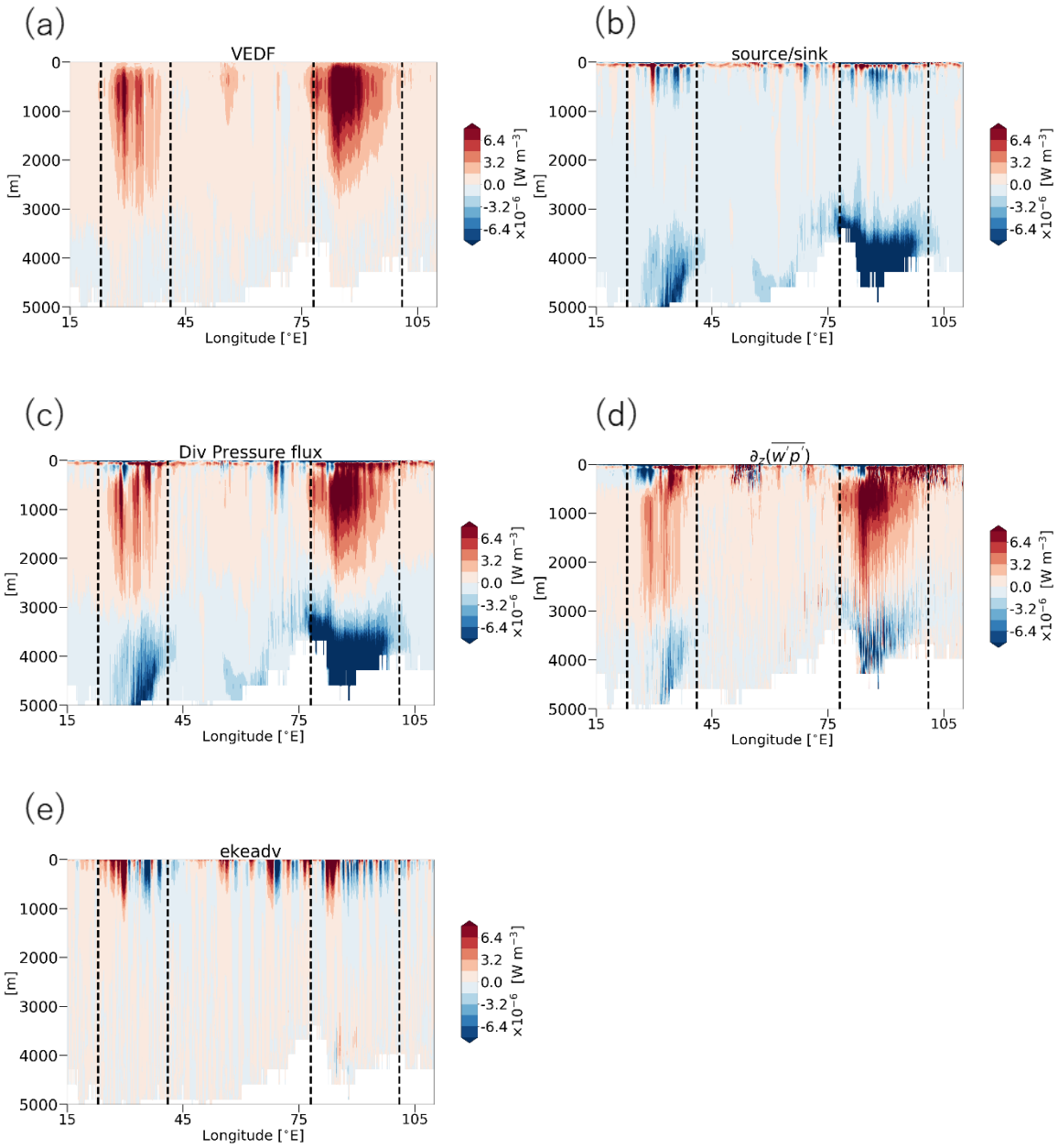

Fig. 4-10. Vertical distributions of (a) the VEDF, (b) the EKE sources/sinks, (c) the divergence of the pressure flux, (d) the vertical derivative of the vertical pressure flux, and (e) the divergence of the eddy advection averaged meridionally in the envelope of the ACC. The vertical black dotted lines at 23˚E, 41˚E, 78˚E, and 101˚E indicate the western and eastern boundary of the Region1 and Region2, respectively.

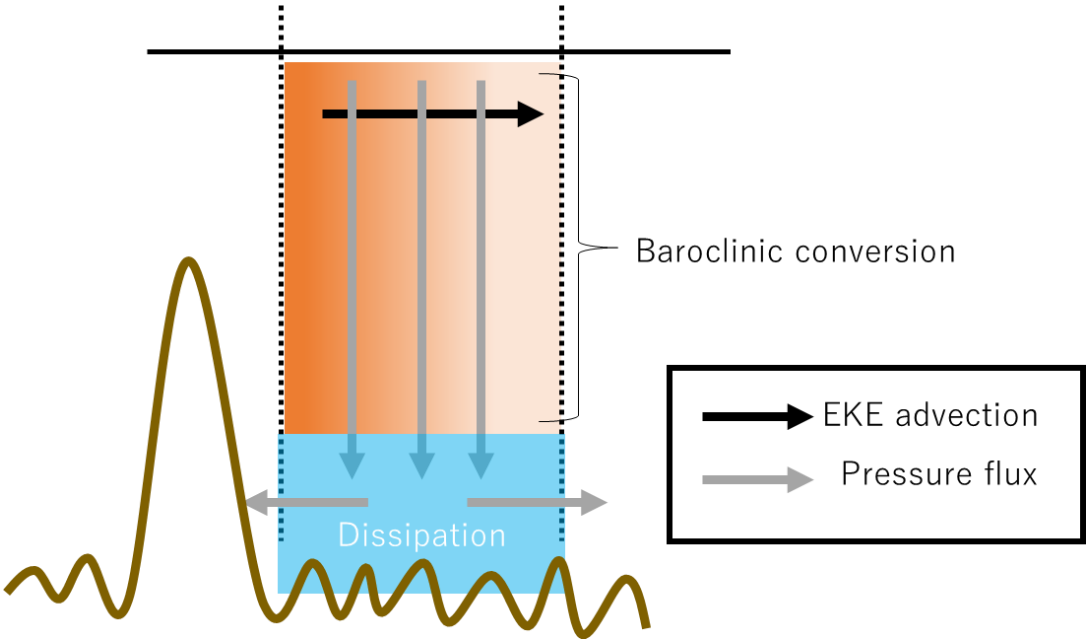

Fig. 4-11. Schematic summarizing the EKE transport in the hotspots. The red (cyan) area indicates the region where the baroclinic energy conversion (energy dissipation) occurs. A black arrow indicates the horizontal transport dominated by the advection, while the gray arrows indicate the energy flux by the pressure. See the main text for the detailed explanation.

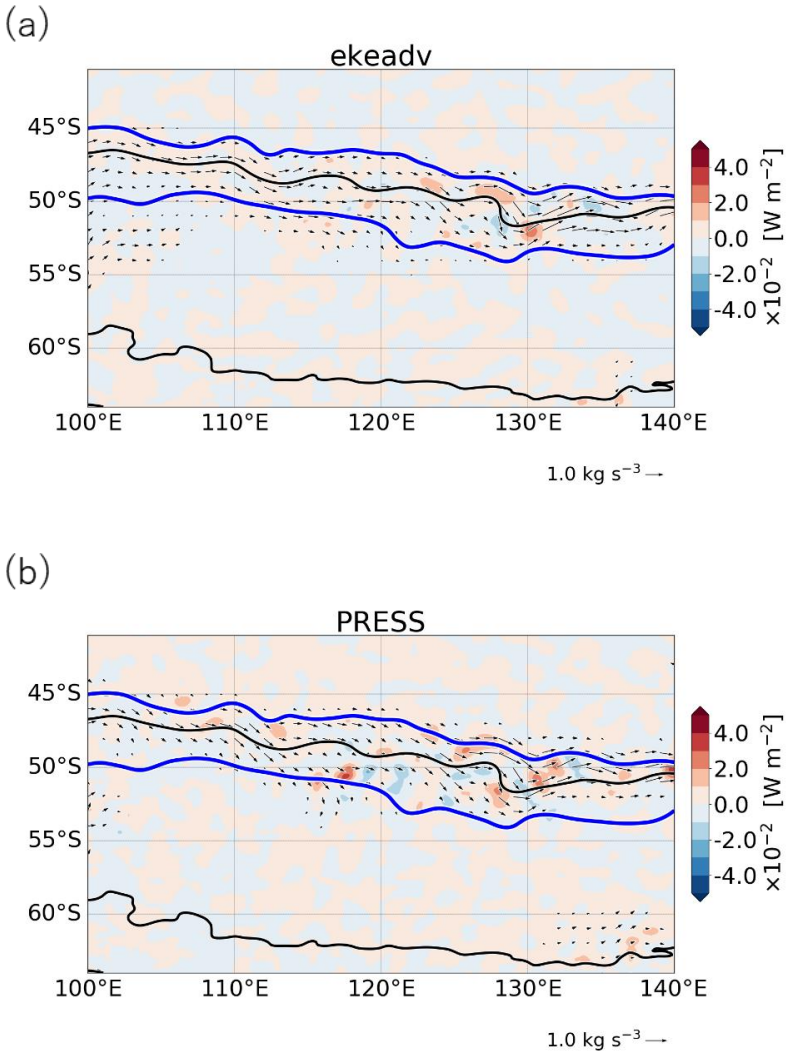

Fig. 4-12. Horizontal distributions of the divergence of (a) the EKE advection and (b) the pressure flux integrated through the water column. Black arrows indicate the eddy advection flux vectors and eddy ageostrophic pressure flux vectors integrated through the water column, respectively. Vectors smaller than $0.2\,\mathrm{kg\,s^{-3}}$ are masked. The 0cm and -70cm sea surface height are indicated by the blue contours as the northern and southern boundary of the SAF region.

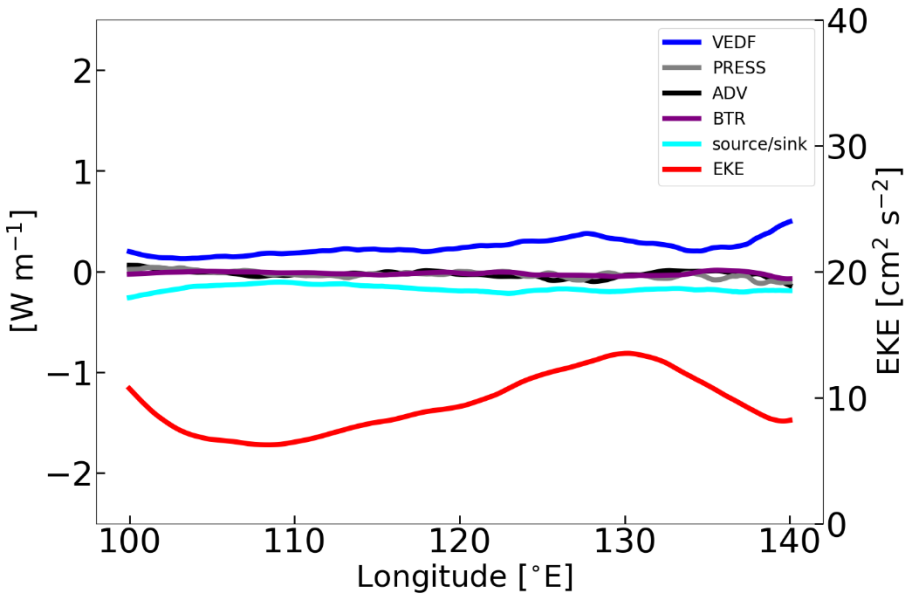

Fig. 4-13. Same as Fig. 4-7 but calculated within the SAF region indicated in Fig. 4-12.

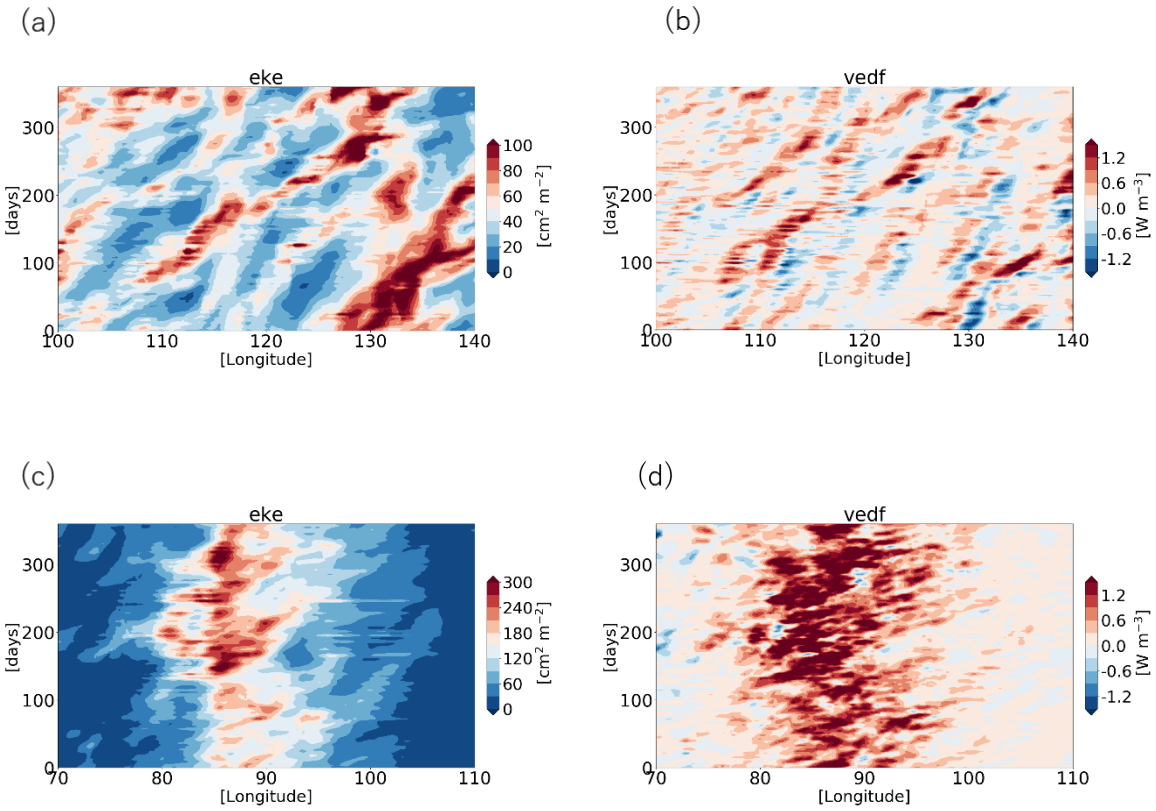

Fig. 4-14. Hovmöller diagram of (a) the EKE and (b) the VEDF in the longitude band between 100˚E and 140˚E. Values of the EKE (VEDF) is averaged (integrated) vertically and meridionally in the envelope of the SAF region. (c) and (d) are same as (a) and (b), respectively but for the envelope of the ACC region at around Region 2.

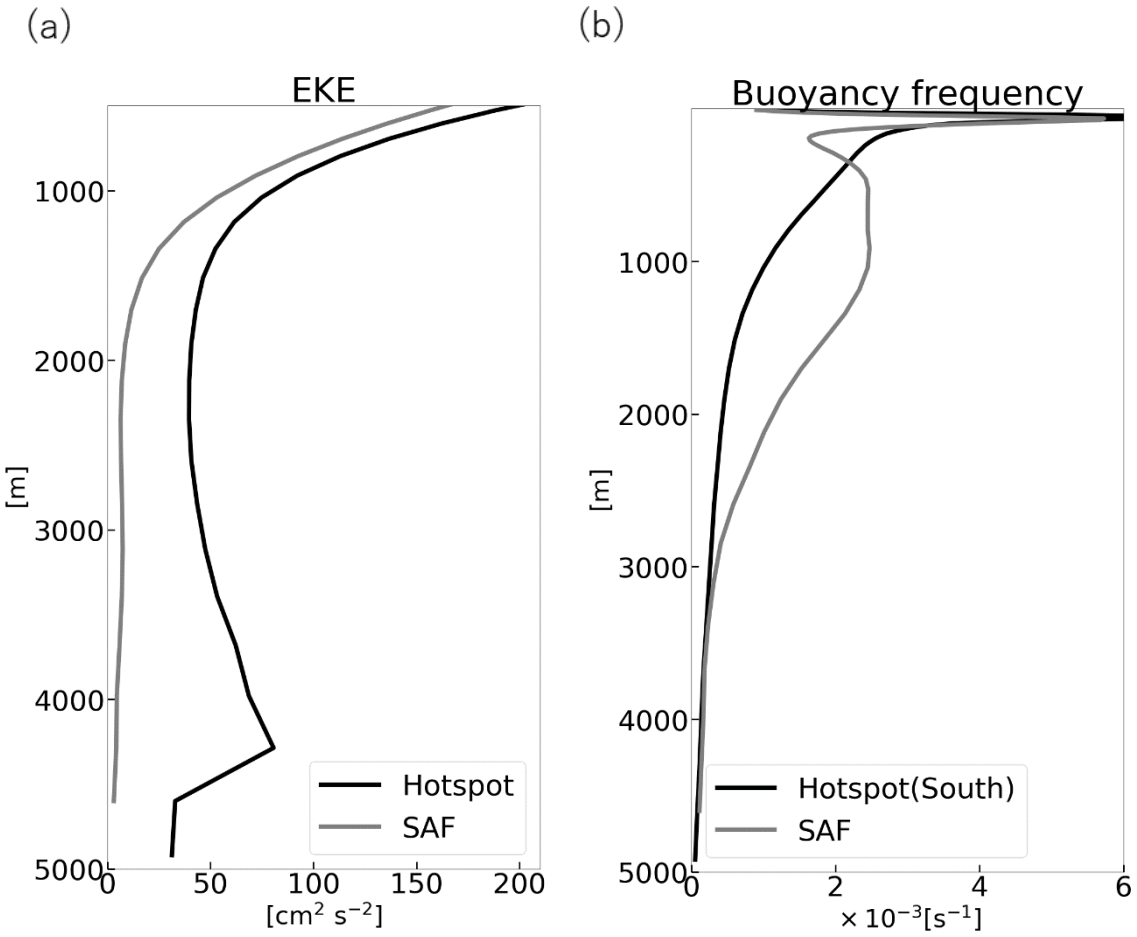

Fig. 4-15. (a) Vertical profiles of the EKE averaged horizontally in the hotspot, Region 2, (black line) and the SAF region (gray line). (b) Vertical profiles of buoyancy frequencies averaged horizontally in the southern part of Region 2 (a black line), and the SAF region (a gray line). The buoyancy frequency is obtained from the mean potential density referenced to the surface.

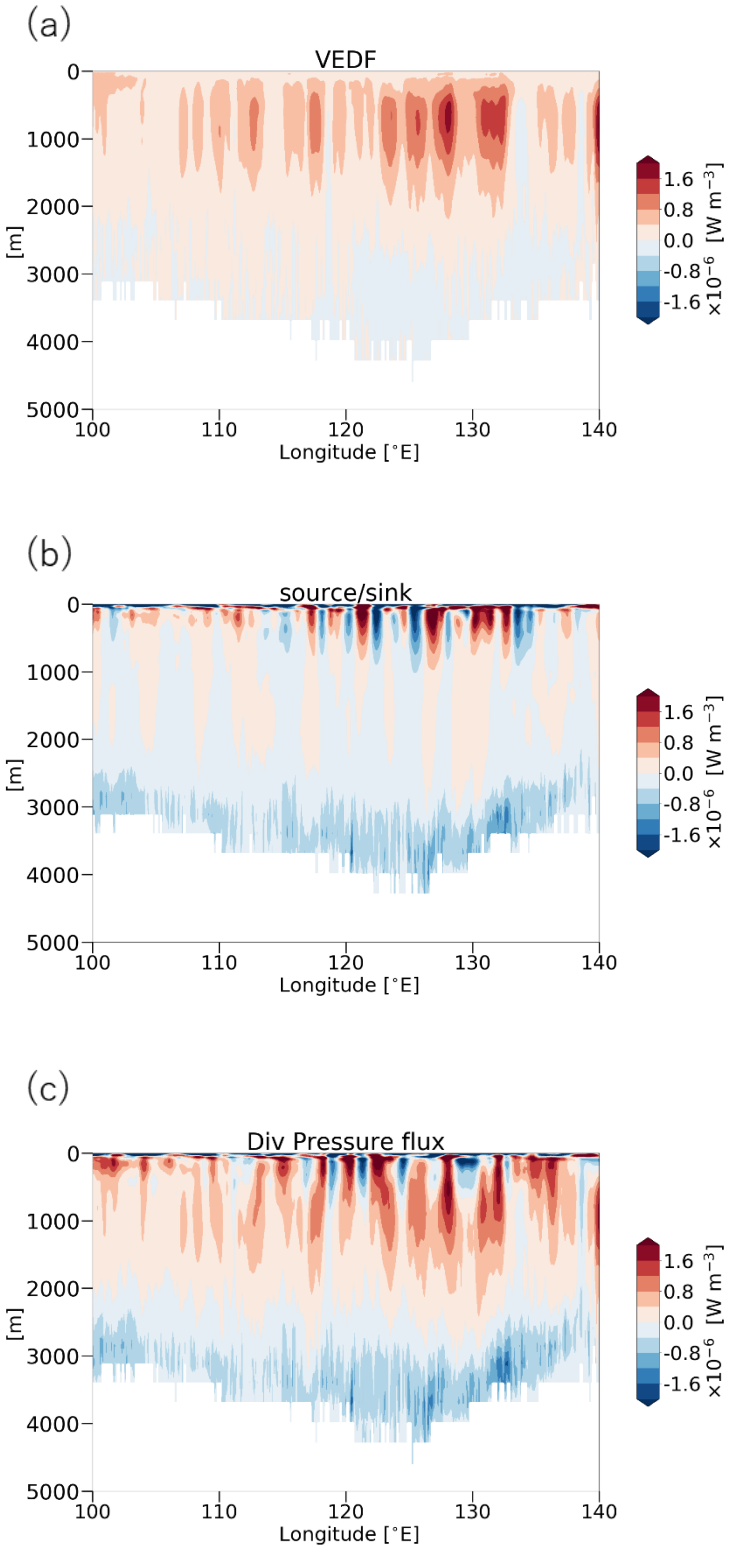

Fig. 4-16. Vertical distributions of (a) the VEDF, (b) the EKE sources/sink and (c) the divergence of pressure flux averaged meridionally in the envelope of the SAF region indicated in Fig. 4-12.

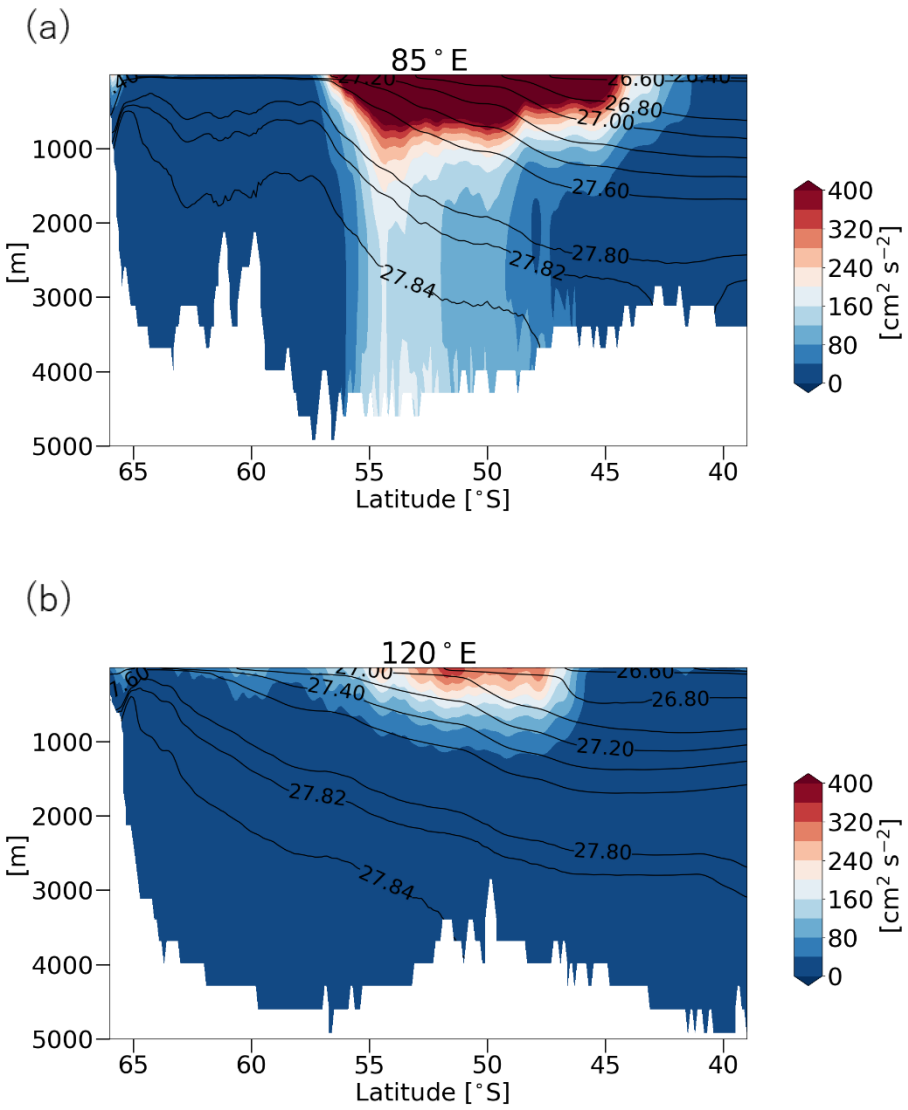

Fig. 4-17. Meridional sections of the EKE along (a) 85˚E and (b) 120˚E. Black contours represent the potential density referenced to the surface at the same section.

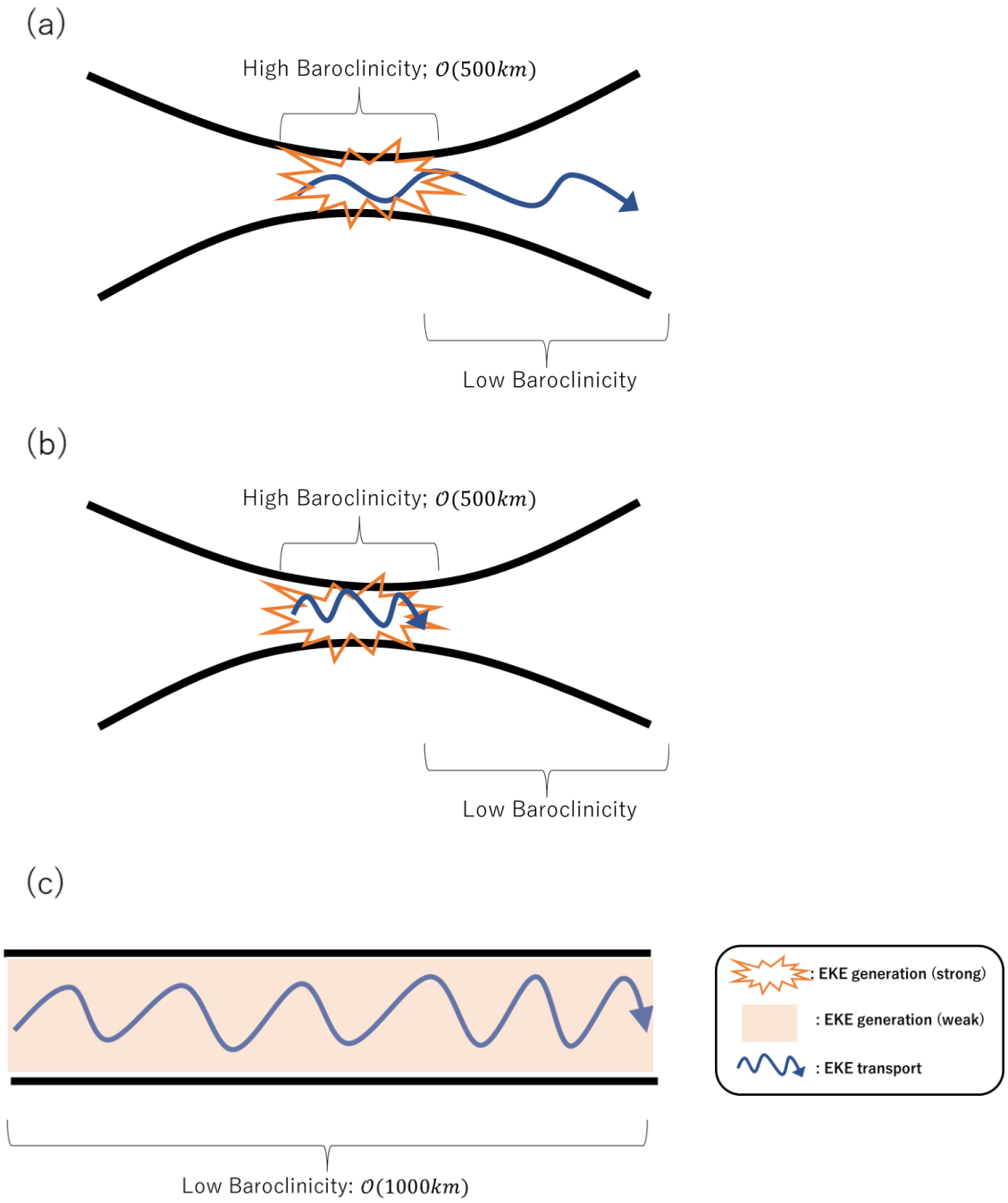

Fig. 4-18. Schematics summarizing the initiation and termination of storm tracks in the idealized ACC, the hotspots and the EKE band along the SAF. (a) The initiation of storm tracks in the idealized ACC is governed by the high baroclinicity associated with the upgradient heat flux due to the standing meander. Relatively large values of the EKE are sustained downstream of the eddy growth regime (the region of the low baroclinicity in (a))

by the horizontal pressure flux, which is an analogy of the downstream development of atmospheric storm tracks over the ocean. (b) The initiation and termination of the hotspots is simply governed by the baroclinicity of the standing meander. Unlike the storm tracks in idealized ACC, the EKE generated by the baroclinic instability is dissipated locally through the vertical redistribution of EKE shown in Fig. 4-11. The remaining part of the EKE is radiated from the upstream side in the hotspots by the advection and pressure fluxes, which converge in the downstream side in the hotspots. The converged EKE in the downstream side is also transported towards the bottom by the pressure flux, resulting in the EKE sink. This results in the downstream decay of the hotspots in OFES. (c) The eddy activities along the SAF are self-maintained as atmospheric storm tracks. Although the SAF is the region of low baroclinicity, the transports due to the pressure flux and advection sustain eddy activities along the SAF.

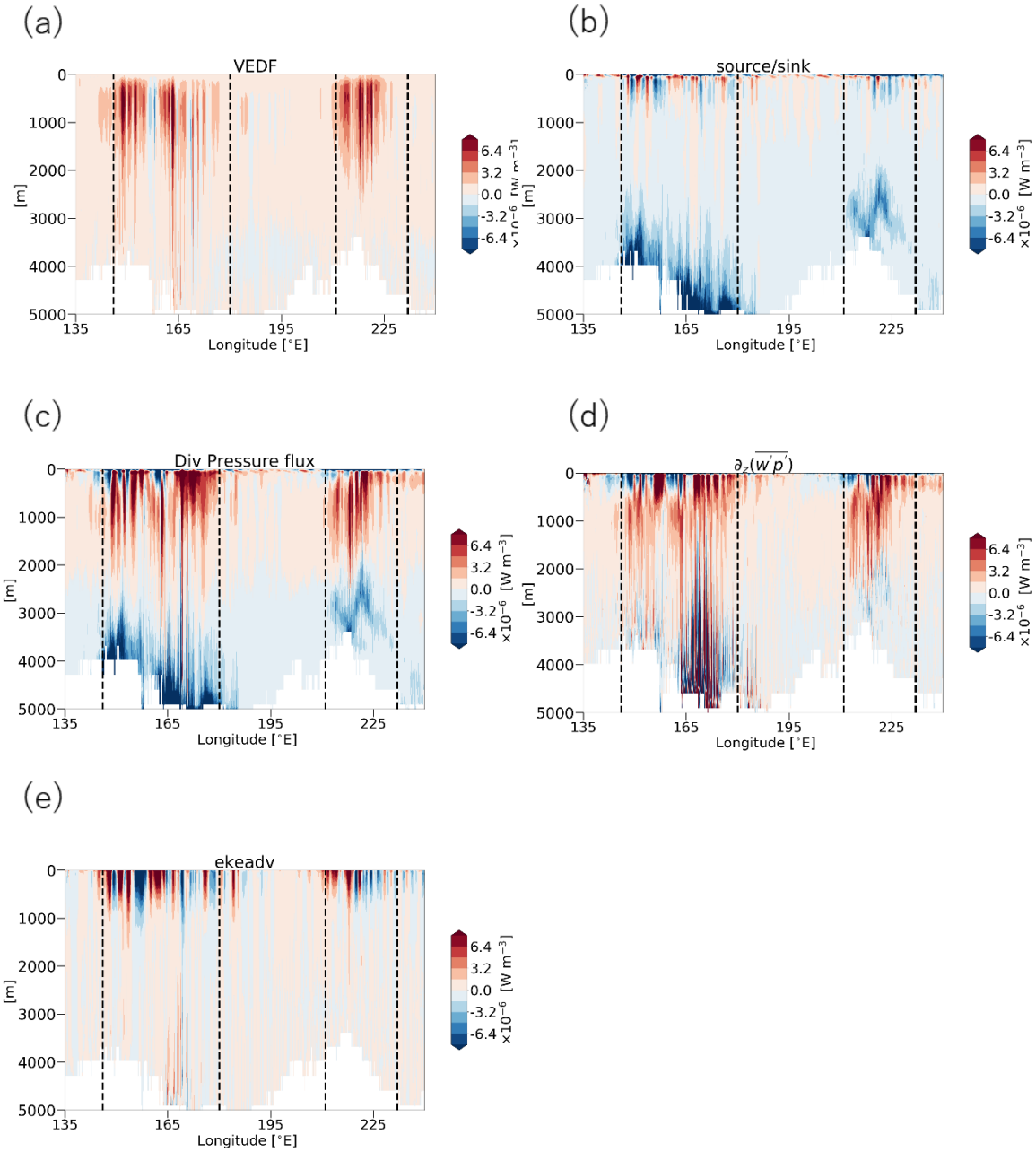

Fig 4A-1. Same as Fig. 4-10 but for the Pacific sector. Vertical black dotted lines at 146˚E, 180˚E, 211˚E, and 232˚E indicate the western and eastern boundary of Region 3 and Region 4, respectively.

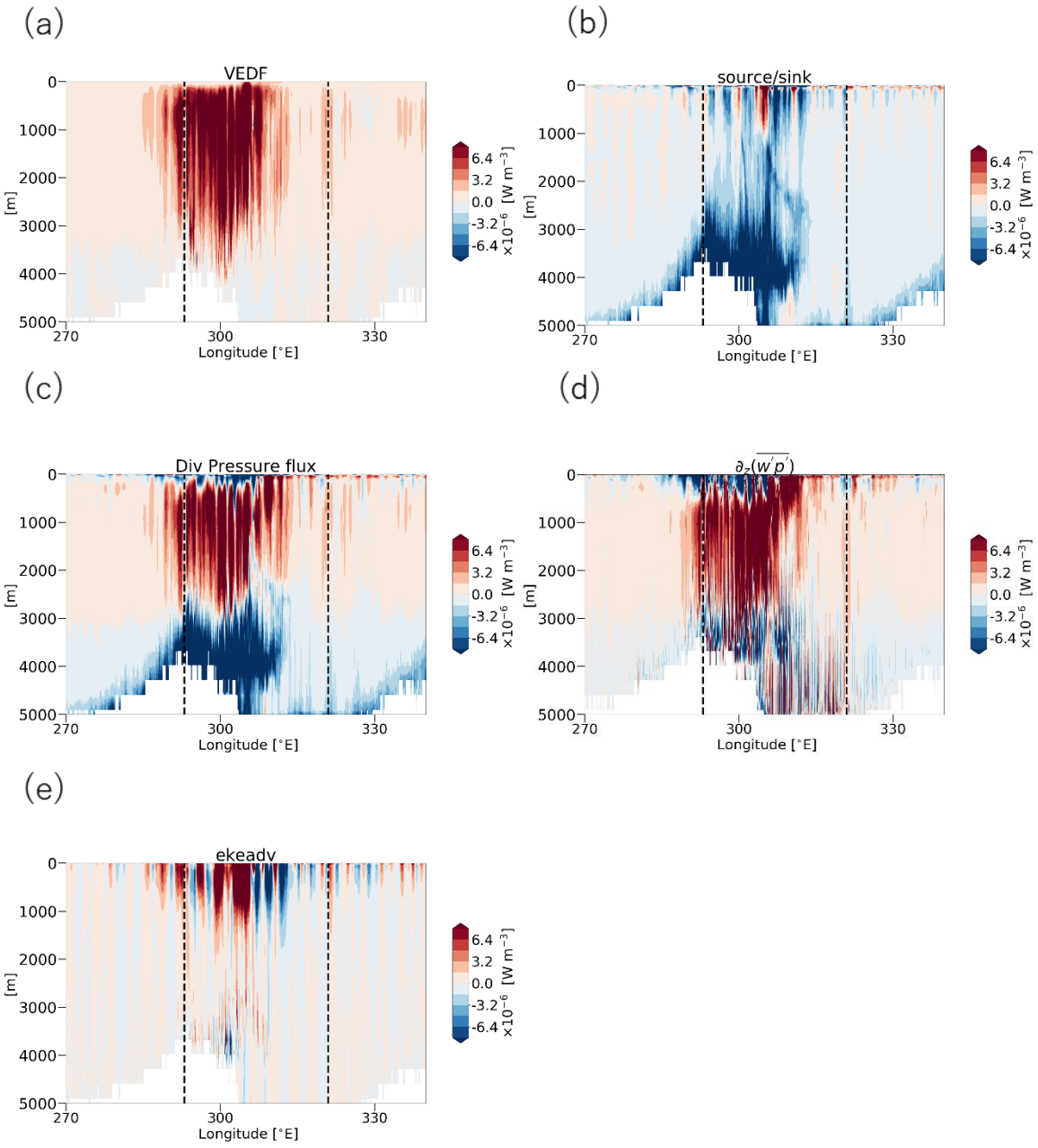

Fig 4A-2. Same as Fig. 4-10 but for the Atlantic sector. The vertical black dotted lines at 293˚E, and 321˚E indicate the western and eastern boundary of Region 5.

Chapter 5. General conclusions and implications

5.1 Summary of this thesis

The Antarctic Circumpolar Current (ACC) region is believed to play a key role in the global ocean circulation that affects the Earth's climate and material circulations. For better understanding of these circulations in the ACC region, detailed knowledges on the ACC dynamics are imperative.

Previous studies have shown that the ACC is insensitive to the changes in the westerlies. While the westerlies has been intensified and shifted southward since the twentieth century (e.g. Marshall 2003), several observational evidences indicate that the isopycnal slope associated with the ACC is insensitive to such changes in the winds (e.g. Böning et al. 2008). Idealized channel models have shown that this unique aspect of the ACC is attributed to the eddy-mean flow interactions. When inclination of the isopycnal surfaces increases, eddy perturbations are generated through baroclinic instability and work to flatten density gradients. This results in the insensitivity of the time-averaged isopycnal tilting to changes in wind forcing, known as the eddy saturation and the eddy compensation (e.g. Marshall and Radko 2003; Hogg et al. 2008; Abernathey et al. 2011; Stewart and Thompson 2013; Munday et al. 2013; Nadeau and Ferrari 2015; Chapman et al. 2015; Youngs et al. 2017, 2019). However, eddy activities reproduced in such models are unrealistic and/or insufficient, particularly in the following two aspects. First, many of the idealized models assumes zonally homogeneous conditions, but the observed eddy activities are strongly non-uniform in space (Fig. 1-1). Second, although some studies utilize models that can represent localized eddy activities, they fail to capture the zonal length scale of the large eddy activity regions, called hotspots. Eddy activities extend further downstream of the ACC from their generation sites in the idealized models (Bischoff and Thompson 2014; Chapman et al. 2015), which is contradictory to observations with rather limited zonal width (Fig. 1-1) .The spatial heterogeneity of the eddy activities in the ACC has not been investigated quantitatively, and detailed mechanisms determining the zonal length

scale of the hotspots has not revealed yet. In-depth clarification of eddy-mean flow interactions in a realistic eddy-resolving ocean general circulation model (OGCM) is thus necessary and results obtained may contribute to further understanding of the eddy saturation and the eddy compensation of the ACC in the realistic ocean.

We have, therefore, investigated such issues based on outputs from an eddy-resolving OGCM, called as OFES, in this thesis. OFES reproduces well the spatially inhomogeneous distributions of eddy activities and a length scale of the hotspots in the ACC, thus providing a good platform to analyze eddy-mean flow interactions of the realistic Southern Ocean. In Chapter 3, the eddy-mean flow interactions are estimated quantitatively based on the Lorenz energy cycle. Since it is confirmed that the classical Lorenz energy cycle includes non-negligible errors in the ACC region due to insufficiency in the linear approximation for the density fluctuations, we utilized the modified energy cycle proposed by Zemskova et al. (2015). Based on the modified diagram, it is confirmed that more than 70% of the total baroclinic energy conversion rate and the eddy kinetic energy (EKE) sink over the ACC region are contributed from the five major hotspots. Regional energy analyses show that the baroclinic instability is dominant among all the five hotspots, whereas the barotropic instability is negligible except for the region around the Campbell Plateau. It is also confirmed that the main source of the baroclinic instability is the wind energy imparted on the geostrophic current. The wind energy input is sufficient to initiate the baroclinic instability in the hotspots except for Region 5 near the Drake Passage, where additional non-local sources are required.

In Chapter 4, the initiation and termination mechanisms of the hotspots are discussed based on the heat budget analysis and the EKE budget analysis. The heat budget for the hotspots shows that the heat flux caused by the transient eddies counterbalances the heat flux due to the standing eddies. The heat flux due to the standing eddies converges (diverges) in the northern

(southern) part of the ACC, resulting in the enhancement of the meridional density gradient, which forms a favorable condition for the baroclinic instability. Since the heat flux divergence or convergence due to the standing eddies has the deep structure in vertical, the transient eddy heat flux divergence or convergence also shows large values over the depth shallower than a depth of 4000 m. To reveal mechanisms responsible for the initiation and termination mechanisms of the hotspots, we analyze each component of the EKE equation. The OFES results demonstrate that a large part of the EKE, generated through the baroclinic energy conversion, is balanced by the diabatic dissipation at their generation sites. The remaining part of the EKE is radiated from the upstream side in the hotspots by the advection and pressure fluxes, which converge in the downstream side in the hotspots. The eddy signals cannot go beyond the eastern boundary of the hotspots of rather limited width, which can be considered as the "downstream decay" of the eddy activities. Although the pressure flux plays a secondary role compared to the advection in the horizontal transport, it plays a central role in the local EKE sink. The vertical pressure flux transports the EKE from the upper layer above the main thermocline towards the ocean bottom. The EKE converged near the bottom is dissipated due to the diabatic process, indicating that the vertical redistribution of the EKE is the key process for the "downstream decay" of the hotspots. These results show large contrast to the previous studies based on idealized models for the ACC (e.g. Chapman et al. 2015), which suggest that the EKE radiation through the pressure flux sustains the relatively large EKE even in further downstream of the eddy growth region, often referred to as the downstream development.

Unlike the eddies in the hotspots, the EKE band along the Subantarctic Front (SAF) rarely decay in spite of weak baroclinicity. In other words, the SAF is in the downstream development regime similar to the idealized channel models. This difference between the hotspots and the SAF region emphasizes an importance of the vertical communication in the eddy activities. While the large vertical EKE transport in the hotspots forms eddies with deep structure that

reaches the bottom, where most of the eddy energy is dissipated, this vertical communication is rather small in the SAF region, where the surface intensified eddies dominated. The strong vertical stratification in the SAF region may be responsible for this weak vertical communication.

The idealized channel models used in the previous studies (Bischoff and Thompson 2014; Chapman et al. 2015) have no effect of bottom topographies to dissipate the EKE efficiently. This prevents the vertical communication in the eddy activities, which leads to the unrealistic downstream development in the idealized models. The topographic roughness also can explain the difference between the hotspots in the ACC and the atmospheric storm track. Since the major atmospheric storm tracks develop over the ocean, the eddy-topography interactions are almost absent over rather smooth sea surface, allowing the atmospheric storm track to have the downstream development. These conditions are different from the OFES results showing the downstream decay. Therefore, this thesis concludes that the upgradient heat flux associated with the standing meanders directly controls the initiation and termination of the hotspots, due to the vertical redistribution of the eddy energy, and determines the zonal width of the hotspots as well as the extent of eddy-mean flow interactions within the hotspots, hence most of the eddy-mean flow interactions of the whole ACC region.

Before closing this section, it is noted that the results presented in this thesis is based on the hindcast run forced by the NCEP/NCAR reanalysis, and therefore contains some uncertainties. For example, the bulk formula for the momentum flux utilizes just the wind speeds, not the relative wind speeds to the ocean surface velocities, which overestimate the wind energy input. While the wind energy input on the geostrophic flow (the Eq. (3.28)) integrated inside the ACC region is 333 GW in SOSE (Roquet et al. 2011), it reaches 425 GW in OFES (Table 3-2). Another example is that 6 hours mean wind forcing underestimates the

energy input to inertial motions, which is non-negligible contributions to the global energy balance (Watanabe and Hibiya 2002). Biases included in the NCEP/NCAR reanalysis itself also lead to uncertainties in our simulation. More realistic estimation of the energy balance is left for future works.

5.2. Implications for eddy saturation/compensation and future works

In Chapter 3, it is revealed that the five major hotspots are responsible for the time-averaged eddy-mean flow interactions over the ACC region. In recently proposed concept of "intermittent ACC" (Thompson and Garabato 2014), the hotspots are central to the adjustment process. In order to investigate responses of the hotspots to changes in the wind forcing, we compare magnitude of the vertical eddy density flux (VEDF) and the EKE between the two representative periods of anomalous conditions; one for the period from 1997 to 2002 with the anomalously large positive Southern Annular Mode (SAM) index and another for the period from 1991 to 1996 with the anomalously large negative SAM index (Fig. 2-1). The SAM index is defined here as the zonal pressure difference between the latitudes of 40˚S and 65S. (see the Eq. (2.1)). Figure 5-1 shows zonal distributions of the VEDF and EKE integrated meridionally and vertically in the ACC region for Region 2, as an example. According to Fig. 5-1, the EKE increases 30% at most during the positive SAM period, and the VEDF difference between the positive and negative SAM periods reaches about $1.0\ \mathrm{W\ m^{-1}}$ near the center of the hotspot. On the other hand, the eddy activities, both the EKE and VEDF, show little changes between the two periods in the free zone. These results suggest that the significant responses in the eddy activities to the change in the wind forcing occur only in the region inside the hotspots. Table 5-1 summarizes the VEDF changes in all the five hotspots as well as the entire ACC region. The VEDF increases by 10% over the ACC region during the positive SAM period, and 75%

of which results from the hotspots. Therefore, it is suggested that the eddy activities in these hotspots keep the zonal transport almost constant during the analysis period (see Fig. 2-1). It is also noted that the vertical redistribution of the EKE is sufficient to relax the changes associated with the wind forcing as long as the changes in the wind forcing stay in the realistic range.

In addition to the above implication for responses of the hotspots, our results suggest that representations of the vertical viscosity and bottom topography should be improved both in theoretical considerations and in numerical models. Particularly for numerical models, as shown in Chapter 4, the eddy energy sink is eventually related to the EKE dissipation due to the sub-grid scale processes. This strongly suggests that the ACC transport in the equilibrium state is controlled by the viscosity and bottom topography. The smaller zonal mean transport simulated in many OGCMs, including OFES, discussed in Chapter 2 may result from inappropriate expressions of the viscosity and bottom topography in the models. Although OFES represents vertical viscosity based on the KPP scheme, the generation of lee waves is one of the most possible mechanisms for enhanced dissipation in the real world. If this is the case, the zonal transport will be close to the realistic values with more realistic representation of viscosity and bottom topographies. Since the implementation of the gravity wave drag into an OGCM reduces the simulated eddy activities (Trossman et al., 2016), the parametrizations of the vertical mixing processes is likely to be critical to determine the equilibrium state of the ACC.

The observational studies indicate that the water mass properties and formation rate of the Antarctic Bottom Water are modified by climate anomalies (e.g. Menezes et al. 2017; Silvano et al. 2020). Moreover, a model study by Lago and England (2019) predicts that the present-day abyssal water masses may be changed under the global warming trend. These possibility of the deep water modifications would alter the dissipation rate of the EKE, through changes

in mixing processes near the bottom in the ACC region, which is critical to the eddy saturation and eddy compensation of the ACC. These changes in the bottom water under the global warming stress and their links to the eddy lifecycle, therefore, should be investigated in the future works.

Table 5-1. Area-integrated values of the VEDF in each hotspot for the period of the negative (1991-1996) and positive (1997-2002) SAM, respectively. The values integrated over the five hotspots (*Sum*) and the entire ACC region (*ACC*) are also shown.

[GW]	Negative	Positive
Region 1	19	20
Region 2	41	48
Region 3	19	26
Region 4	18	17
Region 5	48	50
Sum	145	161
ACC	200	221

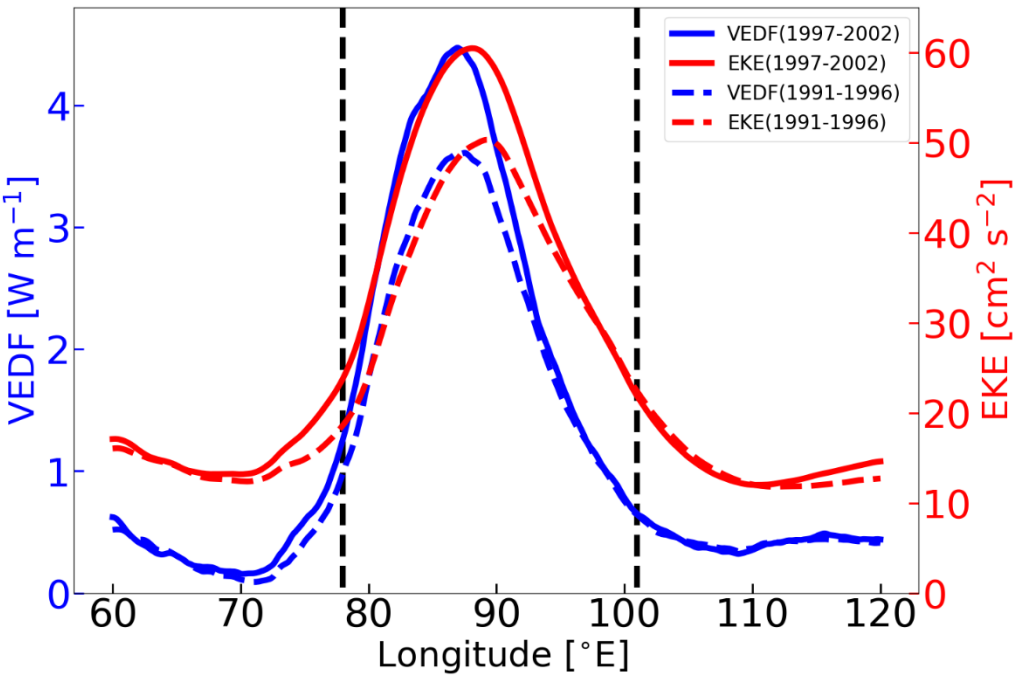

Fig. 5-1. Zonal distributions of the VEDF (EKE) integrated (averaged) meridionally and vertically within the ACC are shown in blue (red) lines. The solid and dashed lines indicate the values for the period of the positive SAM (1997-2002) and the negative SAM (1991-1996), respectively. The vertical dashed black lines indicate the western and eastern boundaries of the hotspots in Region 2.

Acknowledgments

Firstly, I would like to thank to my advisor Yukio Masumoto for his sincere support of my Ph.D. studies. His encouragement enabled me to return to the academic research and start my Ph. D. course. I have learned many methods and personality as a scientist. I became enthusiastic about the physical oceanography and climate dynamics through discussions with him. I am really honored to be his student.

I also greatly appreciate the referees of this thesis, Tomoki Tozuka, Ichiro Yasuda, Keita Iga, and Katsuro Katsumata for their time and helpful comments. The author thanks to Atsushi Kubokawa, Humio Mitsudera, Hidenori Aiki and Shigeru Aoki for their critical comments for my study. This study has been improved through discussion with Bo Qiu, Eitaro Oka, Eric Firing, Hiroaki Miura, Hiroyasu Hasumi, Hisashi Nakamura, Julian McCreary, Jr., Kaihe Yamazaki, Kay I. Ohshima, Kelvin Richards, Kunihiro Aoki, Masahiro Watanabe, Masashi Kohma, Norihiko Sugimoto, Shang-Ping Xie, Takashi Ijichi, Toshio Suga, Tomomichi Ogata, Toshiyuki Hibiya, Yu Kosaka, and Yuki Tanaka. I also appreciate all past and presents members of Atmospheric and Oceanic Science Group and faculty members of Department of Earth and Planetary Science. I especially give a special thanks to all students of our research group, Takahiro Kusumi, Yusuke Terada, and Natsuki Yasuda for beneficial discussions at weekly meetings. I cannot forget many supports and encouragement by Shu Nakamura and Toru Koma during my master-course at Graduate School of Mathematical Sciences, The University of Tokyo. They helped me solidifying the foundation as a scientist. I also thank to all students and staffs at Graduate School of Mathematical Sciences, The University of Tokyo. I learned many scientific topics from them through everyday coffee break. I appreciate my friend, Yuichi Harikane. We have enjoyed scientific discussions since a general education course, and I have learned a lot from him.

It is acknowledged that a part of this research was supported by Fostering Advanced Human Resources to Lead GreenaTransformation (GX) program for Support for Pioneering Research Initiated by Next Generation (SPRING) of Japan Science and Technology Agency.

Finally, I greatly thank my family to support me throughout my life. I could not complete this thesis without their supports.

References

Abernathey, R., and P. Cessi, 2014: Topographic enhancement of Eddy efficiency in baroclinic equilibration. *J. Phys. Oceanogr.*, **44**, 2107–2126, https://doi.org/10.1175/JPO-D-14-0014.1.

——, J. Marshall, and D. Ferreira, 2011: The dependence of southern ocean meridional overturning on wind stress. *J. Phys. Oceanogr.*, **41**, 2261–2278, https://doi.org/10.1175/JPO-D-11-023.1.

Aiki, H., and K. J. Richards, 2008: Energetics of the global ocean: The role of layer-thickness form drag. *J. Phys. Oceanogr.*, **38**, 1845–1869, https://doi.org/10.1175/2008JPO3820.1.

——, ——, and H. Sakuma, 2011: Maintenance of the mean kinetic energy in the global ocean by the barotropic and baroclinic energy routes: The roles of JEBAR and Ekman dynamics. *Ocean Dyn.*, **61**, 675–700, https://doi.org/10.1007/s10236-011-0382-y.

——, X. Zhai, and R. J. Greatbatch, 2016: Energetics of the global ocean: The role of mesoscale eddies. *World Sci. Ser. Asia-Pacific Weather Clim.*, **7**, 109–134, https://doi.org/10.1142/9789814696623_0004.

Barthel, A., A. McC. Hogg, S. Waterman, and S. Keating, 2017: Jet-topography interactions affect energy pathways to the deep Southern Ocean. *J. Phys. Oceanogr.*, **47**, 1799–1816, https://doi.org/10.1175/JPO-D-16-0220.1.

Bischoff, T., and A. F. Thompson, 2014: Configuration of a Southern Ocean storm track. *J. Phys. Oceanogr.*, **44**, 3072–3078, https://doi.org/10.1175/JPO-D-14-0062.1.

Bishop, S. P., P. R. Gent, F. O. Bryan, A. F. Thompson, M. C. Long, and R. Abernathey, 2016: Southern ocean overturning compensation in an eddy-resolving climate

simulation. *J. Phys. Oceanogr.*, **46**, 1575–1592, https://doi.org/10.1175/JPO-D-15-0177.1.

Böning, C. W., A. Dispert, M. Visbeck, S. R. Rintoul, and F. U. Schwarzkopf, 2008: The response of the antarctic circumpolar current to recent climate change. *Nat. Geosci.*, **1**, 864–869, https://doi.org/10.1038/ngeo362.

Boyer, T. P., S. Levitus, J.I. Antonov, M. E. Conkright, T. O'Brien, and C. Stephens, 1998a: *World Ocean Atlas 1998 Vol. 4: Salinity of the Atlantic Ocean. NOAA Atlas NESDIS 30*. U.S. Government Printing Office,.

——, ——, ——, ——, ——, and ——, 1998b: *World Ocean Atlas 1998 Vol. 5: Salinity of the Pacific Ocean. NOAA Atlas NESDIS 31*. U.S. Government Printing Office,.

——, ——, ——, ——, ——, ——, and B. Trotsenko, 1998c: *World Ocean Atlas 1998 Vol. 6: Salinity of the Indian Ocean. NOAA Atlas NESDIS 32*. U.S. Government Printing Office,.

Chang, E. K. M., 1993: Downstream Development of Baroclinic Waves As Inferred from Regression Analysis. *J. Atmos. Sci.*, **50**, 2038–2053, https://doi.org/10.1175/1520-0469(1993)050<2038:DDOBWA>2.0.CO;2.

——, and I. Orlanski, 1993: On the Dynamics of a Storm Track. *J. Atmos. Sci.*, **50**, 999–1015, https://doi.org/10.1175/1520-0469(1993)050<0999:OTDOAS>2.0.CO;2.

Chang, E. K. M., S. Lee, and K. L. Swanson, 2002: Storm track dynamics. *J. Clim.*, **15**, 2163–2183, https://doi.org/10.1175/1520-0442(2002)015<02163:STD>2.0.CO;2.

Chapman, C. C., A. M. C. Hogg, A. E. Kiss, and S. R. Rintoul, 2015: The dynamics of Southern Ocean storm tracks. *J. Phys. Oceanogr.*, **45**, 884–903, https://doi.org/10.1175/JPO-D-14-0075.1.

Chemke, R., and Y. Kaspi, 2016: The latitudinal dependence of the oceanic barotropic eddy kinetic energy and macroturbulence energy transport. *Geophys. Res. Lett.*, **43**, 2723–2731, https://doi.org/10.1002/2016GL067847.

Chen, R., G. R. Flierl, and C. Wunsch, 2014: A description of local and nonlocal eddy-mean flow interaction in a global eddy-permitting state estimate. *J. Phys. Oceanogr.*, **44**, 2336–2352, https://doi.org/10.1175/JPO-D-14-0009.1.

——, A. F. Thompson, and G. R. Flierl, 2016: Time-dependent eddy-mean energy diagrams and their application to the ocean. *J. Phys. Oceanogr.*, **46**, 2827–2850, https://doi.org/10.1175/JPO-D-16-0012.1.

Chidichimo, M. P., K. A. Donohue, D. R. Watts, and K. L. Tracey, 2014: Baroclinic transport time series of the Antarctic Circumpolar Current measured in Drake Passage. *J. Phys. Oceanogr.*, **44**, 1829–1853, https://doi.org/10.1175/JPO-D-13-071.1.

Danielson, R. E., J. R. Gyakum, and D. N. Straub, 2006: A case study of downstream baroclinic development over the North Pacific Ocean. Part I: Dynamical impacts. *Mon. Weather Rev.*, **134**, 1534–1548, https://doi.org/10.1175/MWR3172.1.

Donohue, K. A., K. L. Tracey, D. R. Watts, M. P. Chidichimo, and T. K. Chereskin, 2016: Mean Antarctic Circumpolar Current transport measured in Drake Passage. *Geophys. Res. Lett.*, **43**, 11,760-11,767, https://doi.org/10.1002/2016GL070319.

Döös, K., and D. J. Webb, 1994: The Deacon Cell and the Other Meridional Cells of the Southern Ocean. *J. Phys. Oceanogr.*, **24**, 429–442, https://doi.org/10.1175/1520-0485(1994)024<0429:TDCATO>2.0.CO;2.

Ducet, N., P. Y. Le Traon, and G. Reverdin, 2000: Global high-resolution mapping of ocean circulation from TOPEX/Poseidon and ERS-1 and -2. *J. Geophys. Res. Ocean.*, **105**, 19477–19498, https://doi.org/10.1029/2000jc900063.

Firing, Y. L., T. K. Chereskin, and M. R. Mazloff, 2011: Vertical structure and transport of the Antarctic Circumpolar Current in Drake Passage from direct velocity observations. *J. Geophys. Res. Ocean.*, **116**, 1–16, https://doi.org/10.1029/2011JC006999.

Foppert, A., 2019: Observed storm track dynamics in Drake Passage. *J. Phys. Oceanogr.*, **49**, 867–884, https://doi.org/10.1175/JPO-D-18-0150.1.

Frenger, I., M. Münnich, N. Gruber, and R. Knutti, 2015: Southern Ocean eddy phenomenology. *J. Geophys. Res. Ocean.*, **120**, 7413–7449, https://doi.org/10.1002/2015JC011047.

Frisius, T., F. Lunkeit, K. Fraedrich, and I. N. James, 1998: Storm-track organization and variability in a simplified atmospheric global circulation model. *Q. J. R. Meteorol. Soc.*, **124**, 1019–1043, https://doi.org/10.1002/qj.49712454802.

Gong, D., and S. Wang, 1999: Definition of Antarctic oscillation index. *Geophys. Res. Lett.*, **26**, 459–462, https://doi.org/10.1029/1999GL900003.

Griffies, S. M., and Coauthors, 2015: Impacts on ocean heat from transient mesoscale eddies in a hierarchy of climate models. *J. Clim.*, **28**, 952–977, https://doi.org/10.1175/JCLI-D-14-00353.1.

Hallberg, R., 2013: Using a resolution function to regulate parameterizations of oceanic mesoscale eddy effects. *Ocean Model.*, **72**, 92–103, https://doi.org/10.1016/j.ocemod.2013.08.007.

Hogg, A. M., M. P. Meredith, D. P. Chambers, E. P. Abrahamsen, C. W. Hughes, and A. K. Morrison, 2015: Recent trends in the Southern Ocean eddy field. *J. Geophys. Res. Ocean.*, **120**, 257–267, https://doi.org/10.1002/2014JC010470.

Hogg, A. M. C., M. P. Meredith, J. R. Blundel, and C. Wilson, 2008: Eddy heat flux in the Sourthern ocean: Response to variable wind forcing. *J. Clim.*, **21**, 608–620, https://doi.org/10.1175/2007JCLI1925.1.

Hoskins, B. J., and P. J. Valdes, 1990: On the Existence of Storm-Tracks. *J. Atmos. Sci.*, **47**, 1854–1864, https://doi.org/10.1175/1520-0469(1990)047<1854:OTEOST>2.0.CO;2.

Hughes, C. W., 2005: Nonlinear vorticity balance of the Antarctic Circumpolar Current. *J. Geophys. Res. Ocean.*, **110**, 1–11, https://doi.org/10.1029/2004JC002753.

Johnson, G. C., and H. L. Bryden, 1989: On the size of the Antarctic Circumpolar Current. *Deep Sea Res. Part A. Oceanogr. Res. Pap.*, **36**, 39–53, https://doi.org/10.1016/0198-0149(89)90017-4.

Jouanno, J., and X. Capet, 2020: Connecting flow-topography interactions, vorticity balance, baroclinic instability and transport in the Southern Ocean: The case of an idealized storm track. *Ocean Sci.*, **16**, 1207–1223, https://doi.org/10.5194/os-16-1207-2020.

Jüling, A., J. P. Viebahn, S. S. Drijfhout, and H. A. Dijkstra, 2018: Energetics of the Southern Ocean Mode. *J. Geophys. Res. Ocean.*, **123**, 9283–9304, https://doi.org/10.1029/2018JC014191.

Kalnay, E., and Coauthors, 1996: The NCEP/NCAR 40-Year Reanalysis Project. *Bull. Am. Meteorol. Soc.*, **77**, 437–471, https://doi.org/10.1175/1520-0477(1996)077<0437:TNYRP>2.0.CO;2.

Karsten, R. H., and J. Marshall, 2002: Constructing the residual circulation of the ACC from observations. *J. Phys. Oceanogr.*, **32**, 3315–3327, https://doi.org/10.1175/1520-0485(2002)032<3315:CTRCOT>2.0.CO;2.

Kaspi, Y., and T. Schneider, 2013: The role of stationary eddies in shaping midlatitude storm tracks. *J. Atmos. Sci.*, **70**, 2596–2613, https://doi.org/10.1175/JAS-D-12-082.1.

Katsumata, K., 2017: Eddies observed by Argo floats. Part II: Form stress and streamline length in the Southern Ocean. *J. Phys. Oceanogr.*, **47**, 2237–2250, https://doi.org/10.1175/JPO-D-17-0072.1.

Kim, Y. S., and A. H. Orsi, 2014: On the Variability of Antarctic Circumpolar Current Fronts Inferred from 1992–2011 Altimetry*. *J. Phys. Oceanogr.*, **44**, 3054–3071, https://doi.org/10.1175/JPO-D-13-0217.1.

Lago, V., and M. H. England, 2019: Projected Slowdown of Antarctic Bottom Water Formation in Response to Amplified Meltwater Contributions. *J. Clim.*, **32**, 6319–6335, https://doi.org/10.1175/JCLI-D-18-0622.1.

Langlais, C. E., S. R. Rintoul, and J. D. Zika, 2015: Sensitivity of antarctic circumpolar current transport and eddy activity to wind patterns in the Southern Ocean. *J. Phys. Oceanogr.*, **45**, 1051–1067, https://doi.org/10.1175/JPO-D-14-0053.1.

Large, W. G., J. C. McWilliams, and S. C. Doney, 1994: Oceanic vertical mixing: A review and a model with a nonlocal boundary layer parameterization. *Rev. Geophys.*, **32**, 363–403, https://doi.org/10.1029/94RG01872.

Ledwell, J. R., L. C. St. Laurent, J. B. Girton, and J. M. Toole, 2011: Diapycnal mixing in the antarctic circumpolar current. *J. Phys. Oceanogr.*, **41**, 241–246, https://doi.org/10.1175/2010JPO4557.1.

Liang, X. S., 2016: Canonical transfer and multiscale energetics for primitive and quasigeostrophic atmospheres. *J. Atmos. Sci.*, **73**, 4439–4468, https://doi.org/10.1175/JAS-D-16-0131.1.

Lorenz, E. N., 1955: Available Potential Energy and the Maintenance of the General Circulation. *Tellus*, **7**, 157–167, https://doi.org/10.1111/j.2153-3490.1955.tb01148.x.

Marshall, D. P., M. H. P. Ambaum, J. R. Maddison, D. R. Munday, and L. Novak, 2017: Eddy saturation and frictional control of the Antarctic Circumpolar Current. *Geophys. Res. Lett.*, **44**, 286–292, https://doi.org/10.1002/2016GL071702.

Marshall, G. J., 2003: Trends in the Southern Annular Mode from observations and reanalyses. *J. Clim.*, **16**, 4134–4143, https://doi.org/10.1175/1520-0442(2003)016<4134:TITSAM>2.0.CO;2.

Marshall, J., and T. Radko, 2003: Residual-Mean Solutions for the Antarctic Circumpolar Current and Its Associated Overturning Circulation. *J. Phys. Oceanogr.*, **33**, 2341–2354, https://doi.org/10.1175/1520-0485(2003)033<2341:RSFTAC>2.0.CO;2.

——, and K. Speer, 2012: Closure of the meridional overturning circulation through Southern Ocean upwelling. *Nat. Geosci.*, **5**, 171–180, https://doi.org/10.1038/ngeo1391.

Masich, J., T. K. Chereskin, and M. R. Mazloff, 2015: Topographic form stress in the Southern Ocean State Estimate. *J. Geophys. Res. Ocean.*, **120**, 7919–7933, https://doi.org/10.1002/2015JC011143.

Mason, E., A. Pascual, P. Gaube, S. Ruiz, J. L. Pelegrí, and A. Delepoulle, 2017: Subregional characterization of mesoscale eddies across the Brazil-Malvinas Confluence. *J. Geophys. Res. Ocean.*, **122**, 3329–3357, https://doi.org/10.1002/2016JC012611.

Masumoto, Y., and Coauthors, 2004: A fifty-year eddy-resolving simulation of the world ocean: Preliminary outcomes of OFES (OGCM for the Earth Simulator). *J. Earth Simulator*, **1**, 35–56.

Matsuta, T., and Y. Masumoto, 2021: Modified View of Energy Budget Diagram and its Application to the Kuroshio extension region. *J. Phys. Oceanogr.*, https://doi.org/10.1175/JPO-D-20-0124.1.

Mazloff, M. R., P. Heimbach, and C. Wunsch, 2010: An eddy-permitting Southern Ocean state estimate. *J. Phys. Oceanogr.*, **40**, 880–899, https://doi.org/10.1175/2009JPO4236.1.

Menezes, V. V., A. M. Macdonald, and C. Schatzman, 2017: Accelerated freshening of Antarctic Bottom Water over the last decade in the Southern Indian Ocean. *Sci. Adv.*, **3**, https://doi.org/10.1126/sciadv.1601426.

Meredith, M. P., and A. M. Hogg, 2006: Circumpolar response of Southern Ocean eddy activity to a change in the Southern Annular Mode. *Geophys. Res. Lett.*, **33**, 2–5, https://doi.org/10.1029/2006GL026499.

Munday, D. R., H. L. Johnson, and D. P. Marshall, 2013: Eddy saturation of equilibrated circumpolar currents. *J. Phys. Oceanogr.*, **43**, 507–532, https://doi.org/10.1175/JPO-D-12-095.1.

Munk, W. H., and E. Palmén, 1951: Note on the Dynamics of the Antarctic Circumpolar Current. *Tellus*, **3**, 53–55, https://doi.org/10.3402/tellusa.v3i1.8609.

Nadeau, L. P., and R. Ferrari, 2015: The role of closed gyres in setting the zonal transport of the antarctic circumpolar current. *J. Phys. Oceanogr.*, **45**, 1491–1509, https://doi.org/10.1175/JPO-D-14-0173.1.

Nakamura, N., 1993: Momentum flux, flow symmetry, and the nonlinear barotropic governor. *J. Atmos. Sci.*, **50**, 2159–2179, https://doi.org/10.1175/1520-0469(1993)050<2159:MFFSAT>2.0.CO;2.

Naveira Garabato, A. C., R. Ferrari, and K. L. Polzin, 2011: Eddy stirring in the Southern Ocean. *J. Geophys. Res. Ocean.*, **116**, 1–29, https://doi.org/10.1029/2010JC006818.

Nikurashin, M., G. K. Vallis, and A. Adcroft, 2013: Routes to energy dissipation for geostrophic flows in the Southern Ocean. *Nat. Geosci.*, **6**, 48–51, https://doi.org/10.1038/ngeo1657.

Olbers, D., J. Willebrand, and C. Eden, 2012: *Ocean Dynamics*. Springer Berlin Heidelberg,.

Orlanski, I., 1998: Poleward deflection of storm tracks. *J. Atmos. Sci.*, **55**, 2577–2602, https://doi.org/10.1175/1520-0469(1998)055<2577:PDOST>2.0.CO;2.

Orlanski, I., and J. Sheldon, 1993: A case of downstream baroclinic development over western North America. *Mon. Weather Rev.*, **121**, 2929–2950, https://doi.org/10.1175/1520-0493(1993)121<2929:ACODBD>2.0.CO;2.

Orsi, H., T. Whitworth, and W. D. N. Jr, 1995: On the meridional extent and fronts of the Antarctic Circumpolar Current Pronounced meridional gradients in surface properties separate waters of the Southern Ocean from the warmer and saltier waters of the subtropical circulations . Deacon (1933 , the S. **42**.

Pacanowski, R. C., and A. Gnanadesikan, 1998: Transient response in a Z-level ocean model that resolves topography with partial cells. *Mon. Weather Rev.*, **126**, 3248–3270, https://doi.org/10.1175/1520-0493(1998)126<3248:TRIAZL>2.0.CO;2.

Pacanowski, R. C., and S. M. Griffies, 2000: MOM 3.0 Manual. *Geophys. Fluid Dyn. Lab., Natl. Atmos. Admin., Princet.*, 682.

Phillips, H. E., and S. R. Rintoul, 2000: Eddy variability and energetics from direct current measurements in the Antarctic Circumpolar Current south of Australia. *J. Phys. Oceanogr.*, **30**, 3050–3076, https://doi.org/10.1175/1520-0485(2000)030<3050:EVAEFD>2.0.CO;2.

Piola, A. R., and R. P. Matano, 2001: Brazil And Falklands (malvinas) Currents. *Encycl. Ocean Sci.*, 340–349, https://doi.org/10.1006/rwos.2001.0358.

Plumb, R. A., 1986: Three-dimensional propagation of transient quasi-geostrophic eddies and its relationship with the eddy forcing of the time-mean flow. *J. Atmos. Sci.*, **43**, 1657–1678, https://doi.org/10.1175/1520-0469(1986)043<1657:TDPOTQ>2.0.CO;2.

Le Quéré, C., and Coauthors, 2009: Trends in the sources and sinks of carbon dioxide. *Nat. Geosci.*, **2**, 831–836, https://doi.org/10.1038/ngeo689.

Rignot, E., S. Jacobs, J. Mouginot, and B. Scheuchl, 2013: Ice-shelf melting around antarctica. *Science (80-.).*, **341**, 266–270, https://doi.org/10.1126/science.1235798.

Rintoul, S. R., 2018: The global influence of localized dynamics in the Southern Ocean. *Nature*, **558**, 209–218, https://doi.org/10.1038/s41586-018-0182-3.

Roach, C. J., H. E. Phillips, N. L. Bindoff, and S. R. Rintoul, 2015: Detecting and characterizing Ekman currents in the Southern Ocean. *J. Phys. Oceanogr.*, **45**, 1205–1223, https://doi.org/10.1175/JPO-D-14-0115.1.

Roquet, F., C. Wunsch, and G. Madec, 2011: On the patterns of wind-power input to the ocean circulation. *J. Phys. Oceanogr.*, **41**, 2328–2342, https://doi.org/10.1175/JPO-D-11-024.1.

Rosati, A., and K. Miyakoda, 1988: A General Circulation Model for Upper Ocean Simulation. *J. Phys. Oceanogr.*, **18**, 1601–1626, https://doi.org/10.1175/1520-0485(1988)018<1601:AGCMFU>2.0.CO;2.

Sallée, J. B., K. Speer, S. Rintoul, and S. Wijffels, 2010: Southern ocean thermocline ventilation. *J. Phys. Oceanogr.*, **40**, 509–529, https://doi.org/10.1175/2009JPO4291.1.

Sasaki, H., Y. Sasai, M. Nonaka, Y. Masumoto, and S. Kawahara, 2006: An Eddy-Resolving Simulation of the Quasi-Global Ocean Driven by Satellite-Observed Wind Field Preliminary Outcomes from Physical and Biological Fields . *J. Earth Simulator*, **6**, 35–49, https://doi.org/10.32131/jes.6.35.

——, M. Nonaka, Y. Masumoto, Y. Sasai, H. Uehara, and H. Sakuma, 2008: An Eddy-Resolving Hindcast Simulation of the Quasiglobal Ocean from 1950 to 2003 on the Earth Simulator. *High Resolution Numerical Modelling of the Atmosphere and Ocean*, Springer New York, 157–185.

Scotti, A., and B. White, 2014: Diagnosing mixing in stratified turbulent flows with a locally defined available potential energy. *J. Fluid Mech.*, **740**, 114–135, https://doi.org/10.1017/jfm.2013.643.

Silvano, A., and Coauthors, 2020: Recent recovery of Antarctic Bottom Water formation in the Ross Sea driven by climate anomalies. *Nat. Geosci.*, **13**, 780–786, https://doi.org/10.1038/s41561-020-00655-3.

Smith, K. S., and G. K. Vallis, 2002: The scales and equilibration of midocean eddies: Forced-dissipative flow. *J. Phys. Oceanogr.*, **32**, 1699–1720, https://doi.org/10.1175/1520-0485(2002)032<1699:TSAEOM>2.0.CO;2.

Sokolov, S., and S. R. Rintoul, 2007: Multiple jets of the antarctic circumpolar current South of Australia. *J. Phys. Oceanogr.*, **37**, 1394–1412, https://doi.org/10.1175/JPO3111.1.

Stewart, A. L., and A. F. Thompson, 2013: Connecting antarctic cross-slope exchange with southern ocean overturning. *J. Phys. Oceanogr.*, **43**, 1453–1471, https://doi.org/10.1175/JPO-D-12-0205.1.

Von Storch, J. S., C. Eden, I. Fast, H. Haak, D. Hernández-Deckers, E. Maier-Reimer, J. Marotzke, and D. Stammer, 2012: An estimate of the Lorenz energy cycle for the World Ocean based on the 1/10°STORM/NCEP simulation. *J. Phys. Oceanogr.*, **42**, 2185–2205, https://doi.org/10.1175/JPO-D-12-079.1.

Talley, L., 2013: Closure of the Global Overturning Circulation Through the Indian, Pacific, and Southern Oceans: Schematics and Transports. *Oceanography*, **26**, 80–97, https://doi.org/10.5670/oceanog.2013.07.

Thompson, A. F., and J. B. Sallée, 2012: Jets and Topography: Jet Transitions and the Impact on Transport in the Antarctic Circumpolar Current. *J. Phys. Oceanogr.*, **42**, 956–972, https://doi.org/10.1175/JPO-D-11-0135.1.

——, and A. C. N. Garabato, 2014: Equilibration of the Antarctic Circumpolar Current by standing meanders. *J. Phys. Oceanogr.*, **44**, 1811–1828, https://doi.org/10.1175/JPO-D-13-0163.1.

Treguier, A. M., J. Le Sommer, J. M. Molines, and B. de Cuevas, 2010: Response of the southern ocean to the southern annular mode: Interannual variability and multidecadal trend. *J. Phys. Oceanogr.*, **40**, 1659–1668, https://doi.org/10.1175/2010JPO4364.1.

Trossman, D. S., B. K. Arbic, J. G. Richman, S. T. Garner, S. R. Jayne, and A. J. Wallcraft, 2016: Impact of topographic internal lee wave drag on an eddying global ocean model. *Ocean Model.*, **97**, 109–128, https://doi.org/10.1016/j.ocemod.2015.10.013.

Tseng, Y. H., and J. H. Ferziger, 2001: Mixing and available potential energy in stratified flows. *Phys. Fluids*, **13**, 1281–1293, https://doi.org/10.1063/1.1358307.

Volkov, D. L., L. L. Fu, and T. Lee, 2010: Mechanisms of the meridional heat transport in the Southern Ocean. *Ocean Dyn.*, **60**, 791–801, https://doi.org/10.1007/s10236-010-0288-0.

Wang, W., and R. X. Huang, 2004: Wind Energy Input to the Ekman Layer*. *J. Phys. Oceanogr.*, **34**, 1267–1275, https://doi.org/10.1175/1520-0485(2004)034<1267:WEITTE>2.0.CO;2.

Watanabe, M., and T. Hibiya, 2002: Global estimates of the wind-induced energy flux to inertial motions in the surface mixed layer. *Geophys. Res. Lett.*, **29**, 2–5, https://doi.org/10.1029/2001GL014422.

Williams, R. G., C. Wilson, and C. W. Hughes, 2007: Ocean and atmosphere storm tracks: The role of eddy vorticity forcing. *J. Phys. Oceanogr.*, **37**, 2267–2289, https://doi.org/10.1175/JPO3120.1.

Witter, D. L., and D. B. Chelton, 1998: Eddy-mean flow interaction in zonal oceanic jet flow along zonal ridge topography. *J. Phys. Oceanogr.*, **28**, 2019–2039, https://doi.org/10.1175/1520-0485(1998)028<2019:EMFIIZ>2.0.CO;2.

Wu, Y., Z. Wang, and C. Liu, 2017: On the response of the Lorenz energy cycle for the Southern Ocean to intensified westerlies. *J. Geophys. Res. Ocean.*, **122**, 2465–2493, https://doi.org/10.1002/2016JC012539.

Youngs, M. K., A. F. Thompson, A. Lazar, and K. J. Richards, 2017: ACC meanders, energy transfer, and mixed barotropic-baroclinic instability. *J. Phys. Oceanogr.*, **47**, 1291–1305, https://doi.org/10.1175/JPO-D-16-0160.1.

——, G. R. Flierl, and R. Ferrari, 2019: Role of residual overturning for the sensitivity of southern ocean isopycnal slopes to changes in wind forcing. *J. Phys. Oceanogr.*, **49**, 2867–2881, https://doi.org/10.1175/JPO-D-19-0072.1.

Zemskova, V. E., B. L. White, and A. Scotti, 2015: Available potential energy and the general circulation: Partitioning wind, buoyancy forcing, and diapycnal mixing. *J. Phys. Oceanogr.*, **45**, 1510–1531, https://doi.org/10.1175/JPO-D-14-0043.1.

Zhai, X., and D. P. Marshall, 2013: Vertical eddy energy fluxes in the North Atlantic subtropical and subpolar gyres. *J. Phys. Oceanogr.*, **43**, 95–103, https://doi.org/10.1175/JPO-D-12-021.1.

——, H. L. Johnson, and D. P. Marshall, 2010: Significant sink of ocean-eddy energy near western boundaries. *Nat. Geosci.*, **3**, 608–612, https://doi.org/10.1038/ngeo943.

Zhang, X., and M. Nikurashin, 2020: Small-Scale Topographic Form Stress and Local Dynamics of the Southern Ocean. *J. Geophys. Res. Ocean.*, **125**, 1–18, https://doi.org/10.1029/2019JC015420.

Zhu, Y., B. Qiu, X. Lin, and F. Wang, 2018: Interannual Eddy Kinetic Energy Modulations in the Agulhas Return Current. *J. Geophys. Res. Ocean.*, **123**, 6449–6462, https://doi.org/10.1029/2018JC014333.